X-ray spectroscopy studies of nonradiative energy transfer processes in luminescent lanthanide materials

Joseph I. Pacold

A dissertation
submitted in partial fulfillment of the
requirements for the degree of

Doctor of Philosophy

University of Washington

2014

Reading Committee:
Gerald T. Seidler, Chair
John J. Rehr
Subhadeep Gupta

Program Authorized to Offer Degree:
Physics

University of Washington

Abstract

X-ray spectroscopy studies of nonradiative energy transfer
processes in luminescent lanthanide materials

Joseph I. Pacold

Chair of the Supervisory Committee:
Professor Gerald T. Seidler
Physics

Luminescent materials play important roles in energy sciences, through solid state lighting and possible applications in solar energy utilization, and in biomedical research and applications, such as in immunoassays and fluorescence microscopy. The initial excitation of a luminescent material leads to a sequence of transitions between excited states, ideally ending with the emission of one or more optical-wavelength photons. It is essential to understand the microscopic physics of this excited state cascade in order to rationally design materials with high quantum efficiencies or with other fine-tuning of materials response. While optical-wavelength spectroscopies have unraveled many details of the energy transfer pathways in luminescent materials, significant questions remain open for many lanthanide-based luminescent materials. For organometallic dyes in particular, quantum yields remain limited in comparison with inorganic phosphors.

This dissertation reports on a research program of synchrotron x-ray studies of the excited state electronic structure and energy-relaxation cascade in trivalent lanthanide phosphors and dyes. To this end, one of the primary results of this dissertation is the first time-resolved x-

ray absorption near edge spectroscopy studies of the transient 4f excited states in lanthanide-activated luminescent dyes and phosphors. This is a new application of time-resolved x-ray absorption spectroscopy that makes it possible to directly observe and, to some extent, quantify intramolecular nonradiative energy transfer processes. We find a transient increase in 4f spectral weight associated with an excited state confined to the 4f shell of trivalent Eu. This result implies that it is necessary to revise the current theoretical understanding of 4f excitation in trivalent lanthanide activators: either transient 4f-5d mixing effects are much stronger than previously considered, or else the lanthanide 4f excited state has an unexpectedly large contribution having a strong charge-transfer character.

A second primary result comes from an an x-ray excited optical luminescence (XEOL) study that demonstrates, for the first time, that the high flux of modern synchrotron light sources can induce high fractional populations of excited states in trivalent lanthanide phosphors. In this work we have identified the leading-order nonlinear-response mechanism by drawing on strong similarities between XEOL and cathodoluminescence. These results establish the groundwork for studies that would allow deeper inquiry into energy-transfer mechanisms through time-resolved x-ray pump/optical-probe spectroscopies, through time-resolved x-ray emission spectroscopy, or through quantifying of higher-order nonlinear effects at further-enhanced fractional excitation levels.

The above scientific results are augmented by a supporting effort in instrumental methodology. This includes the development of high-efficiency x-ray emission spectrometers and their use in collaborations to study pressure-induced changes in f-electron physics and to characterize the intermediate states that occur after photoexcitation of the photosystem-II protein.

Acknowledgements

Throughout my time as a graduate student, I have been extremely fortunate to have Jerry Seidler as a scientific and professional mentor. His advice on the process of doing research has been invaluable, ranging from expert knowledge on synchrotron techniques to the practical details of dealing with writing projects. I am also grateful for the input of my advisory committee – John Rehr, Deep Gupta, David Cobden, and William Stein – on my questions about physics, math, and career planning.

None of this work would have been possible without the work of my many collaborators, particularly David Tatum (Raymond group, UC Berkeley) and Jae Park (Cobden group, University of Washington), who synthesized most of the samples that I studied. Additional samples were generously provided by Bill Reichlin (Diaz group, Central Washington University) and Tetsuhiko Isobe (Keio University). I also benefited greatly from working with Jerry's current and former students, particularly Brian Mattern and Devon Mortensen, who spent many late nights with me at the Advanced Photon Source. The staff at several APS beamlines, particularly Robert Gordon, Xiaoyi Zhang, Steve Heald, Zou Finfrock, and Diego Casa, provided essential guidance and technical expertise. I am also grateful to Josh Kas (Rehr group, UW) for guiding me through FEFF. Finally, I would like to thank my family and my friends here at UW for their care and support.

Table of Contents

Chapter 1. Lanthanide luminescence

1.1 Introduction and summary of the dissertation

Luminescence is the emission of optical-wavelength light by processes other than thermal radiation. This dissertation is primarily concerned with photoluminescence, i.e., emission from processes in which the initial excitation is also caused by visible or near-visible light. Other processes include cathodoluminescence (excited by high-energy electrons), electroluminescence (excited by an applied voltage), and x-ray excited luminescence (discussed in Chapter 5) [1]. Conversion of energy into light has a wide range of natural applications in science and industry, including fluorescent lights, LEDs, and display screens [2-6]; solid-state and dye lasers [7-9]; phosphors for detection of ionizing radiation [10-12]; and biomedical dyes [13-16]. Emerging applications include conversion of the solar spectrum to improve the performance of photovoltaic cells [17-21].

High energy-conversion efficiency is a desirable property in all of these applications; for example, one class of white LEDs became commercially available thanks to years of steady improvement in the efficiency of blue-to-yellow converting phosphors [4, 22, 23]. Therefore, quantum yield is a central figure of merit for photoluminescent materials. In order to rationally design new materials with high quantum yields, it is necessary to understand the atomic, molecular, and solid-state physical processes at work.

This chapter reviews applications of photoluminescent materials and the established UV/visible spectroscopy methods used to characterize them. We identify areas where there are opportunities for x-ray measurements to directly interrogate aspects of luminescence that are not practically accessible in the UV/visible regime. In particular, we will focus on internal energy transfer processes in materials containing lanthanide (Ln) ions, in which the properties of the Ln

4f shell pose unique experimental challenges. Chapter 2 reviews applications of the main experimental method, x-ray absorption near edge spectroscopy (XANES), to transition metal and lanthanide systems.

Chapters 3 and 4 report time-resolved XANES studies of several Ln-activated materials. This is the first set of studies that is directly sensitive to the excited state of the luminescent activator in each sample, and we identify a novel transient XANES signature of 4f intrashell excitation. The effect is general across disparate organometallic and inorganic phosphors, and allows us to monitor a crucial nonradiative transition in the excited state cascade. These results establish time-resolved x-ray methods as a valuable tool for interrogating 4f electronic structure in lanthanide-based luminescent materials. From an applied physics perspective, we have established a new method of characterizing the performance of Ln-based phosphors. From a fundamental condensed matter physics and physical chemistry perspective, the TR-XANES signature raises interesting questions about Ln photophysics. In particular, our results require revision of the standard theoretical models of Ln sensitization and optical emission via $4f \rightarrow 4f$ transitions. Further, they motivate a very specific future direction, wherein we propose that time-resolved x-ray emission spectroscopy can be used to directly investigate the physics of the energy transfer mechanism between sensitizer and emitter in these systems.

Chapter 5 describes an x-ray excited optical luminescence study of several inorganic phosphors. We observe, for the first time, nonlinear saturation effects in the luminescence yield under x-ray excitation at high flux density, and identify the dominant energy-loss mechanism. This allows us to quantify the Ln excited state population induced by the x-ray beam, an important technical consideration for future x-ray spectroscopy studies. Specifically, we have established the necessary context to evaluate the effects of a high-intensity x-ray probe in laser-

pump/x-ray probe studies. The result also demonstrates that *x-ray pump/laser-probe* experiments of Ln phosphors are feasible, opening up the the possibility of studying excitation channels that are not accessible by UV/visible excitation. Given the broad technical importance of Ln-based phosphors, this final capability is a new avenue of research with high potential to identify presently unknown nonradiative quenching mechanisms, and thus have high impact on future efforts to improve, e.g., the quantum efficiency of Ln-based luminescent materials (particularly organometallic complexes and materials).

In Chapter 6 we summarize, conclude, and briefly describe ongoing and proposed work. This emphasizes the new directions, especially at XFEL facilities, that will directly build on the work completed in this dissertation; in particular, we propose to use time-resolved x-ray emission spectroscopy (XES) to study the spin dynamics that accompany Ln 4f excitation. Finally, in an appendix, we describe a class of instruments designed for x-ray emission spectroscopy studies of the lanthanides and transition metals. These instruments have been used in two collaborations: a study of a Ln 4f electronic structure effect, specifically volume collapse and the associated 4f electron delocalization in Pr metal [24], and a time-resolved XES investigation of transient excited states in photosystem II [25]. In addition to their scientific value, these results demonstrate the utility of the instruments for the research program reported here.

1.2 Survey of photoluminescent materials

The process of photoluminescence is shown schematically in Fig. 1.1. The essential component of a phosphor is an "activator," an ion or functional group of atoms with an excited state that preferentially decays by emitting light. In some materials, the activator also absorbs the exciting light (Fig. 1a). However, it is common for the activator to be coupled to a "sensitizer," a

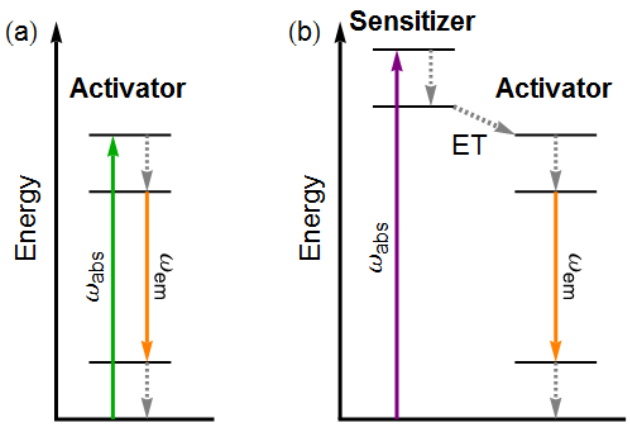

Figure 1.1. Schematic of the process of luminescence. Solid and dashed arrows represent radiative and nonradiative transitions, respectively. (a) A luminescent activator absorbs a photon with frequency ω_{abs} and emits a photon with frequency ω_{em}. Nonradiative relaxation steps may occur before or after emission, producing a Stokes shift $\hbar(\omega_{abs} - \omega_{em})$. (b) The activator may be coupled to a sensitizer that strongly absorbs higher-energy photons. Nonradiative energy transfer (ET) from the sensitizer to the activator fills the desired excited state.

Material	**Example application**	**Sensitizer**	**Activator**	**Stokes shift (eV)**	**Emission transition**	**Luminescence lifetime**	**Emission bandwidth (eV)**
$Al_2O_3:Cr^{3+}$ (ruby) [1, 26]	Solid state laser medium	None	Cr^{3+}	0.7	3d → 3d	3.5 ms	0.06
$Y_3Al_5O_{12}:Ce^{3+}$ (YAG:Ce) [4]	LED material	None	Ce^{3+}	0.7	5d → 4f	65 ns	0.38
$C_{20}H_{12}O_5$ (fluorescein) and derivatives [27, 28]	Biomedical imaging	None	Xanthene moiety	0.1	π* → π	4 ns	0.22
$CaS:Eu^{2+}$ [29]	LED material	None	Eu^{2+}	0.2	5d → 4f	1.4 μs	0.17
$LaPO_4:Ce^{3+},Tb^{3+}$ [2, 3]	Fluorescent lighting	Ce^{3+}	Tb^{3+}	2.2	4f → 4f	3.2 ms	0.05
$YVO_4:Eu^{3+}$ [6]	CRT displays	VO_4^{2-}	Eu^{3+}	1.9	4f → 4f	0.5 ms	0.02
Eu^{3+}-trisbipyridine diamine (TBP:Eu) [30, 31]	Fluorescent immunoassays	TBP ligand	Eu^{3+}	2.1	4f → 4f	0.3 ms	0.02
$LiGdF_4:Eu^{3+}$ [19]	Lighting; quantum cutting	Gd^{3+}	Eu^{3+}	2.5	4f → 4f	0.3 ms	0.02

Table 1.1. Summary of the properties of several luminescent solids and molecules. Possible sensitizers and activators for luminescence include organic functional groups, as well as transition metal and lanthanide ions. Note the large Stokes shifts and long luminescence lifetimes of the phosphors activated by Tb^{3+} and Eu^{3+}.

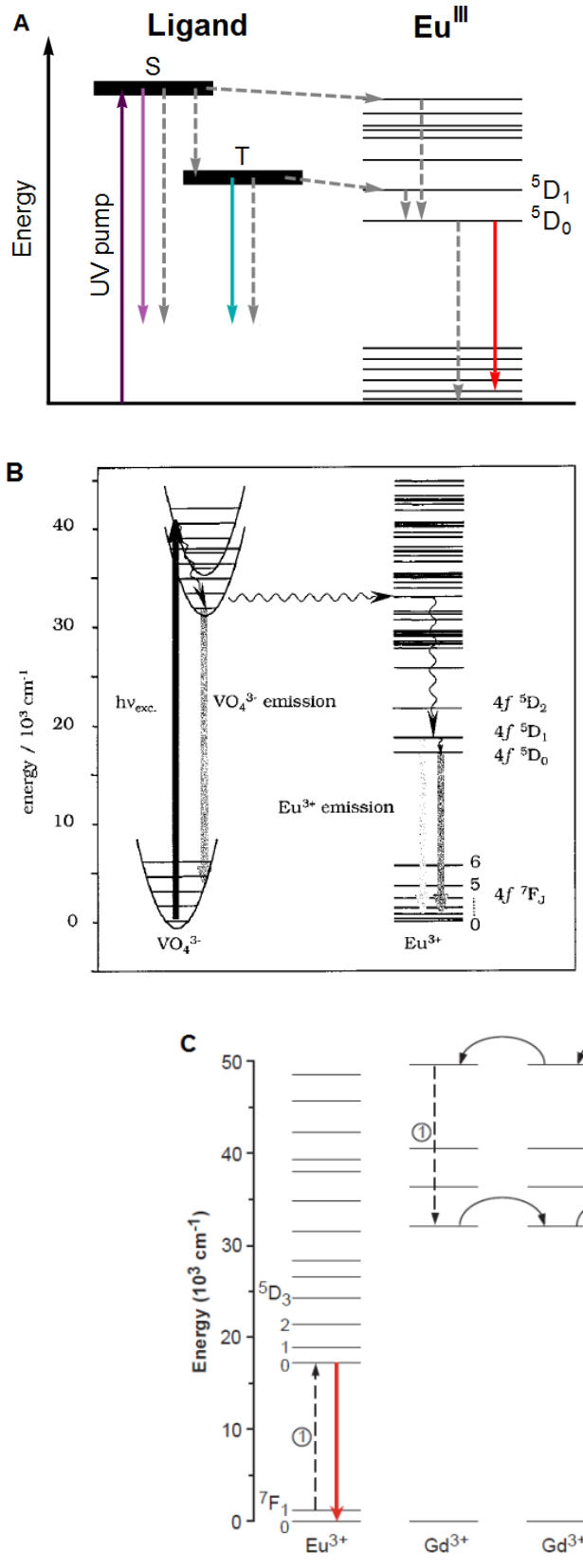

Figure 2.2. Detailed schematics of sensitized luminescence in three Eu-activated systems. (A) A typical Eu-organic dye [32] uses an organic ligand as the sensitizer. Absorption of a UV photon places the ligand in a singlet state (S) that relaxes to a triplet state (T). Nonradiative energy transfer from the T state populates the Eu $^5D_1$ state, which relaxes to the emitting $^5D_0$ state. (B) The inorganic phosphor YVO_4:Eu^{3+} [33] uses the vanadate group as the sensitizer. Energy transfer places the Eu^{3+} ion in a higher-energy state that relaxes to the $^5D_1$ state, followed by relaxation to the $^5D_0$ state. (C) The "quantum cutting" phosphor $LiGdF_4$:Eu^{3+} [19] uses the Gd^{3+} ion in the host lattice as the sensitizer. Two sequential transitions of the Gd^{3+} ion transfer energy to two Eu^{3+} activators, resulting in "quantum cutting," i.e., the emission of two visible photons after the absorption of one UV photon.

strongly absorbing species that can transfer energy nonradiatively to the activator (Fig. 1.1b) [1, 34]. The sensitizer may be an ion, an organic moiety, or a crystal lattice containing the activator as a dopant. Between absorption and emission, the material moves through a series of nonradiative transitions between excited states. Much of the literature on luminescent materials is devoted to identifying the intermediate states and reducing the nonradiative quenching that may occur at each step. To illustrate the variety of materials and processes encountered in the field, Table 1.1 summarizes the photophysical properties of a set of materials with established industrial and scientific applications, and Fig. 1.2 shows the contrasting energy transfer chains in several luminescent systems.

As specific examples, we consider two of the materials in Table 1.1, $CaS:Eu^{2+}$ and $YVO_4:Eu^{3+}$. $CaS:Eu^{2+}$ has a photoluminescence excitation (PLE) band centered near 475 nm and an emission band centered at 650 nm, both from transitions between the 4f and 5d orbitals of the Eu^{2+} ion [29, 35]. Here, Eu^{2+} is the activator and there is no separate sensitizer, i.e, the CaS host lattice does not directly participate in the process of luminescence. The lattice does, however, determine the absorption and emission wavelengths via crystal field splitting of the Eu^{2+} 5d levels. This fact is reflected in the behavior of the emission band as the host lattice changes: the photoluminescence band of $Ca_{1-x}Sr_xS$ shifts continuously as the fraction x increases (Fig. 1.3).

In contrast, the display screen phosphor $YVO_4:Eu^{3+}$ uses the host YVO_4 lattice as a sensitizer for the Eu^{3+} dopant [6]. The PLE spectrum shows a broad UV excitation band centered at 320 nm (Fig. 1.4), derived from V-O charge transfer transitions [33, 36]. The charge transfer state can be converted into an excited state of the Eu^{3+} ion, which proceeds through several lower-energy excited states before emitting a photon. An important qualitative difference from the behavior of divalent Eu is that the emission from trivalent Eu is due to $4f \rightarrow 4f$ intrashell

transitions. This produces a spectrum with sharp emission lines rather than a broad band. The emission wavelengths shift by at most a few nm if the host lattice changes; it is therefore possible to produce Eu^{3+}-activated phosphors with different absorption bands and nearly identical emission spectra [37-39]. For the rest of this chapter, we will focus attention on trivalent lanthanide (Ln^{3+}) phosphors, beginning with a discussion of 4f electronic structure.

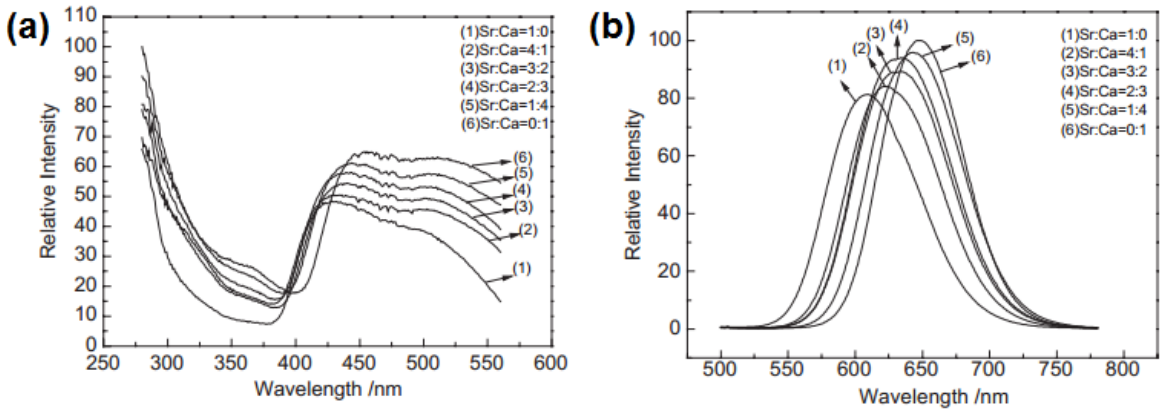

Figure 1.3. From Hu et al. [35], (a) photoluminescence excitation and (b) photoluminescence spectra of $Ca_{1-x}Sr_xS$. Curves are labeled by the Sr:Ca stoichiometric ratio.

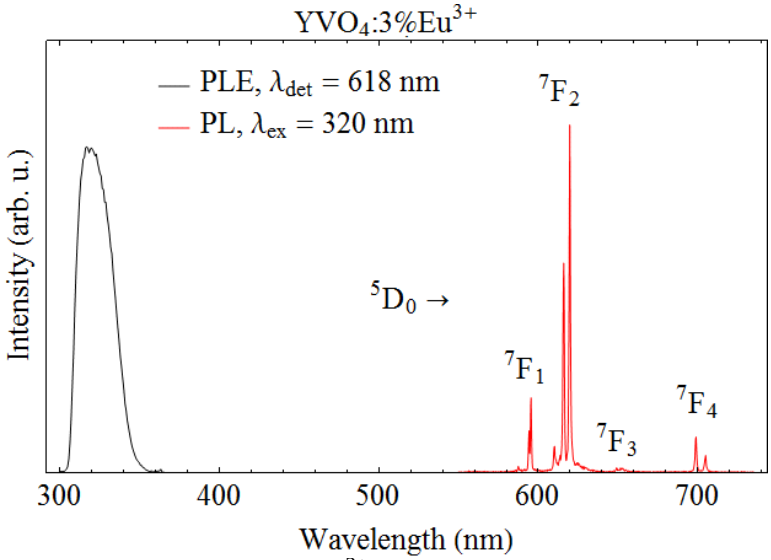

Figure 1.4. PLE and PL spectra of $YVO_4:Eu^{3+}$ powder [40]. The narrow 4f → 4f emission lines are characteristic of Ln^{3+} luminescence (see Table 1.1).

1.3 Lanthanide 4f emission lines

The lanthanide elements are characterized by their partially filled 4f shells. The Ln^{3+} ions in particular have the electron configuration $[Xe]4f^n$, with n increasing from 0 to 14 through the lanthanide series. This produces a rich set of 4f energy levels (Figure 1.5), with transitions between them that emit at wavelengths spanning the visible spectrum. The 4f orbital is spatially surrounded by the 5s and 5p shells, and therefore screened from interaction with other atoms [41, 42]. For instance, the radius of the Eu^{3+} 4f orbital is 0.3 Å while the radius of the filled 5p shell is 0.7 Å [43]. As a result, the 4f levels are very weakly affected by external fields. When an Ln^{3+} ion is embedded in a solid (or bound to a ligand), the 4f emission lines show little crystal field

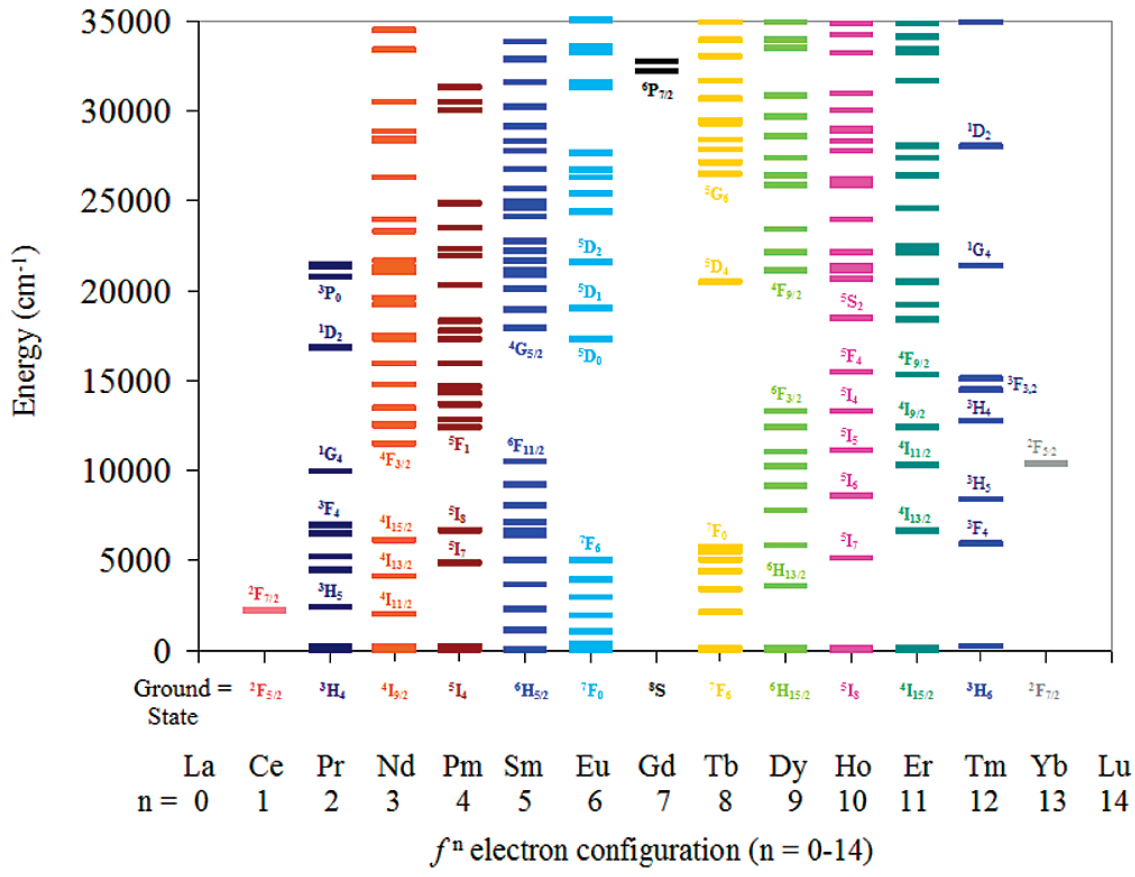

Figure 1.5. From Moore et al. [32], 4f energy levels of the trivalent lanthanide ions.

splitting and almost no broadening from, e.g., coupling to phonons. This means that the 4f excited states of an Ln^{3+} activator in a luminescent material correspond well with excited states of the bare ion, and it is standard practice to label them with atomic term symbols in the LS-coupling scheme [17, 41], as in Figs. 1.4 and 1.5.

The *intensities* of certain 4f → 4f lines, however, vary greatly as the local environment changes. These are referred to as the "hypersensitive" lines [41, 44]. For example, Eu^{3+} ions bound to different organic ligands show an order of magnitude of variation in the intensity of the $^5D_0 \rightarrow {}^7F_2$ emission [45]. This effect is essential for practical applications of Ln^{3+} luminescence, since 4f → 4f transitions on the bare ion are parity-forbidden and extremely weak. Judd and Ofelt [46, 47] proposed that hypersensitivity is due to mixing of the Ln^{3+} 4f orbitals with opposite-parity 5d states, induced by the ligand or crystal field. This occurs, for example, when the Ln^{3+} dopant site in a crystal lattice does not have inversion symmetry. The parity selection rule is relaxed for mixed 4f-5d states, allowing radiative transitions between them.

Other contributions to the hypersensitive effect have been proposed, though theoretical calculations indicate that they enter at lower order than mixing of opposite-parity Ln^{3+} states. Jorgensen and Judd [48] noted that all the hypersensitive lines come from electric quadrupole transitions. This led them to propose a mechanism based on inhomogeneities in the dielectric constant around the Ln^{3+} ion, again caused by the ligand or crystal field. Judd later showed that this approach is equivalent to considering polarization of the ligand induced by the Ln^{3+} 4f electrons [49, 50]. Mixing with charge transfer states has also been investigated [51, 52].

1.4 Quenching mechanisms

Recall again that the 4f → 4f transitions are parity-forbidden (in some cases they are also forbidden by spin). Consequently, 4f intrashell excited states are long-lived, and Ln^{3+} phosphors

have luminescence lifetimes of up to milliseconds, orders of magnitude longer than most other luminescent materials. (See Table 1.1; note that Ce^{3+} is an exception since it emits via 5d → 4f transitions.) This property is crucial in two biomedical applications. First, we consider fluorescence microscopy, in which a fluorescent species is bound to a biologically active structure or molecule and used to track its position within an organism. A wide variety of fluorescent labels has been developed to fit the varying technical constraints of imaging studies [28, 53, 54]. Ln^{3+}-activated dyes in particular are useful in imaging highly autofluorescent species, i.e., organisms that natively produce fluorescent molecules and tissues. The long lifetime of the 4f → 4f emission makes it possible to remove autofluorescence backgrounds by time-gating [13, 55, 56]; see Fig. 1.6. Second, Ln^{3+} dyes are used in assays that study the interaction of two macromolecules, e.g., an antibody and an antigen [14, 57-59]. In an experiment of this type (Fig. 1.7), the long lifetime of the 4f excited state increases the probability of energy transfer from the Ln^{3+} to a second luminescent label. The transfer rate is distance-dependent (see Section 1.5) and can therefore be used to measure the ensemble-averaged distance between the two labeled macromolecules.

However, the long lifetime also introduces a problem: faster processes may quench the luminescence by causing the excited state to relax nonradiatively, rather than by emitting a photon. Avoiding these quenching effects is part of the process of rational design of phosphors. We consider two examples. First, in solution-phase systems, solvent quenching is a common obstacle. The O-H bonds of water have vibrational modes that are energetically well matched with Ln^{3+} excited states [60-62]. Ligands for soluble luminescent dyes are therefore usually chelates designed to prevent coordination of water molecules with the Ln^{3+}. Water coordination can be detected by comparing dye solutions in H_2O and D_2O (deuterated water). Since the

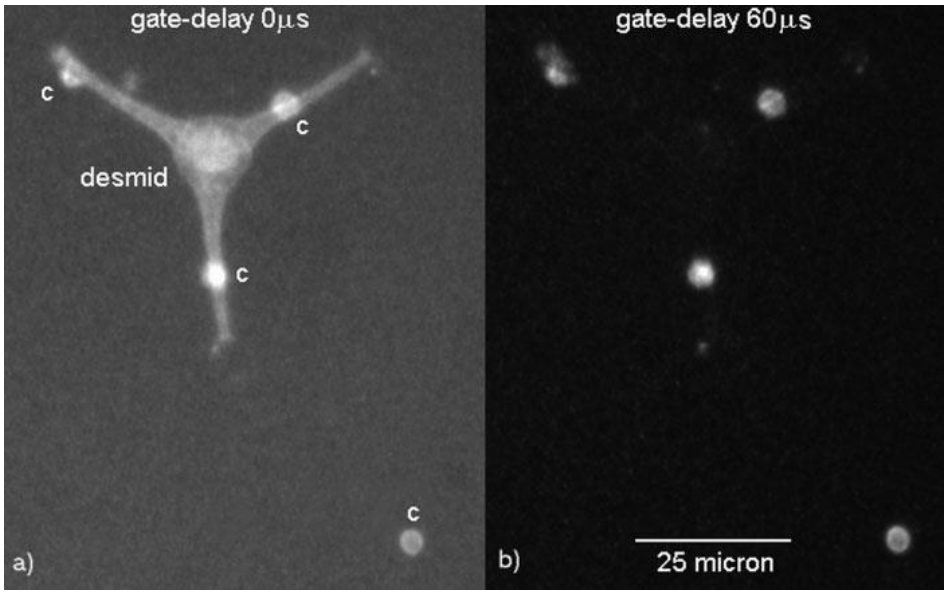

Figure 1.6. From Connally et al. [55]. (a) An algal desmid with several cysts (c) that have been labeled with an Eu-activated dye. Under UV illumination, both the dye and the desmid itself are fluorescent. (b) Time-gated acquisition of the image suppresses the μs-lifetime background from the desmid.

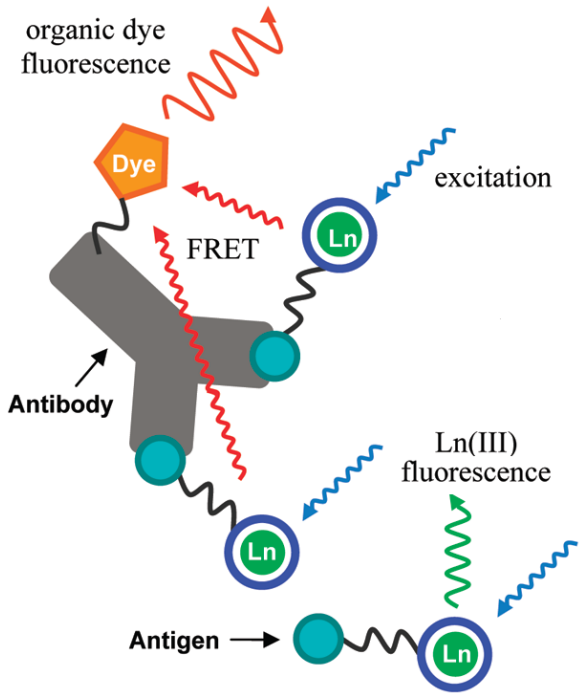

Fig. 1.7. Schematic of an immunoassay using two fluorescent labels, adapted from Moore et al. [32]. The interaction between an antigen and an antibody is studied by labeling the antigen with a Ln-activated dye (~100-μs luminescence lifetime) and the antibody with a purely organic dye (~1-μs luminescence lifetime). The sample is excited with a pulse of light at a wavelength that preferentially excites the Ln dye. If the antibody binds to the antigen, the dye molecules are held sufficiently close together for Forster resonant energy transfer (FRET) from the Ln ion to the organic dye to occur (see Section 1.6). This suppresses the luminescence from the Ln and induces luminescence from the organic dye on long timescales (i.e. > 1 μs).

vibrational modes of the O-D and O-H bonds have different energies, H_2O is a stronger quencher, and the H_2O/D_2O coordination number can be calculated from the luminescence lifetimes of the two solutions [63].

Second, we consider quenching due to interactions among multiple Ln^{3+} ions. Such effects become significant in solid state systems with a high concentration of activators. It is possible for an excitation created on one activator ion to be transferred nonradiatively to other nearby activators; if this process is repeated until the excitation reaches, e.g., a defect in the host lattice, the energy is lost [64]. Another possibility is that "cross-relaxation," closely analogous to the Auger effect, may reduce the luminescence yield [65, 66]. Cross-relaxation can occur when two activators are both in excited states. Instead of emitting a photon, one activator can transfer energy to the second, driving it into a higher (possibly non-emissive) excited state. We will discuss this process further in Chapter 5, in the context of saturation of the luminescence yield at high excitation density.

1.5 Sensitizer-to-activator energy transfer: rate and efficiency measurements

Studies of the nonradiative energy transfer (ET) from the sensitizer to the activator (Fig. 1.1b) lead to several interesting technical challenges. The main quantities of interest are the efficiency of ET from a given sensitizer excited state and the rate of ET to a given excited state of the activator. Here, we summarize several UV/visible spectroscopy ET studies to outline current methods. ET rates can be studied by measuring the rise and decay times of emission from the excited states of the sensitizer and activator. Typically, the result is a correspondence between the decay of emission from particular sensitizer states with the onset of emission from activator states [33, 67]; this yields a map of the excited state cascade.

ET efficiency studies, on the other hand, face an experimental challenge: it is difficult to directly measure the occupation numbers of the relevant Ln^{3+} excited states. It is therefore necessary to deduce the ET efficiency from some other observable. The experiments outlined here take two approaches. First, one can add and remove "external" ET pathways in a quantitatively controlled way by letting a phosphor interact with another fluorescent species. Second, in the specific case of Eu^{3+}, it is possible to calculate the ET efficiency from branching ratios in the emission spectrum and the measured luminescence lifetime.

To understand the first strategy, we consider the overall quantum efficiency Φ of any phosphor, which is the product of the efficiency of each step in the chain of excited states. For a sensitized phosphor, we can write

$$\Phi = \Phi_{\text{sens}}\Phi_{\text{em}}, \tag{1.1}$$

where Φ_{sens} is the probability that an absorbed photon is successfully converted into an excited state of the activator, and Φ_{em} is the probability that the activator emits a photon (rather than being quenched). Measuring Φ is straightforward, so if Φ_{em} can be determined, it is possible to calculate Φ_{sens}.

Xiao and Selvin [68] demonstrated a method for determining Φ_{em} in luminescent Ln-organic complexes by taking advantage of ET from the *activator* to a second, well-understood luminescent molecule. Solutions were prepared with varying concentrations of a Tb^{3+} complex and the standard dye fluorescein, and excited at a wavelength absorbed only by the Tb^{3+} complex. Increasing the fluorescein concentration led to fluorescein emission as a result of ET from the Tb^{3+} ion, and simultaneous suppression of the Tb^{3+} luminescence. The quantum yield of the overall process and the known quantum yield of fluorescein were then used to calculate Φ_{em} (and hence Φ_{sens}).

Beeby [69] and Werts [45] developed another method that applies only to Eu^{3+}. Φ_{em} can be written in terms of the radiative and nonradiative decay rates of the activator excited state, k_{rad} and k_{nr}:

$$\Phi_{em} = \frac{k_{rad}}{k_{rad} + k_{nr}}. \tag{1.2}$$

Both k_{rad} and k_{nr} contribute to the observed luminescence lifetime of the phosphor, τ_{obs}:

$$\tau_{obs} = \frac{1}{k_{rad} + k_{nr}}. \tag{1.3}$$

In the case of Eu^{3+}, it is possible to extract the purely radiative decay rate k_{rad} from a branching ratio in the steady-state emission spectrum. We write k_{rad} as a sum of the spontaneous transition rates for emission from the $^5D_0$ state (see Fig. 1.4):

$$k_{rad} = \sum_{J=1}^{4} P(^5D_0 \rightarrow {}^7F_J) \tag{1.4}$$

The transition $^5D_0 \rightarrow {}^7F_1$ is a purely magnetic dipole transition and consequently independent of the ligand or crystal field affecting the Eu^{3+} ion. The known transition rate $P(^5D_0 \rightarrow {}^7F_J)$ [69] can be used to calculate by rewriting Eq. (1.4) as

$$k_{rad} = P(^5D_0 \rightarrow {}^7F_1)\frac{\sum_{J=1}^{4} P(^5D_0 \rightarrow {}^7F_J)}{P(^5D_0 \rightarrow {}^7F_1)} = P(^5D_0 \rightarrow {}^7F_1)\frac{I_{tot}}{I_1} \tag{1.5}$$

where I_{tot} is the integrated intensity of the entire $^5D_0$-derived portion of the emission spectrum, while and I_1 is the integrated intensity of the $^5D_0 \rightarrow {}^7F_1$ line. This determines k_{rad}, which gives k_{nr} by Eq. (1.3), and hence Φ_{em} and Φ_{sens} by Eqs. (1.2) and (1.1).

We note that both of these methods use measurements of optical emission from the Ln ion. In studies of the excited state kinetics of the sensitizing ligand, it is possible to collect two sets of complementary data: one can observe the rise and decay times of emission from the relevant excited states [67] and use transient UV absorption to measure the excited state occupancies after photoexcitation [70]. For the Ln ion, however, transient absorption studies are

impractical, as the 4f → 4f transitions of interest are parity-forbidden. This presents an opportunity for activator-specific x-ray spectroscopy studies, since the photoelectric cross-sections of the Ln elements are larger in the hard x-ray regime than in the visible. Chapters 3 and 4 report x-ray studies of luminescent dyes that directly target the activator ion to yield information about the population of the $^5D_0$ state, providing an valuable complement to UV/visible data. Chapter 5 reports another approach to using x-rays as the probe by collecting x-ray excited optical luminescence.

1.6 Sensitizer-to-activator energy transfer: mechanisms

In this section, we describe the two dominant ET mechanisms observed in most lanthanide systems. To qualitatively understand the process of internal energy transfer, consider the Hamiltonian for a sensitizer (S) coupled to a lanthanide ion (Ln) by an interaction *U*,

$$H_S + H_{Ln} + U(r_S, r_{Ln}, \chi_S, \chi_{Ln}). \tag{1.6}$$

In general, *U* will be a function of the positions and the spin states of the sensitizer and lanthanide. We denote the ground state of each species by ψ_S and ψ_{Ln}, and excited states by ψ'_S and ψ'_{Ln}. The interaction allows transitions in which an excited state of the sensitizer is transferred nonradiatively to the lanthanide, with transition rate

$$k_{ET} \propto |\langle \psi'_S \psi_{Ln} | U(r_S, r_{Ln}, \chi_S, \chi_{Ln}) | \psi_S \psi'_{Ln} \rangle|^2 \delta(\Delta E_S - \Delta E_{Ln}). \tag{1.7}$$

Performing a multipole expansion of *U* yields a number of possible energy transfer processes. For lanthanide-organic complexes similar to the samples discussed here, DFT-based calculations [71-74] indicate that the dominant processes are Förster resonant energy transfer [75] and Dexter transfer [76]. At lowest order, Förster transfer occurs when the transitions $\psi'_S \rightarrow \psi_S$ and $\psi_{Ln} \rightarrow \psi'_{Ln}$ are both electric dipole-allowed (the term "Förster transfer" also includes higher-order multipole transitions). This can be thought of as a transition driven by the

Coulomb interaction between the sensitizer and Ln. The transition rate shows a power-law dependence on the distance between the sensitizer and activator.

Dexter transfer, on the other hand, is driven by charge exchange. If we expand Eq. (1.7) to higher order and keep track of the spin part of each wavefunction, we obtain exchange integral terms, beginning with

$$\int \phi_S'^*(r_S)\phi_{Ln}^*(r_{Ln})\frac{1}{r_S - r_{Ln}}\phi_S(r_{Ln})\phi_{Ln}'(r_S) \times \chi_S'^*(\sigma_S)\chi_{Ln}^*(\sigma_{Ln})\chi_S(\sigma_{Ln})\chi_{Ln}'(\sigma_S) \qquad (1.8)$$

This term will be nonzero only when the spin states of both S and Ln change (see Fig. 1.8). The electric *n*-pole operators do not act on spins, so it follows that in this case there is no Förster transfer. Furthermore, this term will be negligible unless there is substantial spatial overlap between the sensitizer and Ln wavefunctions. The Dexter transition rate thus decreases exponentially with distance.

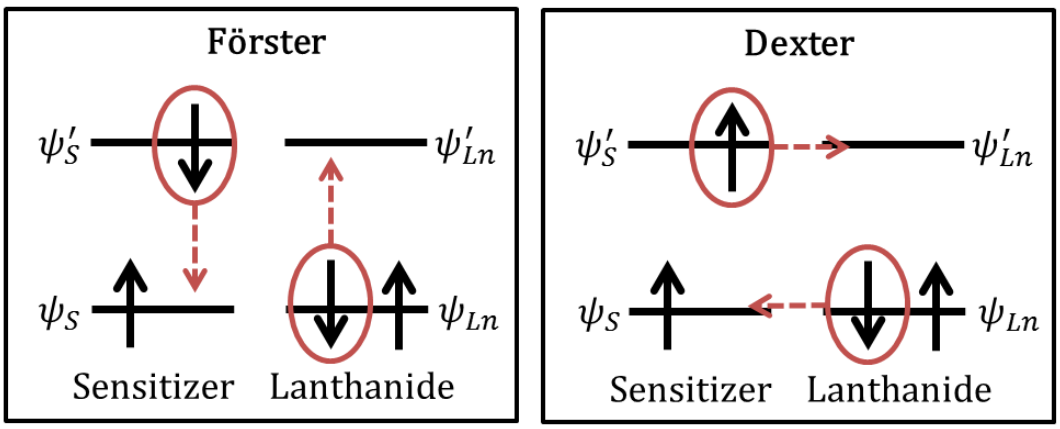

Figure 1.8. Schematics of Förster energy transfer (caused by Coulomb terms in the interaction between the sensitizer and the lanthanide) and Dexter transfer (mediated by charge exchange terms).

The difference in behavior with distance can be used to identify the transition mechanism in some cases. Stryer and Haugland [77] observed Förster transfer by synthesizing a set of organic molecules in which the sensitizer and activator were separated by carbon chains of

several lengths. In most luminescent systems, however (including inorganic phosphors and Ln^{3+} chelates), this type of direct control is impossible. There are also interesting exceptions to the general distance-dependence behavior of both processes. For example, Dexter transfer has been counterintuitively found to be the dominant process over distances of up to 20 Å in one class of large metal-organic complexes [78]. A long-term goal of the research program initiated by this dissertation is to use the spin-sensitivity of x-ray emission spectroscopy to experimentally distinguish between the two mechanisms across a broad class of photoactive materials.

1.6 Conclusion

While the properties of many luminescent systems are superficially similar, the intermediate steps between absorption and emission of photons vary widely. Decades of UV/visible spectroscopy studies have been dedicated to mapping the excited state pathways, and corresponding synthesis work has led to increasingly sophisticated and efficient phosphors. In lanthanide-activated phosphors in particular, optical emission measurements can provide detailed information on the excited state kinetics of both the sensitizer and the activator. The sensitizer-to-activator energy transfer efficiency can be deduced from observations of the emission in some cases, and transient absorption can be used to further interrogate the sensitizer. This leaves an opportunity for transient absorption measurements to provide unique insights into the 4f electron physics of the lanthanide ion. However, such experiments are impractical in the UV/visible regime. The rest of this dissertation covers novel applications of x-ray spectroscopy to this question.

1.7 References

1. Blasse, G. and B.C. Grabmeier, *Luminescent Materials.* 1994, Berlin: Springer-Verlag.
2. Riwotzki, K., et al., *Liquid-phase synthesis of colloids and redispersible powders of strongly luminescing $LaPO_4$:Ce,Tb nanocrystals.* Angewandte Chemie-International Edition, 2001. **40**(3): p. 573-576.

3. Bourcet, J.C. and F.K. Fong, *Quantum Efficiency of Diffusion Limited Energy-Transfer in $La_{1-x-y}Ce_xTbYPO_4$.* Journal of Chemical Physics, 1974. **60**(1): p. 34-39.
4. Bachmann, V., C. Ronda, and A. Meijerink, *Temperature Quenching of Yellow Ce^{3+} Luminescence in YAG:Ce.* Chemistry of Materials, 2009. **21**(10): p. 2077-2084.
5. Hunt, R.B. and R.G. Pappalardo, *Fast Excited-State Relaxation of Eu-Eu Pairs in Commercial Y_2O_3-Eu^{3+} Phosphors.* Journal of Luminescence, 1985. **34**(3): p. 133-146.
6. Levine, A.K. and F.C. Palilla, *A New, Highly Efficient Red-Emitting Cathodoluminescent Phosphor (YVO_4:Eu) for Color Television.* Applied Physics Letters, 1964. **5**(6): p. 118.
7. Reisfeld, R. and C.K.l. Jørgensen, *Lasers and excited states of rare earths.* 1977, Berlin; New York: Springer-Verlag.
8. Kuriki, K., Y. Koike, and Y. Okamoto, *Plastic optical fiber lasers and amplifiers containing lanthanide complexes.* Chemical Reviews, 2002. **102**(6): p. 2347-2356.
9. Weber, J.K.R., et al., *Glass fibres of pure and erkium- or neodymium-doped yttria-alumina compositions.* Nature, 1998. **393**(6687): p. 769-771.
10. Eliseeva, S.V. and J.C.G. Bunzli, *Rare earths: jewels for functional materials of the future.* New Journal of Chemistry, 2011. **35**(6): p. 1165-1176.
11. Neeraj, S., N. Kijima, and A.K. Cheetham, *Novel red phosphors for solid state lighting; the system $Bi_xLn_{1-x}VO_4$:Eu^{3+}/Sm^{3+} (Ln = Y, Gd).* Solid State Communications, 2004. **131**(1): p. 65-69.
12. Lozykowski, H.J., W.M. Jadwisienczak, and I. Brown, *Photoluminescence and cathodoluminescence of GaN doped with Tb.* Applied Physics Letters, 2000. **76**(7): p. 861-863.
13. Soini, E. and T. Lovgren, *Time-Resolved Fluorescence of Lanthanide Probes and Applications in Biotechnology.* Crc Critical Reviews in Analytical Chemistry, 1987. **18**(2): p. 105-154.
14. Handl, H.L. and R.J. Gillies, *Lanthanide-based luminescent assays for ligand-receptor interactions.* Life Sciences, 2005. **77**(4): p. 361-371.
15. Petoud, S., et al., *Stable lanthanide luminescence agents highly emissive in aqueous solution: Multidentate 2-hydroxyisophthalamide complexes of Sm^{3+}, Eu^{3+}, Tb^{3+}, Dy^{3+}.* Journal of the American Chemical Society, 2003. **125**(44): p. 13324-13325.
16. Parker, D. and J.A.G. Williams, *Getting excited about lanthanide complexation chemistry.* Journal of the Chemical Society-Dalton Transactions, 1996(18): p. 3613-3628.
17. Bunzli, J.C.G. and S.V. Eliseeva, *Lanthanide NIR luminescence for telecommunications, bioanalyses and solar energy conversion.* Journal of Rare Earths, 2010. **28**(6): p. 824-842.
18. Trupke, T., et al., *Efficiency enhancement of solar cells by luminescent up-conversion of sunlight.* Solar Energy Materials and Solar Cells, 2006. **90**(18-19): p. 3327-3338.
19. Wegh, R.T., et al., *Visible quantum cutting in $LiGdF_4$:Eu^{3+} through downconversion.* Science, 1999. **283**(5402): p. 663-666.
20. Richards, B.S., *Enhancing the performance of silicon solar cells via the application of passive luminescence conversion layers.* Solar Energy Materials and Solar Cells, 2006. **90**(15): p. 2329-2337.
21. Richards, B.S., *Luminescent layers for enhanced silicon solar cell performance: Down-conversion.* Solar Energy Materials and Solar Cells, 2006. **90**(9): p. 1189-1207.

22. Schlotter, P., R. Schmidt, and J. Schneider, *Luminescence conversion of blue light emitting diodes.* Applied Physics a-Materials Science & Processing, 1997. **64**(4): p. 417-418.
23. Schlotter, P., et al., *Fabrication and characterization of GaN/InGaN/AlGaN double heterostructure LEDs and their application in luminescence conversion LEDs.* Materials Science and Engineering B-Solid State Materials for Advanced Technology, 1999. **59**(1-3): p. 390-394.
24. Bradley, J.A., et al., *4f electron delocalization and volume collapse in praseodymium metal.* Physical Review Letters, 2011(submitted).
25. Davis, K.M., et al., *Room Temperature Mn Kβ X-ray emission analysis of Photosystem II.* 2011(in preparation).
26. Forman, R.A., et al., *Pressure Measurement Made by Utilization of Ruby Sharp-Line Luminescence.* Science, 1972. **176**(4032): p. 284-&.
27. Tanaka, K., et al., *Rational design of fluorescein-based fluorescence probes, mechanism-based design of a maximum fluorescence probe for singlet oxygen.* Journal of the American Chemical Society, 2001. **123**(11): p. 2530-2536.
28. Sun, W.C., et al., *Synthesis of fluorinated fluoresceins.* Journal of Organic Chemistry, 1997. **62**(19): p. 6469-6475.
29. Swiatek, K., et al., *Optical Recombination Mechanisms in Eu^{2+}-Doped CaS and SrS Thin-Films.* Journal of Applied Physics, 1993. **74**(5): p. 3442-3446.
30. Guillaumont, D., et al., *Luminescent Eu(III) and Gd(III) trisbipyridine cryptates: Experimental and theoretical study of the substituent effects.* Chemphyschem, 2007. **8**(3): p. 480-488.
31. Mathis, G., *Probing Molecular-Interactions with Homogeneous Techniques Based on Rare-Earth Cryptates and Fluorescence Energy-Transfer.* Clinical Chemistry, 1995. **41**(9): p. 1391-1397.
32. Moore, E.G., A.P.S. Samuel, and K.N. Raymond, *From Antenna to Assay: Lessons Learned in Lanthanide Luminescence.* Accounts of Chemical Research, 2009. **42**(4): p. 542-552.
33. Riwotzki, K. and M. Haase, *Colloidal YVO_4:Eu and $YP_{0.95}V_{0.05}O_4$:Eu nanoparticles: Luminescence and energy transfer processes.* Journal of Physical Chemistry B, 2001. **105**(51): p. 12709-12713.
34. Weissman, S.I., *Intramolecular energy transfer - The fluorescence of complexes of europium.* Journal of Chemical Physics, 1942. **10**(4): p. 214-217.
35. Hu, Y.S., et al., *Preparation and luminescent properties of $(Ca_{1-x}Sr_x)S:Eu^{2+}$ red-emitting phosphor for white LED.* Journal of Luminescence, 2005. **111**(3): p. 139-145.
36. Riwotzki, K. and M. Haase, *Wet-chemical synthesis of doped colloidal nanoparticles: YVO_4:Ln (Ln = Eu, Sm, Dy).* Journal of Physical Chemistry B, 1998. **102**(50): p. 10129-10135.
37. Huang, X.Y., et al., *Spectral conversion for solar cell efficiency enhancement using $YVO_4:Bi^{3+},Ln^{3+}$ (Ln = Dy, Er, Ho, Eu, Sm, and Yb) phosphors.* Journal of Applied Physics, 2011. **109**(11).
38. Takeshita, S., T. Isobe, and S. Niikura, *Low-temperature wet chemical synthesis and photoluminescence properties of $YVO_4:Bi^{3+},Eu^{3+}$ nanophosphors.* Journal of Luminescence, 2008. **128**(9): p. 1515-1522.

39. Takeshita, S., et al., *Effects of the homogeneous Bi^{3+} doping process on photoluminescence properties of $YVO_4:Bi^{3+},Eu^{3+}$ nanophosphor.* Journal of Luminescence, 2009. **129**(9): p. 1067-1072.
40. Pacold, J.I., et al., 2014 (manuscript in preparation).
41. Bunzli, J.C.G. and C. Piguet, *Taking advantage of luminescent lanthanide ions.* Chemical Society Reviews, 2005. **34**(12): p. 1048-1077.
42. Eliseeva, S.V.B., J. C. G., *Lanthanide luminescence for functional materials and bio-sciences.* Chemical Society Reviews, 2009. **39**: p. 189-227.
43. Waber, J.T. and D.T. Cromer, *Orbital Radii of Atoms and Ions.* Journal of Chemical Physics, 1965. **42**(12): p. 4116-&.
44. Bunzli, J.C.G.E., S. V., *Basics of Lanthanide Photophysics*, in *Lanthanide Luminescence*, H.P.H. H., Editor 2011, Springer Berlin Heidelberg. p. 1-45.
45. Werts, M.H.V., R.T.F. Jukes, and J.W. Verhoeven, *The emission spectrum and the radiative lifetime of Eu^{3+} in luminescent lanthanide complexes.* Physical Chemistry Chemical Physics, 2002. **4**(9): p. 1542-1548.
46. Judd, B.R., *Optical Absorption Intensities of Rare-Earth Ions.* Physical Review, 1962. **127**(3): p. 750.
47. Ofelt, G.S., *Intensities of Crystal Spectra of Rare-Earth Ions.* Journal of Chemical Physics, 1962. **37**(3): p. 511.
48. Jorgensen, C.K. and B.R. Judd, *Hypersensitive Pseudoquadrupole Transitions in Lanthanides.* Molecular Physics, 1964. **8**(3): p. 281.
49. Judd, B.R., *Ionic Transitions Hypersensitive to Environment.* Journal of Chemical Physics, 1979. **70**(11): p. 4830-4833.
50. Mason, S.F., R.D. Peacock, and B. Stewart, *Ligand-Polarization Contributions to Intensity of Hypersensitive Trivalent Lanthanide Transitions.* Molecular Physics, 1975. **30**(6): p. 1829-1841.
51. Peacock, R.D., *Charge-Transfer Contribution to Intensity of Hypersensitive Trivalent Lanthanide Transitions.* Molecular Physics, 1977. **33**(5): p. 1239-1246.
52. Blasse, G., *The influence of charge-transfer and rydberg states on the luminescence properties of lanthanides and actinides.* Structure and Bonding, 1976. **26**: p. 43-79.
53. Urano, Y., et al., *Rational design of fluorescein-based fluorescence probes. Mechanism-based design of a maximum fluorescence probe for singlet oxygen.* Free Radical Biology and Medicine, 2001. **31**: p. S125-S125.
54. Hebbink, G.A., et al., *Unexpected sensitization efficiency of the near-infrared Nd^{3+}, Er^{3+}, and Yb^{3+} emission by fluorescein compared to eosin and erythrosin.* Journal of Physical Chemistry A, 2003. **107**(14): p. 2483-2491.
55. Connally, R., D. Veal, and J. Piper, *Time-resolved fluorescence microscopy using an improved europium chelate BHHST for the in situ detection of Cryptosporidium and Giardia.* Microscopy Research and Technique, 2004. **64**(4): p. 312-322.
56. Yuan, J.L. and G.L. Wang, *Lanthanide-based luminescence probes and time-resolved luminescence bioassays.* Trac-Trends in Analytical Chemistry, 2006. **25**(5): p. 490-500.
57. Soini, E. and I. Hemmila, *Fluoroimmunoassay - Present Status and Key Problems.* Clinical Chemistry, 1979. **25**(3): p. 353-361.
58. Werts, M.H.V., et al., *A near-infrared luminescent label based on Yb-III ions and its application in a fluoroimmunoassay.* Angewandte Chemie-International Edition, 2000. **39**(24): p. 4542.

59. Selvin, P.R., *Principles and biophysical applications of lanthanide-based probes.* Annual Review of Biophysics and Biomolecular Structure, 2002. **31**: p. 275-302.
60. Heller, A., *Formation of Hot Oh Bonds in Radiationless Relaxations of Excited Rare Earth Ions in Aqueous Solutions.* Journal of the American Chemical Society, 1966. **88**(9): p. 2058-&.
61. Haas, Y. and G. Stein, *Pathways of Radiative and Radiationless Transitions in Europium(Iii) Solutions - Role of High Energy Vibrations.* Journal of Physical Chemistry, 1971. **75**(24): p. 3677.
62. Kropp, J.L. and M.W. Windsor, *Luminescence and Energy Transfer in Solutions of Rare-Earth Complexes. I. Enhancement of Fluorescence by Deuterium Substitution.* Journal of Chemical Physics, 1965. **42**(5): p. 1599.
63. Supkowski, R.M. and W.D. Horrocks, *On the determination of the number of water molecules, q, coordinated to europium(III) ions in solution from luminescence decay lifetimes.* Inorganica Chimica Acta, 2002. **340**: p. 44-48.
64. Dexter, D.L. and J.H. Schulman, *Theory of Concentration Quenching in Inorganic Phosphors.* Journal of Chemical Physics, 1954. **22**(6): p. 1063-1070.
65. Robbins, D.J., *On Predicting the Maximum Efficiency of Phosphor Systems Excited by Ionizing-Radiation.* Journal of the Electrochemical Society, 1980. **127**(12): p. 2694-2702.
66. Deleeuw, D.M. and G.W. Thooft, *Method for the Analysis of Saturation Effects of Cathodoluminescence in Phosphors - Applied to Zn_2SiO_4-Mn and $Y_3Al_5O_{12}$-Tb.* Journal of Luminescence, 1983. **28**(3): p. 275-300.
67. Yang, C., et al., *A highly luminescent europium complex showing visible-light-sensitized red emission: Direct observation of the singlet pathway.* Angewandte Chemie-International Edition, 2004. **43**(38): p. 5010-5013.
68. Xiao, M. and P.R. Selvin, *Quantum yields of luminescent lanthanide chelates and far-red dyes measured by resonance energy transfer.* Journal of the American Chemical Society, 2001. **123**(29): p. 7067-7073.
69. Beeby, A., et al., *Intramolecular sensitisation of lanthanide(III) luminescence by acetophenone-containing ligands: the critical effect of para-substituents and solvent.* Journal of the Chemical Society-Dalton Transactions, 2002(1): p. 48-54.
70. Moore, E.G., et al., *A comparison of sensitized Ln(III) emission using pyridine- and pyrazine-2,6-dicarboxylates - part II.* Dalton Transactions, 2013. **42**(6): p. 2075-2083.
71. Malta, O.L., *Ligand-rare-earth ion energy transfer in coordination compounds. A theoretical approach.* Journal of Luminescence, 1997. **71**(3): p. 229-236.
72. Malta, O.L., et al., *Experimental and theoretical study of ligand field, 4f-4f intensities and emission quantum yield in the compound $Eu(bpyO_2)_4(ClO_4)_3$.* Journal of Alloys and Compounds, 2001. **323**: p. 654-660.
73. Lima, P.P., et al., *Energy transfer mechanisms in organic-inorganic hybrids incorporating europium(III): A quantitative assessment by light emission spectroscopy.* Journal of Physical Chemistry C, 2007. **111**(47): p. 17627-17634.
74. Malta, O.L., *Mechanisms of non-radiative energy transfer involving lanthanide ions revisited.* Journal of Non-Crystalline Solids, 2008. **354**(42-44): p. 4770-4776.
75. Forster, T., *Excitation Transfer and Internal-Conversion.* Chemical Physics Letters, 1971. **12**(2): p. 422-424.
76. Dexter, D.L., *A Theory of Sensitized Luminescence in Solids.* Journal of Chemical Physics, 1953. **21**(5): p. 836-850.

77. Stryer, L. and R.P. Haugland, *Energy Transfer - a Spectroscopic Ruler*. Proceedings of the National Academy of Sciences of the United States of America, 1967. **58**(2): p. 719.
78. Ward, M.D., *Mechanisms of sensitization of lanthanide(III)-based luminescence in transition metal/lanthanide and anthracene/lanthanide dyads.* Coordination Chemistry Reviews, 2010. **254**(21-22): p. 2634-2642.

Chapter 2. X-ray absorption spectroscopy methods and applications

2.1 Introduction

This chapter provides an overview of the x-ray spectroscopy modes used in the studies of lanthanide materials reported in this thesis, particularly x-ray absorption near edge structure (XANES) and high energy resolution fluorescence detection (HERFD). First, x-ray interactions with matter are discussed in general, to provide a basic understanding of the physical and chemical information that can be derived from XANES. We then summarize the current technical reach of time-resolved x-ray spectroscopy, and review the literature on time-resolved XANES (TR-XANES) studies of transition metal complexes, to provide context for the TR-XANES studies of lanthanide complexes covered in chapters 3 and 4. Finally, the theoretical discussion of XANES is extended to discuss the spectral features that can be resolved by moving to HERFD.

2.2 Overview of XANES

A XANES spectrum consists of a measurement of the x-ray absorption coefficient in a ~100 eV band around the binding energy of a core electron. XANES is a well-established technique in condensed matter physics and physical chemistry; common applications include analysis of catalysts [1-5], battery electrodes [6, 7], geological materials [8-10] and biological samples [11-13]. In basic physics, examples of XANES results include studies of electron distribution in alloys [14, 15], structural disorder in nanoparticles [16-18], and phase transitions [19-21]. In general, XANES is sensitive to valence and conduction band structure in solids (and analogously, to bonding orbital structure in molecules); consequently, the spectral features contain information on chemistry and local coordination. In addition, it is an element-specific technique, and uses radiation that penetrates through organic material. These features are important in applied sciences, where samples are often heterogeneous and the ability to perform

measurements *in situ* is a major advantage. Furthermore, in studies of non-isotropic materials, detailed information about orbital ordering can often be obtained by collecting polarization-dependent spectra [12, 19-22]. All of these capabilities can be broadly understood from the following description of x-ray absorption by condensed matter, using a treatment similar to the ones in refs. [23-25].

Experimentally, the quantity to be measured is the absorption coefficient $\mu(\omega)$. This quantity is defined so that a sample of thickness t attenuates photons of energy $\hbar\omega$ by a factor of $e^{-\mu(\omega)t}$. We will focus on energies in the "hard X ray" regime, i.e., between approximately 5 keV and 120 keV. This range covers the K shell binding energies of the 3d transition metals and the L shell binding energies of heavier elements, including the lanthanides. To illustrate, the hard x-ray mass absorption coefficients μ/ρ of Mn and Eu are plotted in Figure 2.1. As the photon energy crosses the binding energy of each core electron, the photoelectric effect produces a sharp step referred to as an "absorption edge." Note that distinct edges are widely separated, which gives XAS its element specificity.

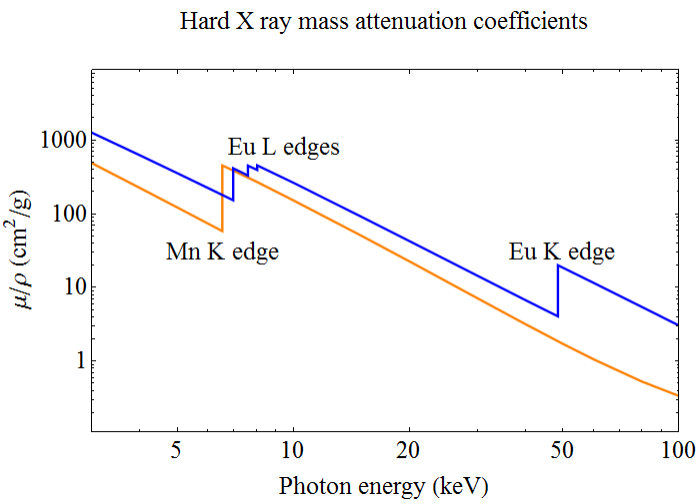

Figure 2.1. Mass attenuation coefficients of a transition metal and a lanthanide in the hard X ray regime. Data obtained from ref. [26].

To write down a description of a photon being absorbed by the sample, we make the simplifying assumption that the photon excites only a one-electron transition. This means that the absorption coefficient is given by Fermi's Golden Rule,

$$\mu(\omega) \propto \sum_f |\langle f|\boldsymbol{p}\cdot\boldsymbol{A}(\boldsymbol{r})|i\rangle|^2 \delta\big(E_f - E_i - \hbar\omega\big), \tag{2.1}$$

where $\boldsymbol{p}$ is the momentum operator, and $\boldsymbol{A}(\boldsymbol{r})$ is the electromagnetic vector potential, and $|i\rangle$ and $|f\rangle$ are the initial and final states of the sample. Following ref. [23], we write each final state as the initial state with the addition of a core hole $\bar{c}$ and a photoelectron e. The sum over f then becomes a sum over possible states of the photoelectron:

$$\mu(\omega) \propto \sum_e |\langle i, e, \bar{c}|\boldsymbol{p}\cdot\boldsymbol{A}(\boldsymbol{r})|i\rangle|^2 \delta(E_e - (\hbar\omega - E_i)). \tag{2.2}$$

Next, we sum over e, and identify the sum of delta functions with a density of states $\rho_{\bar{c}}$. Here, the notation emphasizes the fact that the core hole affects the density of states.

$$\mu(\omega) \propto |\langle \hbar\omega - E_i|\boldsymbol{p}\cdot\boldsymbol{A}(\boldsymbol{r})|i\rangle|^2 \rho_{\bar{c}}(\hbar\omega - E_i). \tag{2.3}$$

This formulation shows explicitly that the absorption near an absorption edge E_i is sensitive to the density of unoccupied states that are available for the photoelectron, i.e. the valence and conduction band structure in a solid, or the valence and bonding orbital structure of the target element in a molecule.

Several considerations prevent a simple interpretation of the measured spectrum as a map of the density of states. First, rewriting $\boldsymbol{p}\cdot\boldsymbol{A}(\boldsymbol{r})$ in the standard multipole expansion shows that the spectrum is dominated by electric dipole transitions. The K edge (1*s*) XANES, for example, primarily measures the *p*-projected density of states; transitions of 1s electrons to *d* orbitals (and *d*-derived bands) are parity-forbidden and will contribute weakly. Second, overlap between core and valence wavefunctions can lead to near-edge spectral features that do not neatly correspond to valence states. Third, the core hole changes the potential of a single atom. In a solid, this

weakly perturbs the band structure but strongly affects the states localized at the absorption site, e.g. the 4*f* states of the lanthanides (see Section 1.2). Fourth, the short lifetime of the core hole causes an intrinsic broadening of the spectrum, further discussed in Section 2.5. Finally, the straightforward one-electron picture used above may break down; corrections for many-body effects and scattering of the photoelectron from multiple atoms are often necessary to reach quantitative agreement between theory and experiment.

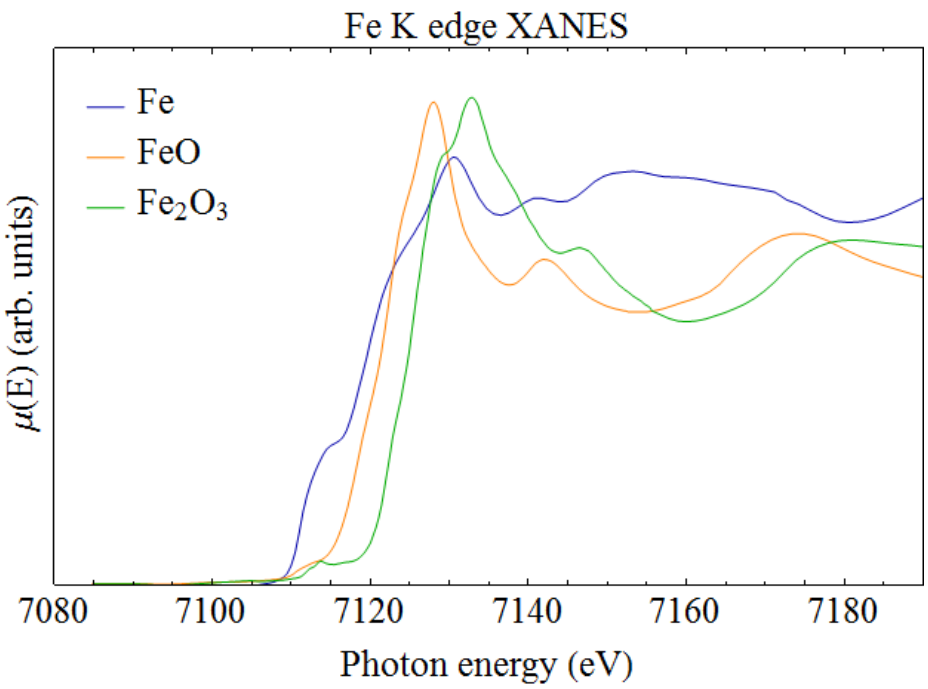

Figure 2.2. Fluorescence-mode XANES collected from Fe foil and two reference Fe oxides (Pacold, Plummer, et al., unpublished data).

With these caveats in mind, it is still possible to at least qualitatively interpret many features of experimental XANES data in terms of band structure (or molecular orbital structure) and local coordination geometry. To illustrate, we now summarize several XANES datasets. Figure 2.2 shows iron K-edge spectra collected from Fe foil and powders of FeO and Fe_2O_3. There is a clear correlation between formal Fe oxidation state and the energy of the absorption

edge. In addition, 1s → 3d transitions produce smaller "pre-edge" features near 7115 eV, with relative spectral weights and positions that are also dependent on Fe valency. Finally, variations in the conduction band structure lead to variations in the functional form of the spectrum above the edge. The strong sensitivity of XANES to oxidation state, particularly in the edge shift, is a mainstay of catalysis studies [1-5, 27, 28].

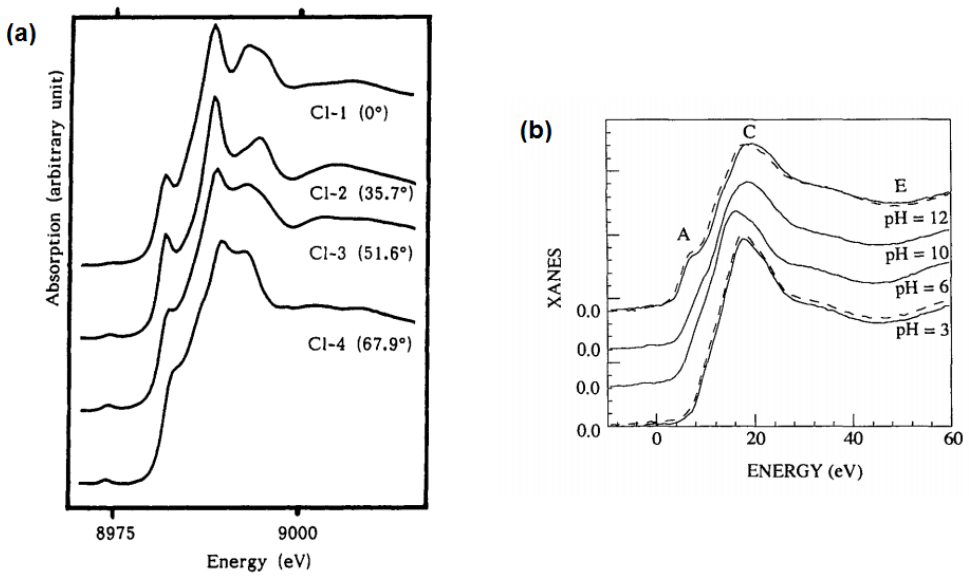

Figure 2.3. Cu K-edge XANES of several Cu complexes. (a) Reproduced from ref. [29], spectra collected from a $[CuCl_4]^{2-}$ in complex with a series of ligands that constrain the position of the Cl atoms, fixing the angle between the two Cl-Cu-Cl planes (in parentheses). (b) Reproduced from ref. [30], spectra of a Cu-ATP complex in solution at varying pH.

Structural displacements alone (i.e. with no formal change in oxidation state and without breaking or formation of bonds) lead to less drastic reorganizations of the valence electrons, and therefore produce smaller but measureable spectral signatures. Figure 2.3a shows copper K-edge spectra collected from a set of Cu^{2+} complexes. In each complex, the Cu^{2+} ion is coordinated to four Cl^- ions. The $[CuCl_4]^{2-}$ subunit is bonded to a ligand which constrains the positions of the Cl- ions, so that they adopt square planar geometry in one complex and distorted tetrahedral geometry in the remaining three. The resulting variation in Cu^{2+} 3d orbital structure leads to a

monotonic increase in the intensity of the 3d-derived pre-edge peak as the dihedral angle increases. A similar pattern appears in Figure 2.3b. Here, the samples were solutions of Cu-ATP complexes. Varying the solution pH causes a distortion of the ATP molecules, again changing the coordination geometry around the Cu without breaking any bonds.

2.3 Ultrafast x-ray spectroscopy

The timescale for atomic motions over angstrom distances is ~100 femtoseconds [31], setting the time resolution needed to study a wide range of elementary chemical and physical processes. This has motivated the development over the past three decades of several experimental techniques with picosecond and sub-picosecond time resolution. Here, in particular, we will discuss the combination of pulsed pump lasers with x-ray probes of structural and electronic dynamics [31, 32]. The time resolution of such studies is currently limited by the length of the X ray pulse; synchrotron beamlines routinely obtain 100-ps resolution [33-36], while sub-picosecond resolution can be achieved at by laser-slicing of the electron bunches at a synchrotron (at the cost of significantly reduced flux) [37-39] and at XFELs [40].

In many time-resolved studies, the scientific goal is to observe the structural rearrangement of atoms in the sample. Time-resolved x-ray diffraction has been used to study lattice dynamics in crystalline materials [41, 42], while small angle x-ray scattering can be used with non-crystalline species, e.g. proteins in the process of folding [43, 44]. Here, we will focus on time-resolved XANES (TR-XANES) results that take advantage of the scope of XANES outlined in the previous section. In particular, we will review several TR-XANES studies of transition metal-organic complexes, to provide context for the studies of lanthanide-organic complexes in the following chapters.

2.3.1 Transition metal-organic complexes

Decades of work towards lowering the cost and scalability of solar energy production have led to the discovery of a broad range of novel photoactive materials and devices [45-52]. One promising example is the dye sensitized solar cell (DSSC); reports of prototype cells by Grätzel and co-workers [53-56] sparked an intensive research effort towards commercialization. In a typical DSSC (Fig. 2.4), the anode is in contact with a mesoporous, nanocrystalline semiconductor film; the surface of the semiconductor is coated with a light-harvesting dye. The dye is kept in electrical contact with the cathode through a redox electrolyte. Absorption of light by the dye places it in an excited state that is capable of transferring an electron into the conduction band of the semiconductor; the charge on the dye is restored by the electrolyte, which in turn accepts electrons from the load circuit.

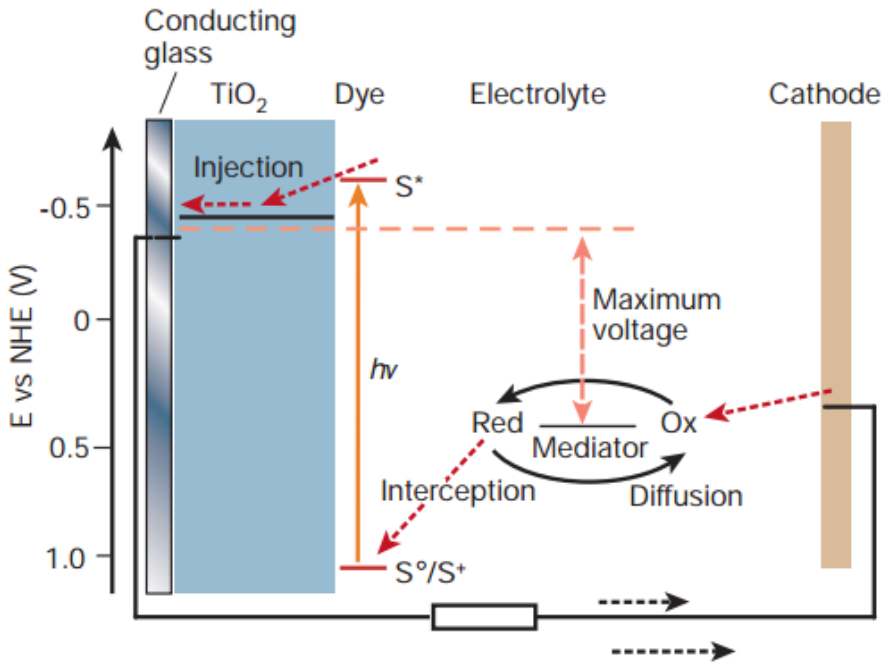

Figure 2.5. Schematic of a dye-sensitized photovoltaic cell, from ref. [54]. Absorption of a photon (hv) causes a light-harvesting dye to inject an electron into the conduction band of a nanocrystalline semiconductor film (here, TiO_2). The load circuit and a redox electrolyte then replenish the charge on the dye.

For commercial viability, the dye must (1) absorb strongly across a broad range of the solar spectrum, (2) have excited states capable of electron transfer to the semiconductor, (3) easily form a monolayer on the surface of the semiconductor, and (4) be stable under long-term exposure to sunlight and rapid redox cycles. Research efforts have focused on engineering organic [57-59] and organometallic [56, 57, 60] dyes to satisfy these criteria. Here, we will concentrate on transition metal-organic complexes, which typically achieve higher solar power conversion efficiency than purely organic dyes and show better long-term stability (though at higher material cost) [61]. In particular, Ru-based dyes have attracted consistent interest over the entire development history of DSSCs [53, 56, 62, 63].

The charge transfer and energy transfer properties of these materials have other potential applications that are the subject of ongoing research. Transition metal complexes have been studied for use in photocatalysis and solar fuel generation (in devices closely related to DSSCs) [54, 64-66]; as electroluminescent materials [57]; and in the construction of molecular-scale optoelectronic and magnetic devices [67-69]. In all of these applications, as well as for DSSCs, it is crucial to understand the excited state dynamics in order to engineer improved materials. To illustrate, we review several representative time-resolved XANES studies.

2.3.2 Examples of TR-XANES studies

Van Kuiken and co-workers [70] reported a laser-pump/x-ray probe study of a Ru-organic solar cell dye in solution, using Ru L_3 edge XANES to probe the 4d bonding orbitals. Photoexcitation of the dye places it in a metal-to-ligand charge transfer (MLCT) state, which relaxes within ~50 fs to a metastable spin-triplet MLCT state (lifetime ~60 ns). Spectra collected from the ground state and the triplet MLCT state are shown in Fig. 2.5. The ground state XANES shows two peaks attributed to transitions into the bonding orbitals of the Ru ion (B) and the

ligand (C). The charge transfer excitation decreases the screening of the Ru nucleus, shifting the 2p and bonding orbitals; this causes the observed shifts to B′ and C′. In addition, the Ru 4d vacancy left by the charge transfer opens a new 2p → 4d x-ray absorption channel. This creates a peak in the excited-state XANES (A′) with no corresponding feature in the ground state.

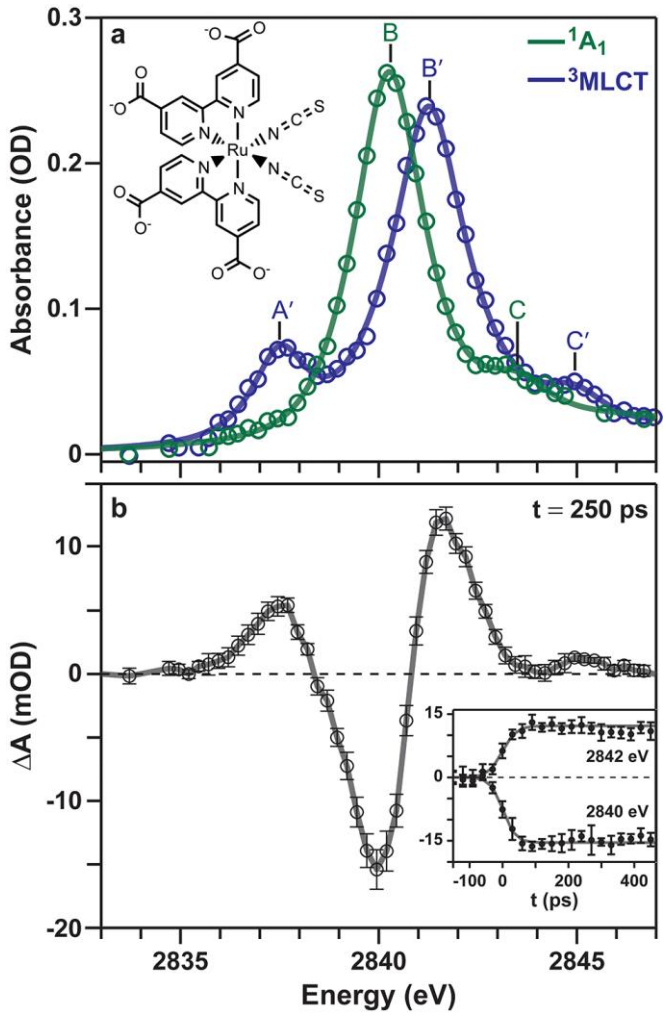

Figure 2.5. From ref. [70]. (a) Ru L_3-edge XANES collected from the solar cell dye N3 in its ground state ($^1A_1$) and metal-to-ligand charge transfer excited state (^{3}MLCT). (b) Difference from the ground-state spectrum 250 ps after the pump pulse. Inset: time-dependent XANES traces at the energies corresponding to the A′ and B features (see main text).

Bressler et al. [71] and Khalil et al. [72] reported on the excited state dynamics of Fe-organic complexes. In each study, steady-state measurements of reference complexes were used to identify structures corresponding to low-spin and high-spin states of the central Fe ion. The structures can be clearly distinguished in the Fe K-edge XANES, due to differences in the Fe-

ligand bond lengths of approximately 0.2 Å (Fig. 2.6; compare this effect with the structural signatures seen in XANES of Cu complexes, Fig. 2.3). The steady-state data were then used to interpret TR-XANES observations of the complexes in solution. In contrast with the Ru complex studied by Van Kuiken et al., the MLCT state is converted into a triplet excitation on the ligand. This transition also returns the charge to the Fe ion, placing it in a high-spin state (Fig. 2.7a). Consequently, there is no edge shift comparable to that observed in the Ru dye. However, the high-spin state is accompanied by a structural distortion, producing a transient XANES signal. The difference of the ground state and high-spin-state XANES corresponds closely with the difference of the reference steady-state spectra (Fig. 2.6b-c). Lemke et al. [40] recently extended this work to finer time resolution by using the sub-picosecond pulses generated by an X ray free electron laser. This made it possible to identify transient features corresponding to the short-lived (~200 fs) MLCT state.

Huse and co-workers [73, 74] performed time-resolved XANES studies of another Fe complex (closely related to those used in refs. [40, 71, 72]), using soft X rays to probe the Fe L edges. This is experimentally more challenging than using the K edges, due to strong attenuation of the X rays by the solvent, but is more sensitive to electronic structure changes in the 3d bonding orbitals, since the signal is dominated by $2p \rightarrow 3d$ transitions. (Recall that in K-edge spectra, the contribution of the 3p shell is suppressed, since $1s \rightarrow 3d$ transitions are parity-forbidden. One way of viewing the distinction is that the Fe K-edge detects changes in atomic motions, while the L edges specifically detect changes in the state of the 3d electrons.) Huse et al. [73, 74] (1) used the total spectral weight across the L edges to confirm that the MLCT state does revert to a state in which the charge returns to the Fe ion, and (2) used the relative spectral weight of the L_2 ($2p_{1/2}$) and L_3 ($2p_{3/2}$) edges to track changes in spin state. As in the K-edge

studies, analysis is assisted by comparison of the ground state and excited state spectra with steady-state models.

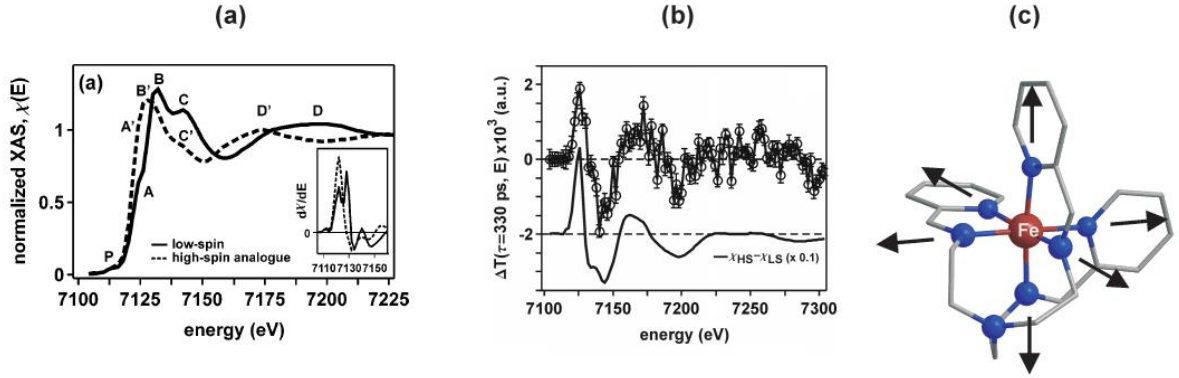

Figure 2.6. Adapted from Khalil et al. [72]. (a) Steady-state Fe K edge XANES of the low-spin complex $[Fe(tren\text{-}(py)_3)](PF_6)_2$ and its high-spin analogue $[Fe(tren(6\text{-}Me\text{-}py)_3)](PF_6)_2$. (b)Open circles: excited – ground state difference from time-resolved XANES measurements of $[Fe(tren(py)_3)](PF_6)_2$ in solution. Solid line: difference of the steady-state spectra from (a). (c) Model of the $[Fe(tren(py)_3)](PF_6)_2$ complex, with arrows indicating the structural distortion that accompanies the high-spin state (as determined by time-resolved EXAFS).

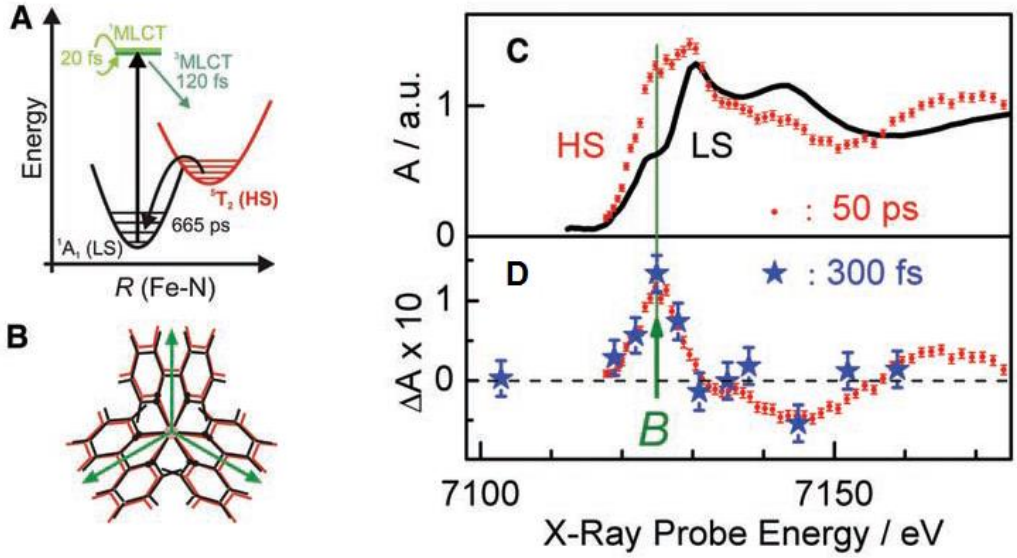

Figure 2.7. Adapted from Bressler et al. [71]. (A) Excited state cascade of the $Fe(bipyridine)_3$ complex. Photoexcitation of the low-spin ground state ($^1A_1$) produces a metal-ligand charge transfer (MLCT) state, which is quickly converted into a high-spin state ($^5T_2$). (B) The high-spin state is accompanied by distortion of the ligand. (C) Fe K-edge XANES of the high-spin and low-spin states and (D) their difference.

2.4 Distinguishing between structural and electronic effects

It is a basic principle of condensed matter physics and physical chemistry that atomic positions affect electronic structure. The arrangement of atomic nuclei in space sets the potential seen by the electrons, and is the starting point for determining band structure in a solid and hybrid orbital structure in a molecule. Atomic motions therefore perturb both the spatial distribution of the electrons and the electronic energy levels. This is a theme of the studies of Fe complexes reviewed above: the dynamics of an electronic signal (XANES) are correlated with structural distortions. Since the physics of interest lie in the dynamics of the electronic excited states, care must be taken to disentangle structural and electronic effects in the observed spectra. This may be done by using structural information from DFT [70] or Raman spectroscopy [75, 76]. Recent work has also shown that time-resolved x-ray emission spectroscopy (which is relatively less sensitive to structural distortions) can provide important complementary information [77, 78].

"Purely electronic" TR-XANES signatures, i.e. transient changes in x-ray absorption that are not associated with structural distortion, are rare but not unprecedented, having been observed in at least two solid-state systems. In GaAs, a pump laser can be used to partially empty the valence band, modifying the density of unoccupied states $\rho_{\bar{c}}$ (see Eq. 2.3) and producing a transient XANES signal [79]. In VO_2, high-fluence photoexcitation has been reported to cause a purely electronic insulator-to-metal phase transition within ~500 fs of the pump pulse [80], followed by a lattice distortion over several picoseconds as the electrons thermalize with the lattice. It should be noted that more recent work calls this result into question: time-resolved electron diffraction data suggest that the lattice reorganization includes an initial sub-picosecond motion along one axis, followed by slower motions along the other axes [81].

These considerations will be important throughout this thesis because many lanthanide systems do not undergo significant structural distortions during the process of luminescence. For example, DFT calculations on the samples studied in Chapter 3 show negligible atomic motions upon excitation of the ligand (less than 0.02 Å, compared to 0.2 Å in the Fe complexes).

2.5 Experimental modes and core hole effects

To conclude the chapter, we discuss the established techniques for collecting XANES data. A schematic of an x-ray absorption experiment is shown in Figure 2.8. A sample of thickness t is placed in a monochromatic beam of photons with energy $\hbar\omega$ and intensity I_0, which is attenuated to intensity $I_T = I_0 e^{-\mu(\omega)t}$. In a transmission-mode measurement, the absorption spectrum is collected by scanning ω and monitoring I_T/I_0 with detectors immediately upstream and downstream of the sample. In a fluorescence-mode measurement, the signal is derived from the intensity I_F of the x-ray fluorescence of the sample, i.e., the radiation emitted as the core holes created by the beam are filled by electrons from higher energy levels. For thin

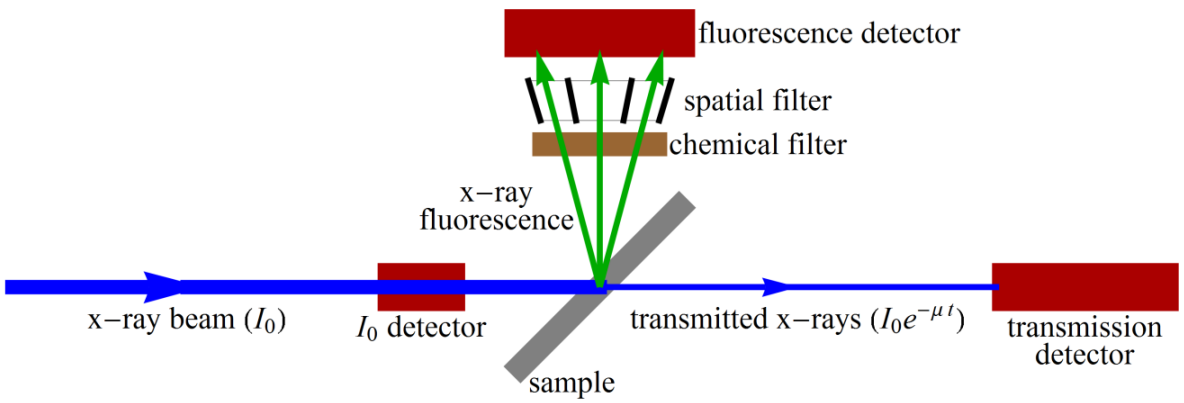

Figure 2.8. Schematic of the experimental setup for x-ray absorption spectroscopy measurements. A beam of X rays passes through a sample of thickness *t* and the resulting attenuation is measured by a pair of detectors upstream and downstream of the sample. Alternatively, the x-ray fluorescence can be used; for thin and dilute samples this is proportional to the absorption and is often experimentally easier to measure. A chemical filter may be used to reject elastic scattering from the sample and pass fluorescence through to the detector, and a spatial filter may be used to reject stray scattering from positions other than the beam spot.

samples, I_F/I_0 is directly proportional to $\mu(\omega)$. This is also true for dilute solutions of the element of interest in weakly absorbing solvents or solid matrices (thick and concentrated samples require corrections for re-absorption of the fluorescence by the sample itself).

Both synchrotron light sources and laboratory-based plasma and tube sources produce broadband x-ray radiation. In order to perform an energy scan as described here, a Bragg monochromator is used to select a narrow, tunable band from the source. A bandwidth of $\Delta E < 2$ eV is typical at the lanthanide L edges (5.5 keV $< E <$ 10.5 keV). Another possibility is to select a broad (> 100 eV) band from the source and perform an energy-dispersive transmission measurement, i.e., to collect complete spectra of the incident and transmitted radiation and use these to calculate $\mu(E)$. All of the XANES datasets presented in this document were collected at a third-generation synchrotron light source, using a scanning monochromator and fluorescence-mode detection. This configuration was chosen since the ~2 mM sample solutions used in most of the experiments would have yielded poor signal-to-background ratios in transmission mode.

2.6 Core hole lifetime suppression

The monochromator bandwidth is not the only limit on the energy resolution of a XANES measurement. The core hole produced by an absorbed X ray has a short lifetime; by the Heisenberg uncertainty principle, this gives the excited state an energy uncertainty, which appears experimentally as a broadening of the entire spectrum. To describe the effect in more detail, we must substantially revise the treatment of x-ray absorption in Section 2.2 to include both an incident and a scattered photon. The core hole state $|i, e, \bar{c}\rangle$ in Eq. (2.2) will now be viewed as an intermediate state, followed by a final state in which the core hole is filled by another electron. For concreteness, following the L-edge studies reported in refs. [82, 83], we will consider one-photon-in/one-photon-out processes, and focus on the case of absorption at the

L_3 ($2p_{3/2}$) edge and $L\alpha_1$ ($3d_{5/2} \rightarrow 2p_{3/2}$) emission. The transition rate, including the widths in energy of the intermediate and final states, is given by the Kramers-Heisenberg formula [84-86]:

$$I(\omega,\omega') \propto \frac{\left|\langle\overline{3d}|\boldsymbol{p}\cdot\boldsymbol{A}(\boldsymbol{r})|\overline{2p}\rangle\langle\overline{2p}|\boldsymbol{p}\cdot\boldsymbol{A}(\boldsymbol{r})|i\rangle\right|^2}{(E_i - E_{\overline{2p}} + \hbar\omega)^2 + \frac{\left(\Gamma_{\overline{2p}}\right)^2}{4}} \cdot \frac{\frac{\Gamma_{\overline{3d}}}{2\pi}}{(E_i - E_{\overline{3d}} + \hbar\omega - \hbar\omega')^2 + \frac{(\Gamma_{\overline{3d}})^2}{4}} \qquad (2.4)$$

Here, $\hbar\omega$ and $\hbar\omega'$ are the energies of the incident and scattered photons, $|\overline{2p}\rangle$ is the intermediate state with a $2p$ core hole, and $|\overline{3d}\rangle$ is the final state with a $3d$ core hole. In the first factor, the lifetime width $\Gamma_{\overline{2p}}$ admits processes in which the energy $\hbar\omega$ of the incident photon does not match the energy difference of the ground and $|\overline{2p}\rangle$ states. For the lanthanide L_3 edges, $\Gamma_{\overline{2p}}$ ranges from 3.48 eV (Ce) to 4.60 eV (Yb) [87], well above the monochromator resolution at modern synchrotron beamlines, and the core hole lifetime therefore causes significant broadening of spectral features in conventional transimission-mode or fluorescence-mode XANES measurements (Fig. 2.9).

The second factor in Eq. 2.4 partially enforces energy conservation. The width $\Gamma_{\overline{3d}}$ (specifically for the $3d_{5/2}$ core hole) is less than 1.6 eV for $Z \leq 70$, which includes the lanthanides [88, 89]. This constrains $\hbar\omega - \hbar\omega'$ to be close to the difference in energy between the L_3 edge and the $L\alpha_1$ emission line (of course, energy must be exactly conserved overall by the process that fills the 3d hole and returns the atom to its ground state). The overall result is resonant Raman scattering of X rays near the edge. An example, at the terbium L_3 edge, is shown in Figure 2.9. When $\hbar\omega$ is sufficiently far above the edge, the fluorescence peak at $\hbar\omega' = E_{L\alpha_1}$ dominates the spectrum. For $\hbar\omega$ near the edge, however, the spectrum shows an inelastic scattering peak that shifts so that the energy transfer $\hbar\omega - \hbar\omega'$ stays constant.

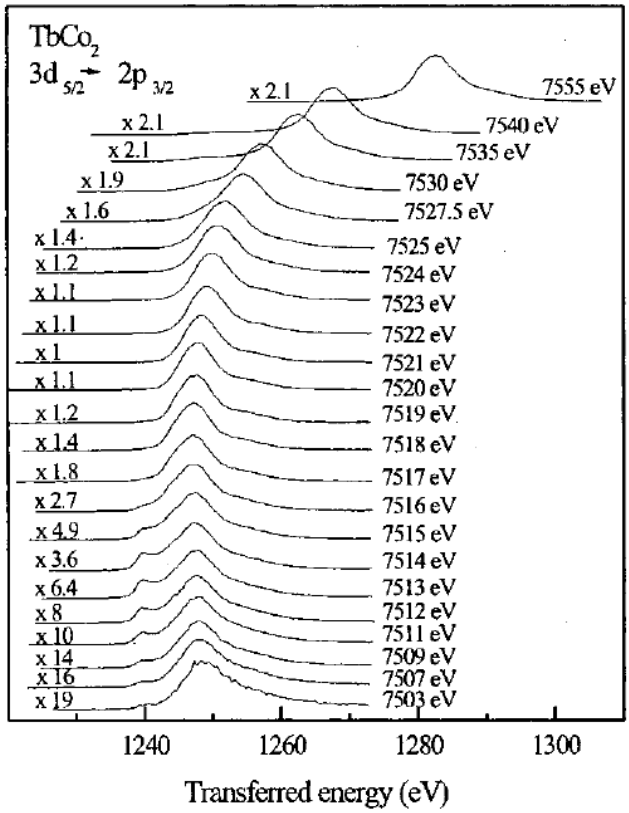

Figure 2.9. Resonant inelastic x-ray scattering of $TbCo_2$ near the Tb L_3 edge, from ref. [90]. Each trace is labeled with the incident photon energy; note that the horizontal axis is the transferred energy (rather than the detected photon energy).

This suggests an experimental approach to suppression of the 2p core hole broadening. The strategy is to only detect photons $\hbar\omega'$ in a narrow band around $E_{\mathrm{L}\alpha_1}$, so that the energy transfer condition constrains $\hbar\omega$. Then $\Gamma_{\overline{3d}}$, rather than $\Gamma_{\overline{2p}}$, becomes the intrinsic limit of the spectral resolution. This method is referred to as high energy resolution fluorescence detection (HERFD) and is typically implemented with a Bragg crystal analyzer. Early HERFD studies showed that it is possible to resolve pre-edge spectral features in the L_3 edge XANES of several lanthanides [82, 91, 92] which are not visible in transmission-mode and total-fluorescence data (Fig. 2.10). The pre-edge region can be assigned to quadrupolar 2p → 4f transitions; in light of

the rich physical properties of the lanthanide 4f electrons, this is particularly interesting for the broader purpose of understanding lanthanide electronic structure. HERFD has also produced interesting results on transition metal systems, for example in L-edge studies of Pt catalysts [83, 93, 94].

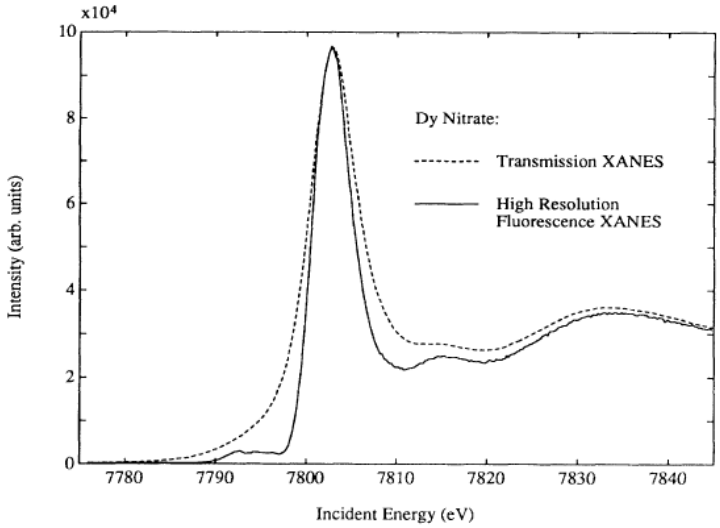

Figure 2.10. "Conventional" transmission-mode XANES and HERFD-mode xanes at the L_3 edge of Dy, reproduced from ref. [82]. Note the pre-edge feature centered near 7795 eV resolved in the HERFD spectrum, which corresponds to electric quadrupole 2p → 4f transitions.

2.7 References

1. Ankudinov, A.L., et al., *Effect of hydrogen adsorption on the x-ray absorption spectra of small Pt clusters.* Physical Review Letters, 2001. **86**(8): p. 1642-1645.
2. Coulston, G.W., et al., *The kinetic significance of V^{5+} in n-butane oxidation catalyzed by vanadium phosphates.* Science, 1997. **275**(5297): p. 191-193.
3. Ricchiardi, G., et al., *Vibrational structure of titanium silicate catalysts. A spectroscopic and theoretical study.* Journal of the American Chemical Society, 2001. **123**(46): p. 11409-11419.
4. Liang, Y.Y., et al., *Covalent Hybrid of Spinel Manganese-Cobalt Oxide and Graphene as Advanced Oxygen Reduction Electrocatalysts.* Journal of the American Chemical Society, 2012. **134**(7): p. 3517-3523.
5. Kanan, M.W., et al., *Structure and Valency of a Cobalt-Phosphate Water Oxidation Catalyst Determined by in Situ X-ray Spectroscopy.* Journal of the American Chemical Society, 2010. **132**(39): p. 13692-13701.
6. Yoon, W.S., et al., *Investigation of the charge compensation mechanism on the electrochemically Li-ion deintercalated $Li_{1-x}Co_{1/3}Ni_{1/3}Mn_{1/3}O_2$ electrode system by*

combination of soft and hard x-ray absorption spectroscopy. Journal of the American Chemical Society, 2005. **127**(49): p. 17479-17487.
7. Yabuuchi, N., et al., *Detailed Studies of a High-Capacity Electrode Material for Rechargeable Batteries, Li_2MnO_3-$LiCo_{1/3}Ni_{1/3}Mn_{1/3}O_2$.* Journal of the American Chemical Society, 2011. **133**(12): p. 4404-4419.
8. Berry, A.J., et al., *Oxidation state of iron in komatiitic melt inclusions indicates hot Archaean mantle.* Nature, 2008. **455**(7215): p. 960-U42.
9. Chisholmbrause, C.J., et al., *Evidence for Multinuclear Metal-Ion Complexes at Solid Water Interfaces from X-Ray Absorption-Spectroscopy.* Nature, 1990. **348**(6301): p. 528-531.
10. Waychunas, G.A., et al., *Evidence from X-Ray Absorption for Network-Forming Fe^{2+} in Molten Alkali Silicates.* Nature, 1988. **332**(6161): p. 251-253.
11. Ade, H., et al., *Chemical Contrast in X-Ray Microscopy and Spatially Resolved XANES Spectroscopy of Organic Specimens.* Science, 1992. **258**(5084): p. 972-975.
12. Bianconi, A., et al., *The Co Bond Angle of Carboxymyoglobin Determined by Angular-Resolved Xanes Spectroscopy.* Nature, 1985. **318**(6047): p. 685-687.
13. Parsons, J.G., M.V. Aldrich, and J.L. Gardea-Torresdey, *Environmental and biological applications of extended X-ray absorption fine structure (EXAFS) and X-ray absorption near edge structure (XANES) spectroscopies.* Applied Spectroscopy Reviews, 2002. **37**(2): p. 187-222.
14. Coulthard, I. and T.K. Sham, *Charge redistribution in Pd-Ag alloys from a local perspective.* Physical Review Letters, 1996. **77**(23): p. 4824-4827.
15. Booth, C.H., et al., *Multiconfigurational nature of 5f orbitals in uranium and plutonium intermetallics.* Proceedings of the National Academy of Sciences of the United States of America, 2012. **109**(26): p. 10205-10209.
16. Hamad, K.S., et al., *Structural disorder in colloidal InAs and CdSe nanocrystals observed by X-ray absorption near-edge spectroscopy.* Physical Review Letters, 1999. **83**(17): p. 3474-3477.
17. Han, S.W., et al., *Lattice disorder and size-induced Kondo behavior in $CeAl_2$ and $CePt_{2+x}$.* Physical Review Letters, 2006. **97**(9).
18. Stern, E.A., et al., *Are Nanophase Grain-Boundaries Anomalous.* Physical Review Letters, 1995. **75**(21): p. 3874-3877.
19. Murakami, Y., et al., *Direct observation of charge and orbital ordering in $La_{0.5}Sr_{1.5}MnO_4$.* Physical Review Letters, 1998. **80**(9): p. 1932-1935.
20. Murakami, Y., et al., *Resonant X-ray scattering from orbital ordering in $LaMnO_3$.* Physical Review Letters, 1998. **81**(3): p. 582-585.
21. Haverkort, M.W., et al., *Orbital-assisted metal-insulator transition in VO_2.* Physical Review Letters, 2005. **95**(19): p. 6404.
22. Koethe, T.C., et al., *Transfer of spectral weight and symmetry across the metal-insulator transition in VO_2.* Physical Review Letters, 2006. **97**(11): p. 6402.
23. de Groot, F., *High resolution X-ray emission and X-ray absorption spectroscopy.* Chemical Reviews, 2001. **101**(6): p. 1779-1808.
24. Rehr, J.J. and R.C. Albers, *Theoretical approaches to x-ray absorption fine structure.* Reviews of Modern Physics, 2000. **72**(3): p. 621-654.

25. Degroot, F.M.F., *X-Ray-Absorption and Dichroism of Transition-Metals and Their Compounds.* Journal of Electron Spectroscopy and Related Phenomena, 1994. **67**(4): p. 529-622.
26. Hubbell, J.H. and S.M. Seltzer, *Tables of X-Ray Mass Attenuation Coefficients and Mass Energy-Absorption Coefficients from 1 keV to 20 MeV for Elements Z = 1 to 92 and 48 Additional Substances of Dosimetric Interest.* 1996.
27. Hu, H.C., I.E. Wachs, and S.R. Bare, *Surface-Structures of Supported Molybdenum Oxide Catalysts - Characterization by Raman and Mo L_3-Edge Xanes.* Journal of Physical Chemistry, 1995. **99**(27): p. 10897-10910.
28. Gao, X.T., et al., *Preparation and in-situ spectroscopic characterization of molecularly dispersed titanium oxide on silica.* Journal of Physical Chemistry B, 1998. **102**(29): p. 5653-5666.
29. Sano, M., S. Komorita, and H. Yamatera, *Xanes Spectra of Copper(II) Complexes - Correlation of the Intensity of the 1s-3d Transition and the Shape of the Complex.* Inorganic Chemistry, 1992. **31**(3): p. 459-463.
30. Palladino, L., et al., *X-Ray Absorption near Edge Structure (XANES) of Cu(II)-ATP and Related-Compounds in Solution - Quantitative-Determination of the Distortion of the Cu Site.* Journal of Chemical Physics, 1993. **98**(4): p. 2720-2726.
31. Zewail, A.H., *Femtochemistry: Atomic-scale dynamics of the chemical bond.* Journal of Physical Chemistry A, 2000. **104**(24): p. 5660-5694.
32. Bressler, C. and M. Chergui, *Ultrafast X-ray absorption spectroscopy.* Chemical Reviews, 2004. **104**(4): p. 1781-1812.
33. Ihee, H., et al., *Ultrafast x-ray diffraction of transient molecular structures in solution.* Science, 2005. **309**(5738): p. 1223-1227.
34. Cammarata, M., et al., *Tracking the structural dynamics of proteins in solution using time-resolved wide-angle X-ray scattering.* Nature Methods, 2008. **5**(10): p. 881-886.
35. Schotte, F., et al., *Watching a protein as it functions with 150-ps time-resolved X-ray crystallography.* Science, 2003. **300**(5627): p. 1944-1947.
36. Wohri, A.B., et al., *Light-Induced Structural Changes in a Photosynthetic Reaction Center Caught by Laue Diffraction.* Science, 2010. **328**(5978): p. 630-633.
37. Fritz, D.M., et al., *Ultrafast bond softening in bismuth: Mapping a solid's interatomic potential with X-rays.* Science, 2007. **315**(5812): p. 633-636.
38. Daranciang, D., et al., *Ultrafast Photovoltaic Response in Ferroelectric Nanolayers.* Physical Review Letters, 2012. **108**(8): p. 7601.
39. Johnson, S.L., et al., *Full Reconstruction of a Crystal Unit Cell Structure during Coherent Femtosecond Motion.* Physical Review Letters, 2009. **103**(20): p. 5501.
40. Lemke, H.T., et al., *Femtosecond X-ray Absorption Spectroscopy at a Hard X-ray Free Electron Laser: Application to Spin Crossover Dynamics.* Journal of Physical Chemistry A, 2013. **117**(4): p. 735-740.
41. Rose-Petruck, C., et al., *Picosecond-milliangstrom lattice dynamics measured by ultrafast X-ray diffraction.* Nature, 1999. **398**(6725): p. 310-312.
42. Cavalleri, A., et al., *Anharmonic lattice dynamics in germanium measured with ultrafast x-ray diffraction.* Physical Review Letters, 2000. **85**(3): p. 586-589.
43. Pollack, L., et al., *Compactness of the denatured state of a fast-folding protein measured by submillisecond small-angle x-ray scattering.* Proceedings of the National Academy of Sciences of the United States of America, 1999. **96**(18): p. 10115-10117.

44. Pollack, L., et al., *Time resolved collapse of a folding protein observed with small angle x-ray scattering.* Physical Review Letters, 2001. **86**(21): p. 4962-4965.
45. Tang, C.W., *2-Layer Organic Photovoltaic Cell.* Applied Physics Letters, 1986. **48**(2): p. 183-185.
46. Groves, C., O.G. Reid, and D.S. Ginger, *Heterogeneity in Polymer Solar Cells: Local Morphology and Performance in Organic Photovoltaics Studied with Scanning Probe Microscopy.* Accounts of Chemical Research, 2010. **43**(5): p. 612-620.
47. Peumans, P., S. Uchida, and S.R. Forrest, *Efficient bulk heterojunction photovoltaic cells using small-molecular-weight organic thin films.* Nature, 2003. **425**(6954): p. 158-162.
48. Huynh, W.U., J.J. Dittmer, and A.P. Alivisatos, *Hybrid nanorod-polymer solar cells.* Science, 2002. **295**(5564): p. 2425-2427.
49. Gur, I., et al., *Air-stable all-inorganic nanocrystal solar cells processed from solution.* Science, 2005. **310**(5747): p. 462-465.
50. Hermann, A.M., *Polycrystalline thin-film solar cells - A review.* Solar Energy Materials and Solar Cells, 1998. **55**(1-2): p. 75-81.
51. Stanbery, B.J., *Copper indium selenides and related materials for photovoltaic devices.* Critical Reviews in Solid State and Materials Sciences, 2002. **27**(2): p. 73-117.
52. Yu, G., et al., *Polymer Photovoltaic Cells - Enhanced Efficiencies Via a Network of Internal Donor-Acceptor Heterojunctions.* Science, 1995. **270**(5243): p. 1789-1791.
53. O'Regan, B. and M. Gratzel, *A Low-Cost, High-Efficiency Solar-Cell Based on Dye-Sensitized Colloidal TiO_2 Films.* Nature, 1991. **353**(6346): p. 737-740.
54. Gratzel, M., *Photoelectrochemical cells.* Nature, 2001. **414**(6861): p. 338-344.
55. Hagfeldt, A. and M. Gratzel, *Molecular photovoltaics.* Accounts of Chemical Research, 2000. **33**(5): p. 269-277.
56. Desilvestro, J., et al., *Highly Efficient Sensitization of Titanium-Dioxide.* Journal of the American Chemical Society, 1985. **107**(10): p. 2988-2990.
57. Kalyanasundaram, K. and M. Gratzel, *Applications of functionalized transition metal complexes in photonic and optoelectronic devices.* Coordination Chemistry Reviews, 1998. **177**: p. 347-414.
58. Ito, S., et al., *High-efficiency organic-dye-sensitized solar cells controlled by nanocrystalline-TiO_2 electrode thickness.* Advanced Materials, 2006. **18**(9): p. 1202-+.
59. Schmidt-Mende, L., et al., *Organic dye for highly efficient solid-state dye-sensitized solar cells.* Advanced Materials, 2005. **17**(7): p. 813.
60. Mathew, S., et al., *Dye-sensitized solar cells with 13% efficiency achieved through the molecular engineering of porphyrin sensitizers.* Nature Chemistry, 2014. **6**(3): p. 242-247.
61. Gratzel, M., *Recent Advances in Sensitized Mesoscopic Solar Cells.* Accounts of Chemical Research, 2009. **42**(11): p. 1788-1798.
62. Nazeeruddin, M.K., et al., *Conversion of Light to Electricity by Cis-X_2bis(2,2'-Bipyridyl-4,4'-Dicarboxylate)Ruthenium(II) Charge-Transfer Sensitizers (X = Cl-, Br-, I-, Cn-, and Scn-) on Nanocrystalline TiO_2 Electrodes.* Journal of the American Chemical Society, 1993. **115**(14): p. 6382-6390.
63. Amadelli, R., et al., *Design of Antenna-Sensitizer Polynuclear Complexes - Sensitization of Titanium-Dioxide with $[Ru(Bpy)_2(Cn)_2]_2Ru(Bpy(CoO)_2)_2^{2-}$.* Journal of the American Chemical Society, 1990. **112**(20): p. 7099-7103.

64. Rosenthal, J., et al., *Oxygen and hydrogen photocatalysis by two-electron mixed-valence coordination compounds.* Coordination Chemistry Reviews, 2005. **249**(13-14): p. 1316-1326.
65. Linsebigler, A.L., G.Q. Lu, and J.T. Yates, *Photocatalysis on TiO_2 Surfaces - Principles, Mechanisms, and Selected Results.* Chemical Reviews, 1995. **95**(3): p. 735-758.
66. Kim, D. and A. Osuka, *Directly linked porphyrin arrays with tunable excitonic interactions.* Accounts of Chemical Research, 2004. **37**(10): p. 735-745.
67. Holten, D., D.F. Bocian, and J.S. Lindsey, *Probing electronic communication in covalently linked multiporphyrin arrays. A guide to the rational design of molecular photonic devices.* Accounts of Chemical Research, 2002. **35**(1): p. 57-69.
68. Hirayama, D., et al., *Large photocurrent generation of gold electrodes modified with [60]fullerene-linked oligothiophenes bearing a tripodal rigid anchor.* Journal of the American Chemical Society, 2002. **124**(4): p. 532-533.
69. Otsubo, T., Y. Aso, and K. Takimiya, *Functional oligothiophenes as advanced molecular electronic materials.* Journal of Materials Chemistry, 2002. **12**(9): p. 2565-2575.
70. Van Kuiken, B.E., et al., *Probing the Electronic Structure of a Photoexcited Solar Cell Dye with Transient X-ray Absorption Spectroscopy.* Journal of Physical Chemistry Letters, 2012. **3**(12): p. 1695-1700.
71. Bressler, C., et al., *Femtosecond XANES Study of the Light-Induced Spin Crossover Dynamics in an Iron(II) Complex.* Science, 2009. **323**(5913): p. 489-492.
72. Khalil, M., et al., *Picosecond X-ray absorption spectroscopy of a photoinduced iron(II) spin crossover reaction in solution.* Journal of Physical Chemistry A, 2006. **110**(1): p. 38-44.
73. Huse, N., et al., *Photo-Induced Spin-State Conversion in Solvated Transition Metal Complexes Probed via Time-Resolved Soft X-ray Spectroscopy.* Journal of the American Chemical Society, 2010. **132**(19): p. 6809-6816.
74. Huse, N., et al., *Femtosecond Soft X-ray Spectroscopy of Solvated Transition-Metal Complexes: Deciphering the Interplay of Electronic and Structural Dynamics.* Journal of Physical Chemistry Letters, 2011. **2**(8): p. 880-884.
75. Smeigh, A.L., et al., *Femtosecond Time-Resolved Optical and Raman Spectroscopy of Photoinduced Spin Crossover: Temporal Resolution of Low-to-High Spin Optical Switching.* Journal of the American Chemical Society, 2008. **130**(43): p. 14105-+.
76. Monat, J.E. and J.K. McCusker, *Femtosecond excited-state dynamics of an iron(II) polypyridyl solar cell sensitizer model.* Journal of the American Chemical Society, 2000. **122**(17): p. 4092-4097.
77. Vanko, G., et al., *Picosecond Time-Resolved X-Ray Emission Spectroscopy: Ultrafast Spin-State Determination in an Iron Complex.* Angewandte Chemie-International Edition, 2010. **49**(34): p. 5910-5912.
78. Zhang, W.K., et al., *Tracking excited-state charge and spin dynamics in iron coordination complexes.* Nature, 2014. **509**(7500): p. 345.
79. Adams, B.W., et al., *Picosecond laser-pump, x-ray probe spectroscopy of GaAs.* Review of Scientific Instruments, 2002. **73**(12): p. 4150-4156.
80. Cavalleri, A., et al., *Band-selective measurements of electron dynamics in VO_2 using femtosecond near-edge x-ray absorption.* Physical Review Letters, 2005. **95**(6): p. 7405.
81. Baum, P., D.S. Yang, and A.H. Zewail, *4D visualization of transitional structures in phase transformations by electron diffraction.* Science, 2007. **318**(5851): p. 788-792.

82. Hamalainen, K., et al., *Elimination of the Inner-Shell Lifetime Broadening in X-Ray-Absorption Spectroscopy.* Physical Review Letters, 1991. **67**(20): p. 2850-2853.
83. de Groot, F.M.F., M.H. Krisch, and J. Vogel, *Spectral sharpening of the Pt L edges by high-resolution x-ray emission.* Physical Review B, 2002. **66**(19): p. 5112.
84. Kotani, A. and S. Shin, *Resonant inelastic x-ray scattering spectra for electrons in solids.* Reviews of Modern Physics, 2001. **73**(1): p. 203-246.
85. Gel'mukhanov, F. and H. Agren, *Resonant X-ray Raman scattering.* Physics Reports-Review Section of Physics Letters, 1999. **312**(3-6): p. 87-330.
86. Eisenberger, P., P.M. Platzman, and H. Winick, *X-Ray Resonant Raman-Scattering - Observation of Characteristic Radiation Narrower Than Lifetime Width.* Physical Review Letters, 1976. **36**(11): p. 623-626.
87. Krause, M.O. and J.H. Oliver, *Natural Widths of Atomic K-Levels and L-Levels,K-Alpha X-Ray-Lines and Several Kll Auger Lines.* Journal of Physical and Chemical Reference Data, 1979. **8**(2): p. 329-338.
88. Fuggle, J.C. and S.F. Alvarado, *Core-Level Lifetimes as Determined by X-Ray Photoelectron-Spectroscopy Measurements.* Physical Review A, 1980. **22**(4): p. 1615-1624.
89. Mcguire, E.J., *Atomic M-Shell Coster-Kronig, Auger, and Radiative Rates, and Fluorescence Yields for Ca-Th.* Physical Review a-General Physics, 1972. **5**(3): p. 1043-&.
90. Dallera, C., et al., *Resonant inelastic x-ray scattering at the L-2 and L-3 edge of terbium in TbCo2 and TbF3.* Physical Review B, 2000. **62**(11): p. 7093-7097.
91. Krisch, M.H., et al., *Evidence for a Quadrupolar Excitation Channel at the L_{III} Edge of Gadolinium by Resonant Inelastic X-Ray Scattering.* Physical Review Letters, 1995. **74**(24): p. 4931-4934.
92. Krisch, M.H., et al., *X-ray resonant Raman scattering from $Gd_3Fe_5O_{12}$.* Journal of Electron Spectroscopy and Related Phenomena, 1997. **86**(1-3): p. 159-164.
93. Safonova, O.V., et al., *Identification of CO adsorption sites in supported Pt catalysts using high-energy-resolution fluorescence detection X-ray spectroscopy.* Journal of Physical Chemistry B, 2006. **110**(33): p. 16162-16164.
94. Friebel, D., et al., *In situ X-ray probing reveals fingerprints of surface platinum oxide.* Physical Chemistry Chemical Physics, 2011. **13**(1): p. 262-266.

Chapter 3. Direct Observation of 4f Intrashell Excitation in Luminescent Eu Complexes by Time-Resolved X-ray Absorption Near Edge Spectroscopy

The text of this chapter is adapted from ref. [1], by Joseph I. Pacold,[†] David S. Tatum,[‡] Gerald T. Seidler,[†] Kenneth N. Raymond,[‡] Xiaoyi Zhang,[‖] Andrew B. Stickrath,[#, §] and Devon R. Mortensen[†]. The published paper and supporting information have been combined; some introductory information has been moved to the general discussion of luminescence in Chapter 1, particularly details on the UV/visible spectroscopic determination of the energy transfer efficiency.

[†]Department of Physics, University of Washington, Seattle, Washington 98195, United States
[‡]Chemical Sciences Division, Lawrence Berkeley National Laboratories, Berkeley, California 94720, United States, and Department of Chemistry, University of California, Berkeley, California 94720, United States
[‖]X-ray Science Division, Argonne National Laboratory, Argonne, Illinois 60439, United States
[#]Department of Chemistry, Northwestern University, Evanston, Illinois 60208, United States, and Chemical Sciences and Engineering Division, Argonne National Laboratory, Argonne, Illinois 60439, United States

Abstract

We report time-resolved X-ray absorption near edge structure (TR-XANES) measurements at the Eu L_3 edge upon photoexcitation of several Eu^{III}-based luminescent lanthanide complexes. We find an unambiguous signature of the 4f intrashell excitation that occurs upon energy transfer from the photoactive organic antennas to the lanthanide species. Phenomenologically, this observation provides the basis for direct investigation of a crucial step in the energy transfer pathways that lead to sensitized luminescence in lanthanide-based dyes. Interestingly, the details of the TR-XANES feature suggest that the degree of 4f-5d hybridization may itself vary depending on the excited state of the Eu^{III} ion.

3.1 Introduction

The photophysical properties of the lanthanides and applications of lanthanide luminescence were covered in Chapter 1. Here, we briefly review the main points. Despite the development of numerous applications [2-7], elucidating the energy transfer pathways in luminescent lanthanide materials remains challenging. Most of these systems exploit transitions within the partially filled 4f shells of the trivalent lanthanide ions (denoted Ln^{III}). The optical cross-sections for direct excitation (or de-excitation) of 4f-4f transitions are very weak, since they are electric dipole forbidden by parity and, in some cases, by spin. It is more efficient to indirectly excite the lanthanide by coupling to a sensitizer, i.e., another species that strongly absorbs photons and then transfers energy nonradiatively to the lanthanide [8-10].

In order to rationally design efficient luminescent lanthanide materials, it is crucial to understand the underlying mechanisms of energy transfer (which vary from system to system). After initial photoexcitation, the sensitizer may undergo intersystem crossing to lower energy excited states before transferring energy to the lanthanide, creating uncertainty about which particular states contribute most. There are several possible mechanisms for the ligand to Ln^{III} energy transfer, such as: resonant Coulomb interactions including Förster dipole-dipole transfer and resonance between higher multipole transitions [11, 12], or charge exchange (Dexter transfer) [13]. Resonance conditions and selection rules may constrain these possibilities, but it is often not clear *a priori* which mechanism is dominant [14-17]. Following energy transfer, the excited state of the lanthanide may relax to a lower excited state before emitting a photon, or be nonradiatively quenched without any photoemission [18-20].

Here, we report a time-resolved X-ray absorption near edge spectroscopy (TR-XANES) signature of the ligand-to-lanthanide energy transfer (ET) step in a set of luminescent Eu^{III}

complexes. Specifically, we find that photoexcitation of the sensitizing ligand leads to a long-lived (ms) transient change in the XANES at the Eu L_3 ($2p_{3/2}$) edge, and that the magnitude of the change is correlated with the efficiency of the ligand-to-lanthanide ET. TR-XANES directly interrogates the metal ion and is complementary to time-resolved optical measurements that indirectly provide information about the ET step. While the result we report here is a purely phenomenological observation, we aim to use this ultrafast technique as a time-resolved probe for the excited state electronic structure of Eu^{III} and other lanthanides, toward establishing a more detailed understanding of energy transfer in these systems.

Over the past two decades, TR-XANES has emerged as a powerful technique for studies of transient photo-induced effects, including chemical reactions [21, 22] and spin crossover in photoactive transition metal complexes [23-26]. All of these phenomena involve significant distortions in local structure (e.g. dissociation, or bond length changes larger than 0.1 Å) that are driven by interatomic charge transfer or by electronic occupancy changes in bonding orbitals. Here, we find that TR-XANES can be used to observe a qualitatively different process, the nonradiative transfer of energy to a lanthanide ion, involving no intermediate charge transfer state. Because the long-lived Eu^{III} excitation is confined to *non*bonding 4f orbitals, we expect no significant structural change relative to the ground state at the 100-μs timescale of the observed signal. The nonbonding nature of the 4f orbitals is well documented and self-evident from the atomic-like spectroscopic properties, which is why atomic term symbols are used to label the observed transitions. We note that lanthanide phosphors in general, including those that are sensitized via intermediate charge transfer states, show no difference in configuration coordinate between 4f intrashell excited states [27-29]. It is therefore interesting that we observe a clear TR-XANES feature at all.

The functional form of the transient signal raises questions about the nature of 4f coupling to other atomic orbitals and to the local environment (e.g. the ligand). In particular, we consider whether the degree of 4f mixing with the bonding s- and d-orbitals, and consequently the energies of the nominal 4f and 5d manifolds, may itself be a function of 4f excitation.

Luminescent lanthanide dyes [30-40] such as the ones used in this study provide an illustration of the difficulties involved in understanding the photophysics of a general luminescent lanthanide system. An organic ligand attached to a trivalent lanthanide ion (Eu^{III} here) serves as a light-harvesting antenna [8, 32, 41] by absorbing broadband UV light (Figure 3.1). Ideally, this excitation is eventually transferred to the Eu^{III}, which can later emit a visible photon (Figure 3.1a). The quantum efficiency of this process is limited by the existence of other pathways for radiative and non-radiative dissipation of energy, which we will now summarize. The initial excited singlet state (S) of the ligand may quickly undergo intersystem crossing to the triplet state (T). However, it may also transfer energy directly to the lanthanide, or decay back to the ground state (Figure 3.1c). When sufficient coupling exists between the ligand and the Eu^{III} ion, a portion of the energy in the ligand S or T state is converted to a 4f intrashell excitation on the Eu^{III}.

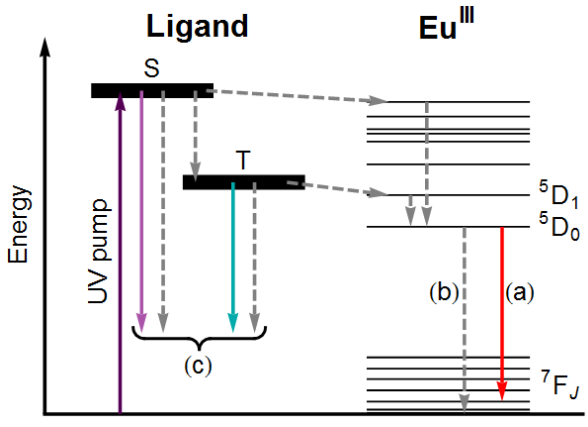

Figure 3.1. A schematic representation of the different possible energy transfer pathways in photo-active luminescent lanthanide complexes. Solid arrows represent radiative transitions, while dashed arrows represent nonradiative transitions. Three possible outcomes of photoexcitation (a, b, c) are described in the text.

The long-lived Eu^{III} excited state requires substantial isolation from solvent species that have vibrational modes capable of quenching the excitation through nonradiative channels [18-20] (Figure 3.1b). Ligands used for lanthanide luminescence must therefore be carefully designed to minimize non-radiative solvent coupling. In cases where the excited lanthanide is not quenched, the lanthanide may emit a photon upon 4f intrashell de-excitation along narrow, atomic-like emission lines (Figure 3.1a). In this final emission step, the intensities of certain 4f-4f transitions, the "hypersensitive" lines (e.g. $^5D_0$ to $^7F_2$ of Eu^{III}), are strongly dependent on the local environment of the lanthanide atom [10, 42-44].

Each step in this process has been investigated experimentally by UV/visible spectroscopy [10, 18, 45-47] and by extensive theoretical calculations [48-52]. The overall efficiency of the antenna-to-lanthanide energy transfer in several complexes has been estimated through calculations based on optical photoemission measurements (as outlined under "Materials and Methods") and on the efficiency of energy transfer to a second fluorescent species [53]. Additionally, transient absorption measurements have been used to determine the lifetimes of the various ligand excited states responsible for energy transfer [46, 54]. There have been no complementary metal-specific absorption spectroscopy observations of the lanthanide excited state electronic structure, likely due to the very weak, dipole-forbidden nature of the 4f intrashell transitions.

3.2 Materials and Methods

The samples are listed in Table 3.1. The three ligands are similar in that they each bear two 1-hydroxypyridin-2-one amide antennas (Table 3.1, shown in blue) which bind the Eu^{III} ion through both types of pyridyl oxygen donors. Each ligand has four donors, leading to 8-coordinate 1:2 metal:ligand complexes in the solid state [36, 55]. Note that upon solvation, the

Table 3.1. Ligand structures and photophysical parameters of the luminescent Eu^{III} complexes.

	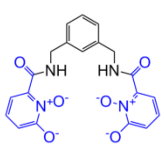 L^1	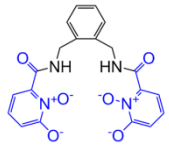 L^2	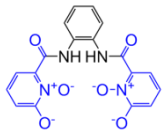 L^3
Complex	$[Eu(L^1)_2]^-$	$[Eu(L^2)_2]^-$	$[Eu(L^3)_2]^-$
λ_{max} **(nm)**	333	337	342
ε_{max} **($M^{-1}cm^{-1}$)**	22,000	19,000	21,000
τ_{obs} **H_2O (µs)**	733	234	536
τ_{obs} **D_2O (µs)**	1022	317	734
Φ_{tot} **H_2O**	0.22	0.051	0.062
τ_{rad} **(µs)**	1680	1740	1470
k_{rad} **(s^{-1})**	596	573	680
k_{nonrad} **(s^{-1})**	768	3700	1190
η_{Eu}	0.436	0.134	0.365
η_{sens}	0.500	0.380	0.170
q **(# of H_2O)**	0.1	0.9	0.2

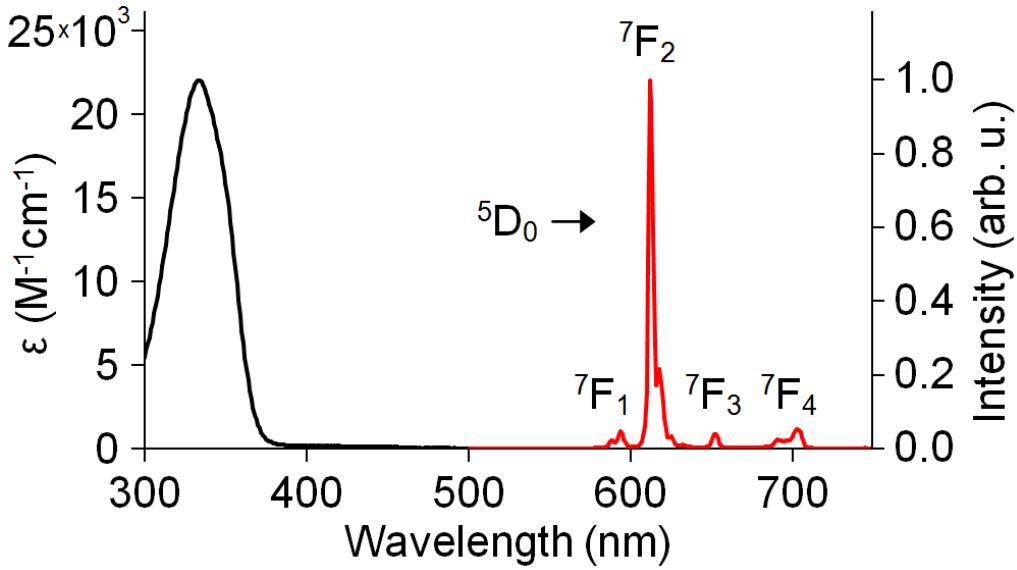

Figure 3.2. Photoabsorption spectrum (black) and photoluminescence spectrum (red) at 333 nm excitation, collected from a 2µM solution of $[Eu(L^1)_2]^-$ in 0.1 M TRIS buffer (pH = 7.4).

coordination number of $[Eu(L^2)_2]^-$ increases to nine (Fig. 3.6). The UV-visible absorption and photoluminescent emission properties of the three complexes are similar. In particular, all three show broadband absorption in the near UV, with the absorption maxima (λ_{max}) occurring at wavelengths near 340 nm and similar peak molar absorptivities (ε_{max}). Combined spectra of $[Eu(L^1)_2]^-$ in aqueous buffer are provided in Fig. 3.2 as a representative plot. A notable feature of the luminescence spectrum is the large $^5D_0 \rightarrow {}^7F_2$ transition, which accounts for 79% of the total emission.

Analysis of Eu^{III} luminescence is greatly simplified by the presence of a purely magnetic dipole transition ($^5D_0 \rightarrow {}^7F_1$). With an intensity that is unaffected by the ligand field, the $^5D_0$ to $^7F_1$ transition acts as an internal reference for estimating the radiative (k_{rad}) and nonradiative (k_{nonrad}) decay rates of the $^5D_0$ state. These quantities, together with the overall quantum yield Φ_{tot}, can then be used to determine the sensitization efficiency η_{sens}, the probability that the energy of an absorbed photon is successfully transferred onto the Eu^{III} center. This calculation is described in refs. [36, 44, 56] and in Section 1.4 of this dissertation. The overall quantum yields (Φ_{tot}) were experimentally determined by the optically dilute method using quinine sulfate as the fluorescence standard.

In aqueous solution, the lifetimes of each complex in H_2O and D_2O can be used to determine the degree of Eu^{III} hydration. Since O-H oscillators resonate at high energy, water is a particularly efficient quencher of Eu^{III} luminescence [18-20]. Consequently, each complex shows a shorter luminescent lifetime in water than deuterated water. The number of inner-sphere water molecules, q, is calculated using the empirically derived Horrocks equation [47],

$$q = 1.11(1/\tau_{H2O} - 1/\tau_{D2O} - 0.31), \quad (1)$$

where τ_{H2O} and τ_{D2O}, the observed luminescent lifetimes in the two solvents, are in ms. Comparing k_{nonrad} and q in Table 3.1 shows that water coordination leads to increased rates of nonradiative quenching.

Comparing the values η_{sens} and η_{Eu} in Table 3.1 reveals the rationale for choosing these three complexes to study. Complex $[Eu(L^1)_2]^-$ is approximately four times brighter than $[Eu(L^2)_2]^-$ and $[Eu(L^3)_2]^-$ due to efficient sensitization (large η_{sens}) and minimal quenching (large η_{Eu}; q close to zero; small k_{nonrad}). Complex $[Eu(L^2)_2]^-$ has efficient sensitization (large η_{sens}), but a low quantum yield due to quenching by a bound water molecule (small η_{Eu}; q close to one; large k_{nonrad}). Finally, $[Eu(L^3)_2]^-$ has minimal quenching (large η_{Eu}; q close to zero; small k_{nonrad}) but also a low quantum yield due to inefficient sensitization of the metal (low η_{sens}). Thus, complex $[Eu(L^1)_2]^-$ is representative of pathway (a) in Figure 3.1, $[Eu(L^2)_2]^-$ is representative of (b), and $[Eu(L^3)_2]^-$ is representative of (c). Synthesis and characterization of $[Eu(L^2)_2]^-$ and $[Eu(L^3)_2]^-$ have been reported previously (including further details on the photophysical measurements summarized in Table 3.1), while $[Eu(L^1)_2]^-$ will be reported soon [36, 55, 57].

Time-resolved Eu L_3-edge XANES measurements were performed in total fluorescence mode at beamline 11-ID-D of the Advanced Photon Source (APS) using a flowing jet of each sample in solution, at concentrations varying from 0.3 mM to 1 mM. The energy of the incident X-ray beam was scanned through the Eu L_3 edge (i.e., the $2p_{3/2}$ binding energy) in 0.25 eV steps, and the total X-ray fluorescence (proportional to the absorption for a dilute sample) was measured at each step. Avalanche photodiodes were used to record the time-resolved incident X-ray flux and the fluorescence from the sample. A pulsed 351 nm laser was used to excite the chromophore. Data were collected for 300 μs before and after each laser pulse. This collection time was limited by the height of the laser-illuminated volume of sample (approximately 750

μm) and the minimum jet flow rate needed to sustain laminar flow (approximately 3 m/s), rather than the luminescence lifetimes of the samples (τ_{obs} H2O, Table 3.1). Additional experimental details are given in the Supporting Information.

3.3 Results and Discussion

Typical L_3 XANES spectra for $[Eu(L^1)_2]^-$ are shown in Fig. 3.3a. The "white line" peak at 6987 eV corresponds to the $2p_{3/2} \rightarrow 5d$ excitations dominating the spectrum, since the 5d shell is unoccupied. The width of the peak is determined largely by the splitting of the 5d levels. There is an additional intrinsic broadening of the entire spectrum due to the lifetime of the $2p_{3/2}$ core hole; the implications of this effect are discussed below.

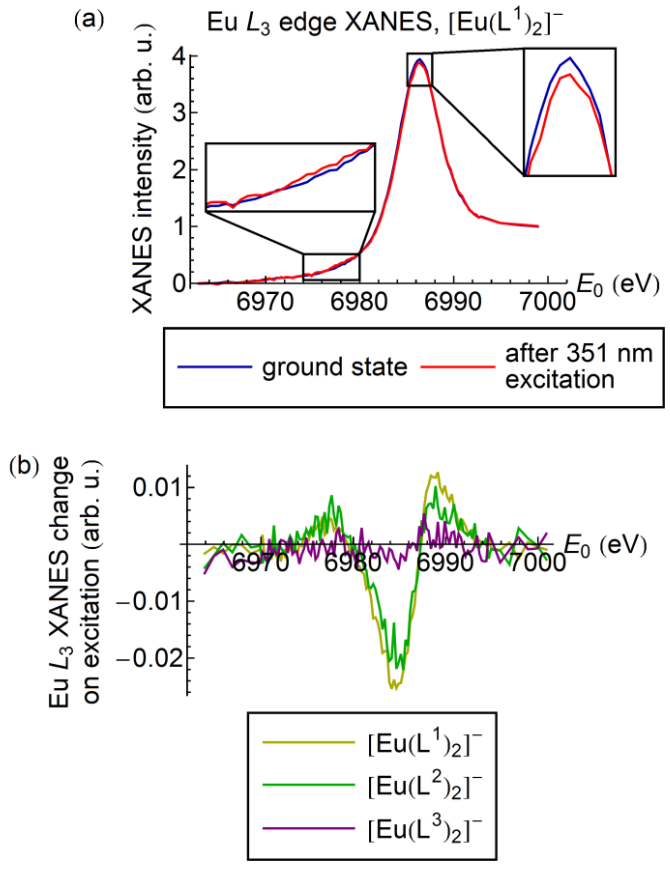

Figure 3.3 (a) Eu L_3 edge XANES collected from a 1 mM solution of $[Eu(L^1)_2]^-$. The sample was excited by a 351 nm laser with a fluence per pulse of approximately 20 mJ/cm^2. Two sections of the spectrum are magnified (insets) to show part of the change induced by the UV pump. (b) Fractional differences in the excited-state and ground-state XANES from the three complexes used in this study. To mitigate sample damage, the laser fluence was decreased to approximately 12 mJ/cm^2 while collecting these spectra, giving a smaller change than the one seen in (a). Data were averaged over 75 μs after the pump pulse to generate the excited-state spectra.

The UV photoexcitation caused a suppression of the white line and additional smaller changes, which are visible in the difference spectra shown in Fig. 3.3b. The difference scales with the pump laser power, saturating (but not changing functional form) near a fluence per shot of 20 mJ/cm^2; the spectra in Fig. 3.3a were collected at this fluence. The data shown in in Fig. 3.3b were collected at a fluence per shot of 12 mJ/cm^2.

The UV pump laser gradually caused sample damage, observed as precipitation of unidentified Eu-containing material out of each solution. Monitoring the intensity of the total fluorescence over time showed that during a typical ten-minute long XANES scan the concentration of Eu in solution decreased by approximately 0.05% (an amount we regard as negligible). The total white line intensity changed by approximately 1% following each laser pulse (Fig. 3.3b). In addition, we observed visible luminescence extending approximately 2 mm along the sample jet below the laser spot. Based on the jet flow rate (approximately 3 m/s), we estimate the luminescence lifetime to be on the order of 0.5 ms, consistent with optical measurements.

We first note that the signals from $[Eu(L^1)_2]^-$ and $[Eu(L^2)_2]^-$ have similar magnitudes and shapes, while the signal from $[Eu(L^3)_2]^-$ is strongly suppressed. We find this to be consistent with the calculated η_{sens} values discussed above; specifically, there is a clear correlation between the magnitude of the transient XANES signal and the efficiency of energy transfer from the ligand to the Eu^{III} ion. The long lifetime (> 100 μs) of the TR-XANES signal is also inconsistent with the short lifetimes of the ligand excited states of related systems at room temperature (< 10 ps) [46, 54]. We conclude that the transient signal is a feature of the Eu^{III} 4f-4f intrashell excitation that follows photoexcitation of the antenna, and that X-ray absorption spectroscopy is a useful probe of the transient 4f electronic state of the lanthanide atom in these systems.

Furthermore, we again emphasize that this method specifically targets the lanthanide, and it is therefore complementary to transient absorption and time-resolved photoemission measurements. As a possible application, we suggest that measurements at higher time resolution (available at XFEL facilities) should be able to determine the time delay between UV activation of the ligand and population of the lanthanide 4f excited state(s). This would directly probe the ligand-to-lanthanide energy transfer mechanism in complexes of this type [14-17, 45, 58].

Before concluding, it is interesting to consider possible mechanisms for the sensitivity of the L_3 XANES to the 4f intrashell configuration. Recall that this effect is unexpected in light of the insignificant structural differences between the ground state and the excited states of each complex (Fig. 3.7). We therefore consider mechanisms driven purely by changes in electronic structure.

Fig. 3.4a shows a simplified schematic of the density of states of Eu^{III} in the presence of a ligand. The ion has several narrow, atomic-like unoccupied 4f states near the Fermi level E_F, and a large unfilled 5d band. For clarity, we have plotted a small number of arbitrarily positioned 4f states rather attempting to show the entire 4f manifold. A simple broadening of the 5d band (Fig. 3.4b) would lead to suppression of the associated XANES peak. This might be caused, for example, by an increase in the crystal field splitting due to a change in the symmetry of the chelating cage around the Eu^{III} ion. However, no such distortion is expected here (Fig. 3.7). As an alternative explanation of our result, we first note that there is a TR-XANES peak at 6977 eV. We expect unoccupied 4f states (or mixed 4f-5d states) to contribute to the XANES near this energy, since FEFF calculations [59] (Fig. 3.12) show a concentration of Eu f states there. In addition, this energy is 10 eV below the white-line peak, and the gap between the 4f and 5d levels of Eu^{III} is on the order of 10 eV in solid-state systems [60-62].

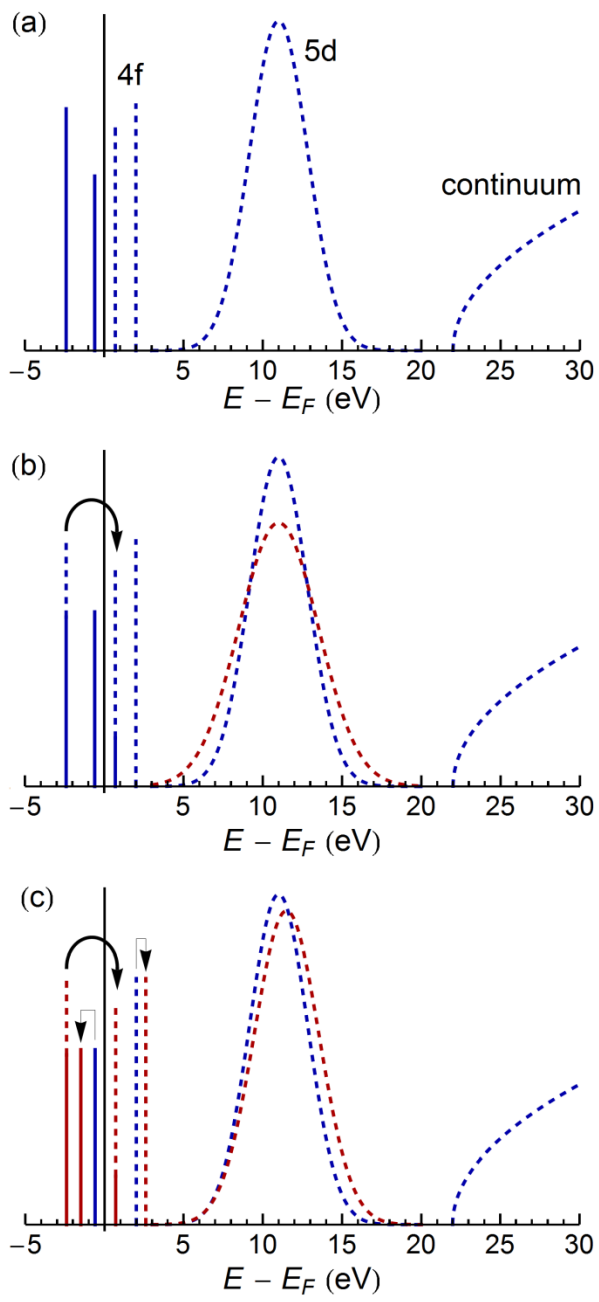

Figure 3.4. (a) Schematic representation of the density of states for ground-state Eu^{III}, including atomic-like occupied 4f states (solid lines), unoccupied 4f states (dashed), and unoccupied 5d and continuum bands. (b) Effect of a 4f-4f transition accompanied by a change in 5d crystal field splitting. (c) Effect of a 4f-4f excitation accompanied by a change in the degree of 4f-5d hybridization. The curved arrows indicate the change in electron occupancy upon excitation, while the orthogonal arrows indicate reorganization of the 4f manifold due to a changed 4f-5d hybridization.

Taken together, the TR-XANES features of the long-lived Eu^{III} excited state indicate a change in both the 4f and 5d states, as would be associated with an increase of 4f-5d mixing (Fig. 3.4c). As support for this hypothesis, we note that *static* orbital hybridization effects in lanthanide materials have been extensively studied [63-65]. In particular, quantitative

interpretations of visible lanthanide emission spectra [66-69] use 4f wavefunctions that are mixed with opposite-parity 5d states due to perturbation by the ligand field. The observation of a *time-dependent* change in the degree of orbital mixing would have important consequences for theoretical calculations of the energy transfer rate, as well as for treatments of the emission spectrum in these complexes.

The total fluorescence detection method used in this experiment gives spectra with an energy resolution intrinsically limited by the 3.91 eV lifetime of the $2p_{3/2}$ vacancy. The low resolution destroys some information about the density of states, especially changes of the hypothetical type shown in Fig. 3.4. The present data therefore do not distinguish unambiguously between the possible scenarios. Existing data on lanthanide compounds [70-73], including europium (III) oxide [62], show that it is possible to resolve 2p to 4f excitations with high detection energy resolution; further studies are ongoing.

3.4 Summary

We have identified a transient XANES signal associated with the 4f-4f intrashell transition that precedes hypersensitive emission in a family of luminescent Eu complexes. The functional form of the transient signal suggests that excitation-induced orbital hybridization effects may play an unexpected role in systems of the type studied here. More fundamentally, the existence of the signal demonstrates that time-resolved X-ray absorption spectroscopy is a promising tool for directly studying the excited states of lanthanides in luminescent materials.

3.5 Supporting Information

3.5.1 DFT Calculations

Ground state geometry optimization and frequency calculations were performed using Gaussian 09 at the Molecular Graphics and Computation Facility at University of California,

Berkeley, CA [74]. The B3LYP functional [75, 76] was used, treating the light atoms with the 6-31G(d,p) basis set [77-79] and the Eu^{III} atoms with the quasi relativistic effective core pseudopotential ECP52MWB (Gaussian Keyword MWB52) [80, 81]. All calculations were run with no symmetry constraints. Frequency calculations were inspected to ensure the absence of imaginary frequencies, confirming the structures minimized to a ground state. In all cases, input coordinates were originally taken from the appropriate crystal structures [36, 55]. Coordinates for the singlet-triplet structural comparison were superimposed in Accelrys Discovery Studio Viewer v3.5 using the metal and first coordination sphere as tether points. Molecular graphics were rendered in POV-RAY [82]. Ground state geometry minimizations of the XRD crystal structure coordinates are shown in Figure 3.5.

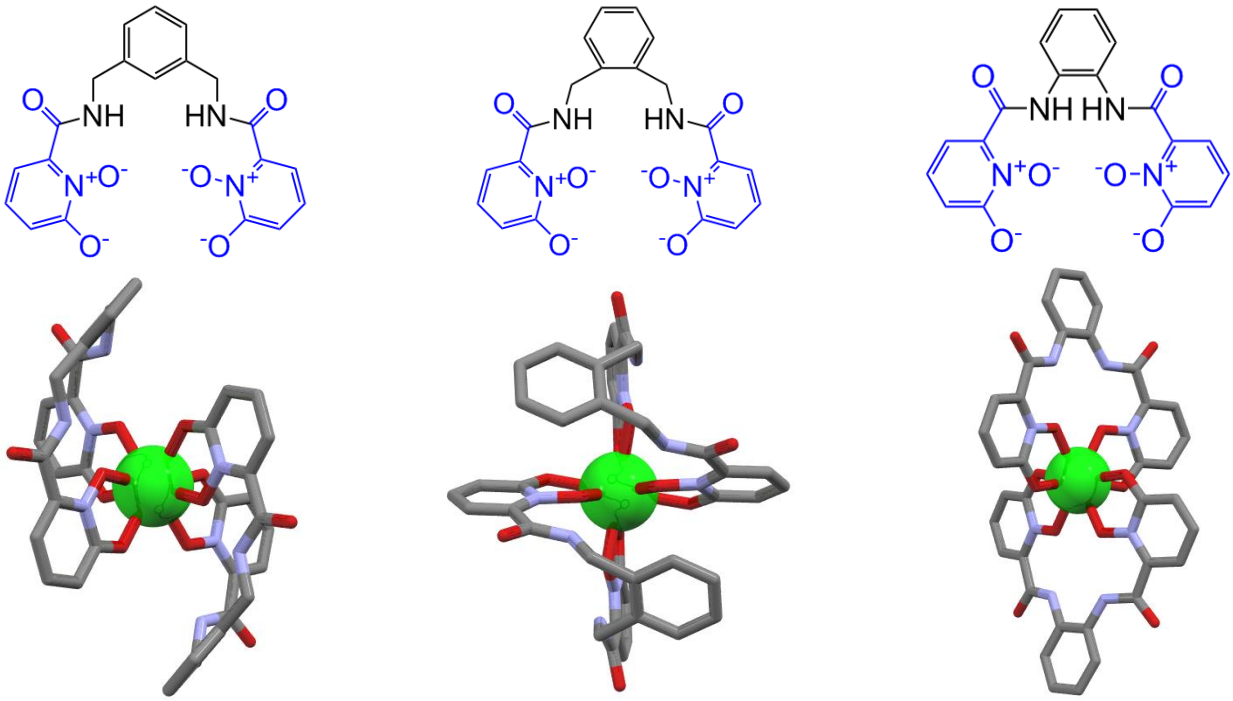

Figure 3.5. DFT geometry optimized structures of $[Eu(L^1)_2]^-$ (left), $[Eu(L^2)_2]^-$ (middle), and $[Eu(L^3)_2]^-$ (right).

The DFT minimizations of the XRD crystal structures are shown, viewed along the apparent C_2 symmetry axis that relates the two ligands. The shape of the eight coordinating oxygen atoms is closest to a D_{2d} trigonal face dodecahedron in all three cases. The 1,2-HOPO chelates span the *m* edges and the connecting backbones span either *g* edges (for $[Eu(L^1)_2]^-$ and $[Eu(L^2)_2]^-$) or *a* edges ($[Eu(L^3)_2]^-$). However, we know from the q-value of $[Eu(L^2)_2]^-$ (see Materials and Methods) that $[Eu(L^2)_2]^-$ is not 8-coordinate in aqueous solution. Addition of the 9th oxygen-containing ligand was modeled as a molecule of DMSO in these gas phase DFT calculations. DMSO was chosen instead of water for the purposes of calculation, since optimizations using water were skewed by the strong hydrogen bonding between the water protons and the anionic HOPO oxygens, an effect that is exacerbated by the lack of solvent treatments in these gas-phase calculations.

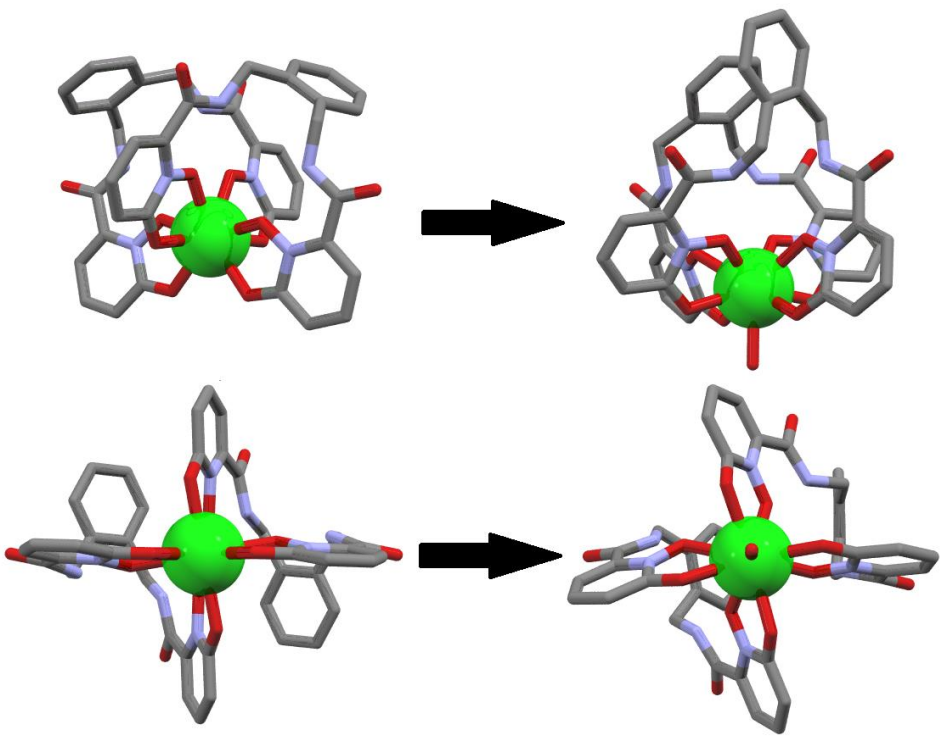

Figure 3.6. Two views of the DFT geometry optimized structures of $[Eu(L^2)_2]^-$ (left) and $[Eu(L^2)_2DMSO]^-$ (right), hydrogens and DMSO atoms (except coordinating oxygen) were removed for clarity.

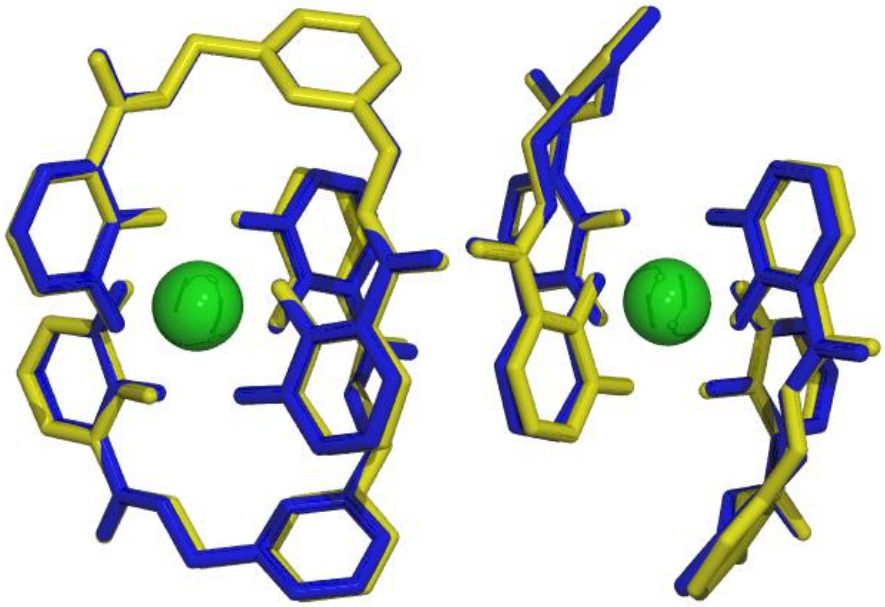

Figure 3.7. Two views of singlet (blue) and triplet (yellow) $[Eu(L^1)_2]^-$ superimposed to demonstrate similarity.

Superimposing the singlet and triplet state DFT minimized structures for $[Eu(L^1)_2]^-$ reveals that the structures are nearly identical. The average M-O bond distances were found to be 0.004 Å longer in the triplet state structure, which is an extremely small difference. Note that the triplet excited state calculated here is not the state that can be observed by our time resolved XANES signal. The ligand-centered singlet and triplet excited states are short lived in aqueous solution at room temperature, even more so in the presence of an accepting state on the Eu^{III}. The ligand is expected to quickly relax to the ground state structure once the energy has been transferred onto the Eu^{III} center. We therefore expect that the structures of the ground state and *4f* metal-centered excited state are even more closely matched than the two structures shown above.

3.5.2 Collection of Time-Resolved XANES

Laser pump/X-ray probe experiments were carried out at beamline 11-ID-D of the Advanced Photon Source (APS). The X-ray beam at this station has a flux of 5×10^{12} photons/second at the sample position, after focusing with a toroidal mirror to measure

approximately 2 mm (H) by 50 μm (V). The APS produced X-ray pulses approximately 80 ps wide at 153 ns intervals. The sample was excited with an Nd:YLF regenerative amplified laser (repetition rate 1.6 kHz, FWHM 5 ps); a frequency-tripling crystal was used to produce a 351 nm-wavelength beam. The laser spot, approximately 750 microns in diameter, was centered over the X-ray spot at the sample position. Neutral density filters were used to attenuate the laser, with the resulting fluence per shot incident on the sample varying between 1.6 and 40 mJ/cm^2.

We used a flowing jet of solution with diameter 0.5 mm. Assuming laminar flow, the linear speed of material in the jet can be estimated from the cross-sectional area and the volume flow rate. We found that (by adjusting the pump speed) the linear speed could be varied from 2.7 m/s to 3.5 m/s; the jet became visibly unstable outside this range. This means that after each laser pulse, the UV-illuminated volume of sample flowed past the X-ray beam within ~150 microseconds, which is less than the luminescence lifetime of all the samples studied here (see Table 3.1). We consequently found that the apparent decay rate of the TR-XANES signal

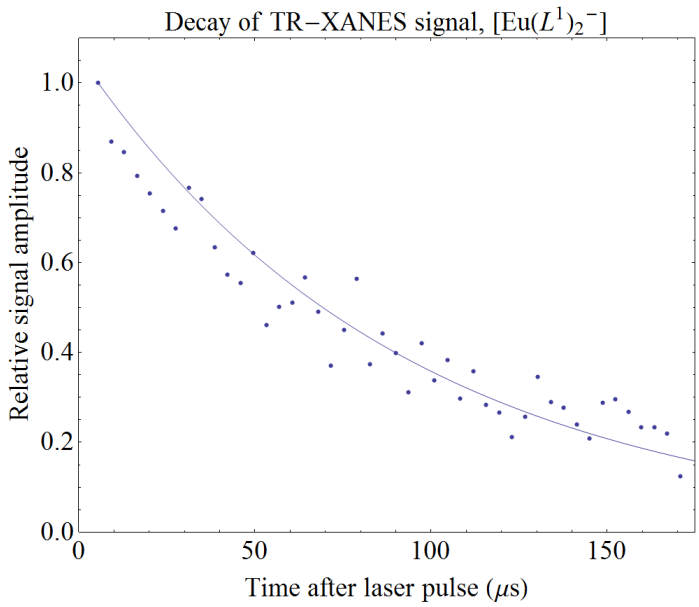

Figure 3.8. Time-dependence of the relative amplitude of the TR-XANES signal from complex $[Eu(L^1)_2]^-$, averaged over 3.6 μs intervals (points). The apparent lifetime is 92 μs (solid line).

depended on the flow speed. This constitutes a limitation on the measurement, as we cannot directly compare the decay rate of the TR-XANES signal with the known lifetime of the 4f intrashell excitation that we claim to observe. However, we note that there is no other excitation with a comparable lifetime (on the order of 100 μs) in the systems being studied here. Fig. 3.8 shows the apparent decay rate of the signal from complex $[Eu(L^1)_2]^-$ with the jet speed set to 3 m/s (this flow speed was used during collection of all the data presented here).

Sample concentrations ranged from 0.3 mM to 1 mM in pure water or aqeuous TRIS buffer (0.01 M, pH 7.4), with up to 15% DMSO by volume as a cosolvent. Solutions were prepared by dissolving each solid sample in DMSO and then diluting with either water or TRIS buffer. Spectral features were unaffected by these variations in solvent chemistry. We also compared solutions of complex $[Eu(L^1)_2]^-$ prepared from crystallizations with two counter-ions, py^+ and $NMe4^+$. The two transient XANES signals are shown in Fig. 3.9.

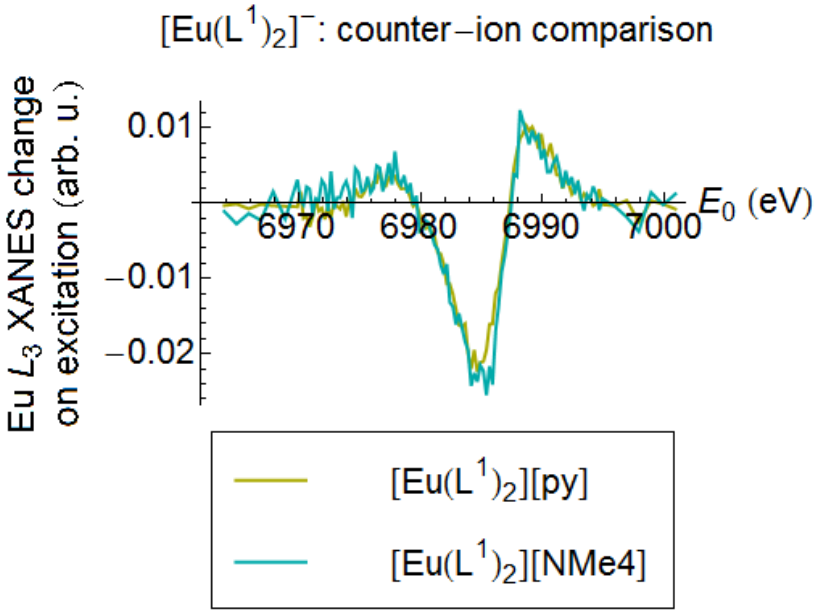

Figure 3.9. Transient XANES signals obtained from solutions of $[Eu(L^1)_2]^-$ with two counter-ions.

The data taken from the solution of [Eu(L^1)$_2$][NMe4] show higher noise, since a smaller quantity of sample was used. Otherwise, we observe no significant difference as a result of the change in counterion, especially when compared to the much larger variations among the three signals shown in Fig. 3.3. The similarities of the XANES signals are consistent with the fact that the luminescence behavior of the representative complex is unaffected by the counterion. For the sake of consistency, however, we have only used data collected from solutions of the pyridinium salts for making Fig. 3.3.

To clearly show the correlation between the observed XANES signal and the known efficiency for excitation of the Eu^{III} ion, the sensitization efficiency η_{sens} (see Table 3.1) is plotted against the integrated TR-XANES signals (Fig. 3b) of the three complexes (see Fig. 3.10 below).

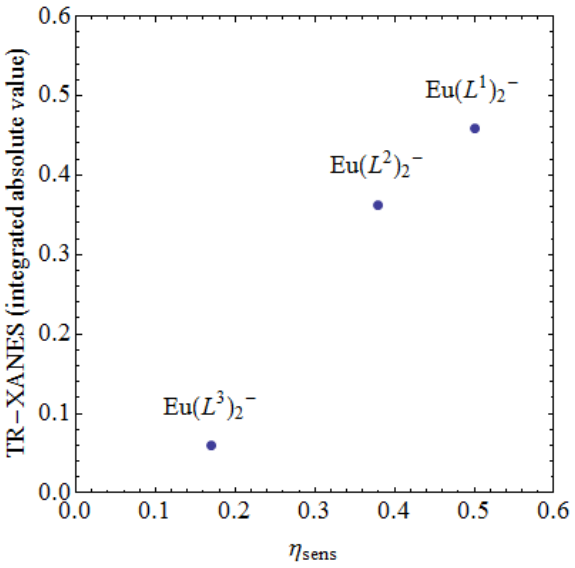

Figure 3.10. Correlation between η_{sens} and integrated TR-XANES signals.

3.5.3 Laser-Induced Damage

We used two criteria to assess sample damage: visual inspection of the sample solutions for precipitation and discoloration, and systematic drifts of the ground-state XANES. X-ray exposure caused no visible change in the samples, and correspondingly, we found no significant

change in the ground-state XANES over 1 hour of exposure to the X-rays alone (Fig. 3.11a). Exposure to the pump laser caused both precipitation of unidentified Eu-containing material out of solution and a gradual decrease in the ground-state XANES intensity (Fig. 3.11b). For comparison of this systematic drift with the transient signal, Fig. 3.11c shows the excited – ground state difference from a single scan, plotted against the difference in the ground state spectra from two consecutive scans (i.e., the systematic drift induced by 10 minutes of exposure to the pump laser). Note that the systematic drift is uniform across the scan range, and smaller in magnitude than the transient signal.

3.5.4 FEFF calculations

Using FEFF9 [83], we performed ab initio calculations of the *l*-projected density of states and multiple scattering calculations of the L_3 edge XANES for the Eu^{III} ion in the DFT-minimized structure of the ground state of complex $[Eu(L^1)_2]^-$. Self-consistent scattering potentials were calculated while including the effect of the *f* electrons (using the UNFREEZEF card). The results are shown in Figure 3.12. In the pre-edge region (below 6980 eV), the features of the *d*-DOS and *f*-DOS are closely aligned, a signature of the expected (static) 4*f*-5*d* hybridization common in lanthanide materials. The calculated XANES shown includes both electric dipole and electric quadrupole transitions (specified in the MULTIPOLE card). The contribution from quadrupole transitions alone, i.e. the expected position of $2p \rightarrow 4f$ transitions, is shown in the same panel. We note that both the large *f*-dos peak and the contribution to the XANES from quadrupole transitions have maxima in the same region as the TR-XANES signal at 6977 eV, providing evidence that the TR-XANES signal at this energy is associated with a change in either a mixed *f-d* state or a pure 4*f* state.

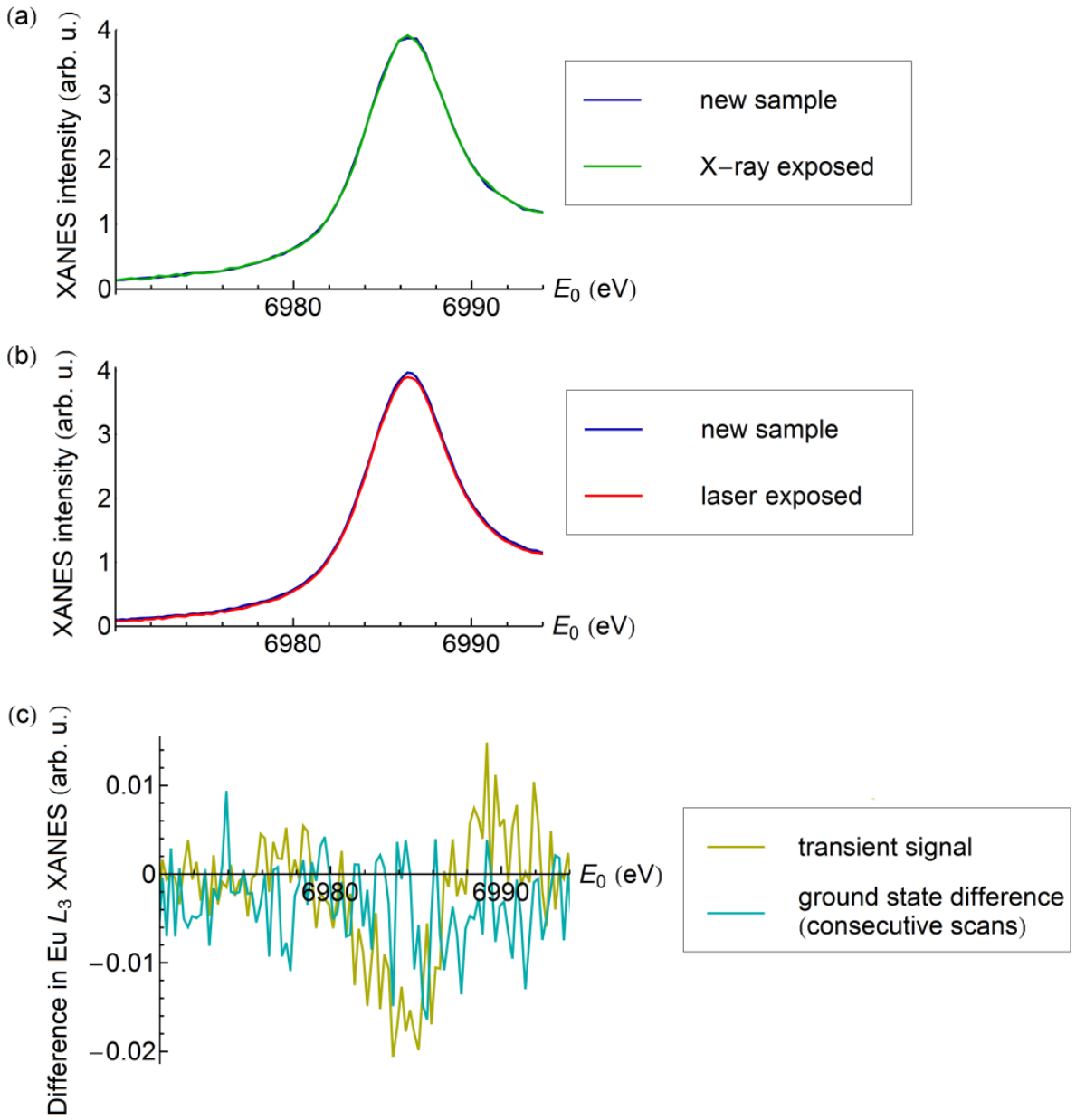

Figure 3.11. (a) Ground-state XANES collected from a newly prepared solution of $[Eu(L^1)_2]^-$ and from the same solution after 1 hour of exposure to the X-ray beam. Each scan required approximately 10 minutes of collection time. (b) Ground-state XANES collected from a second solution of $[Eu(L^1)_2]^-$ and from the same solution after 1 hour of simultaneous exposure to the X-ray beam and pump laser (12 mJ/cm^2 fluence per shot at 1.6 kHz). (c) Comparison of the transient signal with the systematic scan-to-scan drift.

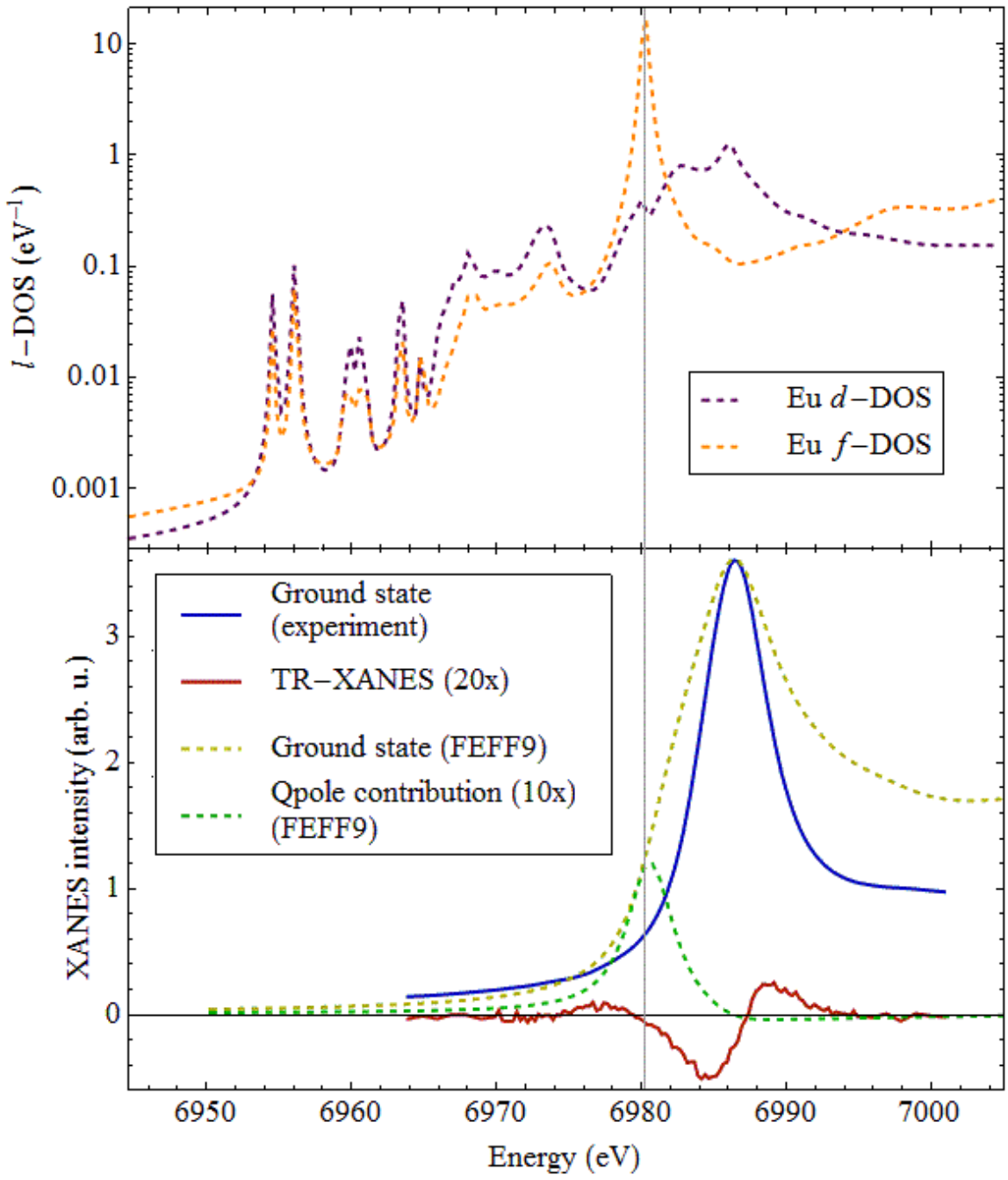

Figure 3.12. Upper panel: FEFF calculations of the *l*-projected density of states for the central Eu^{III} ion in $[Eu(L^1)_2]^-$. Lower panel: experimental ground state XANES and TR-XANES signal (solid lines; TR-XANES scaled vertically for clarity). Also shown are the FEFF-calculated XANES including both electric dipole and electric quadrupole transitions, and the contribution from quadrupole transitions alone (dashed lines; quadrupole contribution scaled vertically).

3.6 References

1. Pacold, J.I., et al., *Direct Observation of 4f Intrashell Excitation in Luminescent Eu Complexes by Time-Resolved X-ray Absorption Near Edge Spectroscopy.* Journal of the American Chemical Society, 2014. **136**(11): p. 4186-4191.
2. Eliseeva, S.V. and J.C.G. Bunzli, *Rare earths: jewels for functional materials of the future.* New Journal of Chemistry, 2011. **35**(6): p. 1165-1176.
3. Bunzli, J.C.G. and S.V. Eliseeva, *Lanthanide NIR luminescence for telecommunications, bioanalyses and solar energy conversion.* Journal of Rare Earths, 2010. **28**(6): p. 824-842.
4. Bunzli, J.C.G. and C. Piguet, *Taking advantage of luminescent lanthanide ions.* Chemical Society Reviews, 2005. **34**(12): p. 1048-1077.
5. Binnemans, K., *Lanthanide-Based Luminescent Hybrid Materials.* Chemical Reviews, 2009. **109**(9): p. 4283-4374.
6. de Sa, G.F., et al., *Spectroscopic properties and design of highly luminescent lanthanide coordination complexes.* Coordination Chemistry Reviews, 2000. **196**: p. 165-195.
7. Eliseeva, S.V.B., J. C. G., *Lanthanide luminescence for functional materials and bio-sciences.* Chemical Society Reviews, 2009. **39**: p. 189-227.
8. Weissman, S.I., *Intramolecular energy transfer - The fluorescence of complexes of europium.* Journal of Chemical Physics, 1942. **10**(4): p. 214-217.
9. Nakazawa, E., *Excitation energy transfer and cooperative optical phenomena*, in *Fundamentals of Phosphors*, W.M.S. Yen, S.; Yamamoto, H., Editor 2006, CRC Press. p. 89-100.
10. Bunzli, J.C.G.E., S. V., *Basics of Lanthanide Photophysics*, in *Lanthanide Luminescence*, H.P.H. H., Editor 2011, Springer Berlin Heidelberg. p. 1-45.
11. Forster, T., *10th Spiers Memorial Lecture - Transfer Mechanisms of Electronic Excitation.* Discussions of the Faraday Society, 1959(27): p. 7-17.
12. Forster, T., *Excitation Transfer and Internal-Conversion.* Chemical Physics Letters, 1971. **12**(2): p. 422-424.
13. Dexter, D.L., *A Theory of Sensitized Luminescence in Solids.* Journal of Chemical Physics, 1953. **21**(5): p. 836-850.
14. Lima, P.P., et al., *Energy transfer mechanisms in organic-inorganic hybrids incorporating europium(III): A quantitative assessment by light emission spectroscopy.* Journal of Physical Chemistry C, 2007. **111**(47): p. 17627-17634.
15. Ward, M.D., *Mechanisms of sensitization of lanthanide(III)-based luminescence in transition metal/lanthanide and anthracene/lanthanide dyads.* Coordination Chemistry Reviews, 2010. **254**(21-22): p. 2634-2642.
16. Hebbink, G.A., et al., *Singlet energy transfer as the main pathway in the sensitization of near-infrared Nd^{3+} luminescence by dansyl and lissamine dyes.* Chemphyschem, 2002. **3**(12): p. 1014-1018.
17. Hebbink, G.A., et al., *Unexpected sensitization efficiency of the near-infrared Nd^{3+}, Er^{3+}, and Yb^{3+} emission by fluorescein compared to eosin and erythrosin.* Journal of Physical Chemistry A, 2003. **107**(14): p. 2483-2491.
18. Heller, A., *Formation of Hot O-H Bonds in Radiationless Relaxations of Excited Rare Earth Ions in Aqueous Solutions.* Journal of the American Chemical Society, 1966. **88**(9): p. 2058.

19. Haas, Y. and G. Stein, *Pathways of Radiative and Radiationless Transitions in Europium(Iii) Solutions - Role of High Energy Vibrations.* Journal of Physical Chemistry, 1971. **75**(24): p. 3677.
20. Kropp, J.L. and M.W. Windsor, *Luminescence and Energy Transfer in Solutions of Rare-Earth Complexes. I. Enhancement of Fluorescence by Deuterium Substitution.* Journal of Chemical Physics, 1965. **42**(5): p. 1599.
21. Stickrath, A.B., et al., *Detailed Transient Heme Structures of Mb-CO in Solution after CO Dissociation: An X-ray Transient Absorption Spectroscopic Study.* Journal of Physical Chemistry B, 2013. **117**(16): p. 4705-4712.
22. Chen, L.X., et al., *Excited-state molecular structures captured by X-ray transient absorption spectroscopy: a decade and beyond.* Acta Crystallographica Section A, 2010. **66**: p. 240-251.
23. Bressler, C., et al., *Femtosecond XANES Study of the Light-Induced Spin Crossover Dynamics in an Iron(II) Complex.* Science, 2009. **323**(5913): p. 489-492.
24. Huse, N., et al., *Photo-Induced Spin-State Conversion in Solvated Transition Metal Complexes Probed via Time-Resolved Soft X-ray Spectroscopy.* Journal of the American Chemical Society, 2010. **132**(19): p. 6809-6816.
25. Monat, J.E. and J.K. McCusker, *Femtosecond excited-state dynamics of an iron(II) polypyridyl solar cell sensitizer model.* Journal of the American Chemical Society, 2000. **122**(17): p. 4092-4097.
26. Gawelda, W., et al., *Structural determination of a short-lived excited iron(II) complex by picosecond x-ray absorption spectroscopy.* Physical Review Letters, 2007. **98**(5): p. 057401.
27. Blasse, G. and B.C. Grabmeier, *Luminescent Materials.* 1994, Berlin: Springer-Verlag.
28. Fonger, W.H. and C.W. Struck, *Eu^{3+} ^5D Resonance Quenching to Charge-Transfer States in Y_2O_2S, La_2O_2S, and LaOCl.* Journal of Chemical Physics, 1970. **52**(12): p. 6364.
29. Struck, C.W. and W.H. Fonger, *Quantum-mechanical Treatment of Eu^{3+} 4f-4f and 4f-Reversible Charge-transfer- state Transitions in Y_2O_2S and La_2O_2S.* Journal of Chemical Physics, 1976. **64**(4): p. 1784-1790.
30. Soini, E. and T. Lovgren, *Time-Resolved Fluorescence of Lanthanide Probes and Applications in Biotechnology.* Crc Critical Reviews in Analytical Chemistry, 1987. **18**(2): p. 105-154.
31. Handl, H.L. and R.J. Gillies, *Lanthanide-based luminescent assays for ligand-receptor interactions.* Life Sciences, 2005. **77**(4): p. 361-371.
32. Petoud, S., et al., *Stable lanthanide luminescence agents highly emissive in aqueous solution: Multidentate 2-hydroxyisophthalamide complexes of Sm^{3+}, Eu^{3+}, Tb^{3+}, Dy^{3+}.* Journal of the American Chemical Society, 2003. **125**(44): p. 13324-13325.
33. Parker, D. and J.A.G. Williams, *Getting excited about lanthanide complexation chemistry.* Journal of the Chemical Society-Dalton Transactions, 1996(18): p. 3613-3628.
34. Moore, E.G., A.P.S. Samuel, and K.N. Raymond, *From Antenna to Assay: Lessons Learned in Lanthanide Luminescence.* Accounts of Chemical Research, 2009. **42**(4): p. 542-552.
35. Selvin, P.R., *Principles and biophysical applications of lanthanide-based probes.* Annual Review of Biophysics and Biomolecular Structure, 2002. **31**: p. 275-302.
36. D'Aleo, A., et al., *Aryl Bridged 1-Hydroxypyridin-2-one: Effect of the Bridge on the Eu(III) Sensitization 'Process.* Inorganic Chemistry, 2009. **48**(19): p. 9316-9324.

37. Moore, E.G., et al., *"Cymothoe sangaris": An extremely stable and highly luminescent 1,2-hydroxypyridinonate chelate of Eu(III).* Journal of the American Chemical Society, 2006. **128**(33): p. 10648-10649.
38. Moore, E.G., et al., *Highly luminescent lanthanide complexes of 1-hydroxy-2-pyridinones.* Inorganic Chemistry, 2008. **47**(8): p. 3105-3118.
39. Fernandez-Moreira, V., et al., *Bioconjugated lanthanide luminescent helicates as multilabels for lab-on-a-chip detection of cancer biomarkers.* Analyst, 2010. **135**(1): p. 42-52.
40. Moore, E.G., et al., *Eu(III) Complexes of Functionalized Octadentate 1-Hydroxypyridin-2-ones: Stability, Bioconjugation, and Luminescence Resonance Energy Transfer Studies.* Inorganic Chemistry, 2010. **49**(21): p. 9928-9939.
41. Crosby, G.A. and M. Kasha, *Intramolecular Energy Transfer in Ytterbium Organic Chelates.* Spectrochimica Acta, 1958. **10**(4): p. 377-382.
42. Moeller, T. and W.F. Ulrich, *Observations on the Rare Earths .67. Some Observations on the Absorption Spectra of Non-Aqueous Solutions of Some Acetylacetone Chelates.* Journal of Inorganic & Nuclear Chemistry, 1956. **2**(3): p. 164-175.
43. Sonesson, A., *On the Complex Chemistry of the Tervalent Rare Earth Ions .2. The Acetate Systems of Praseodymium, Samarium, Dysprosium, Holmium, Erbium and Ytterbium.* Acta Chemica Scandinavica, 1958. **12**(10): p. 1937-1954.
44. Werts, M.H.V., R.T.F. Jukes, and J.W. Verhoeven, *The emission spectrum and the radiative lifetime of Eu^{3+} in luminescent lanthanide complexes.* Physical Chemistry Chemical Physics, 2002. **4**(9): p. 1542-1548.
45. Yang, C., et al., *A highly luminescent europium complex showing visible-light-sensitized red emission: Direct observation of the singlet pathway.* Angewandte Chemie-International Edition, 2004. **43**(38): p. 5010-5013.
46. Moore, E.G., et al., *A comparison of sensitized Ln(III) emission using pyridine- and pyrazine-2,6-dicarboxylates - part II.* Dalton Transactions, 2013. **42**(6): p. 2075-2083.
47. Supkowski, R.M. and W.D. Horrocks, *On the determination of the number of water molecules, q, coordinated to europium(III) ions in solution from luminescence decay lifetimes.* Inorganica Chimica Acta, 2002. **340**: p. 44-48.
48. Malta, O.L., *Ligand-rare-earth ion energy transfer in coordination compounds. A theoretical approach.* Journal of Luminescence, 1997. **71**(3): p. 229-236.
49. Malta, O.L., *Mechanisms of non-radiative energy transfer involving lanthanide ions revisited.* Journal of Non-Crystalline Solids, 2008. **354**(42-44): p. 4770-4776.
50. Rodrigues, M.O., et al., *Theoretical and experimental studies of the photoluminescent properties of the coordination polymer $[Eu(DPA)(HDPA)(H_2O)_2]$ $4H_2O$.* Journal of Physical Chemistry B, 2008. **112**(14): p. 4204-4212.
51. Malta, O.L., et al., *Experimental and theoretical study of ligand field, 4f-4f intensities and emission quantum yield in the compound $Eu(bpyO_2)_4(ClO_4)_3$.* Journal of Alloys and Compounds, 2001. **323**: p. 654-660.
52. Malta, O.L., H.J. Batista, and L.D. Carlos, *Overlap polarizability of a chemical bond: a scale of covalency and application to lanthanide compounds.* Chemical Physics, 2002. **282**(1): p. 21-30.
53. Xiao, M. and P.R. Selvin, *Quantum yields of luminescent lanthanide chelates and far-red dyes measured by resonance energy transfer.* Journal of the American Chemical Society, 2001. **123**(29): p. 7067-7073.

54. Foley, T.J., et al., *Facile preparation and photophysics of near-infrared luminescent lanthanide(III) monoporphyrinate complexes.* Inorganic Chemistry, 2003. **42**(16): p. 5023-5032.
55. D'Aleo, A., et al., *Aryl-bridged 1-hydroxypyridin-2-one: Sensitizer ligands for Eu(III).* Inorganic Chemistry, 2008. **47**(14): p. 6109-6111.
56. Beeby, A., et al., *Intramolecular sensitisation of lanthanide(III) luminescence by acetophenone-containing ligands: the critical effect of para-substituents and solvent.* Journal of the Chemical Society-Dalton Transactions, 2002(1): p. 48-54.
57. Tatum, D., manuscript in preparation, 2014.
58. Rodriguez-Cortinas, R., et al., *Structural and photophysical properties of heterobimetallic 4f-Zn iminophenolate cryptates.* Inorganic Chemistry, 2002. **41**(21): p. 5336-5349.
59. Rehr, J.J., et al., *Parameter-free calculations of X-ray spectra with FEFF9.* Physical Chemistry Chemical Physics, 2010. **12**(21): p. 5503-5513.
60. Thiel, C.W. and R.L. Cone, *Investigating material trends and lattice relaxation effects for understanding electron transfer phenomena in rare-earth-doped optical materials.* Journal of Luminescence, 2011. **131**(3): p. 386-395.
61. Dorenbos, P., *The $4f_n$ <-> $4f_{n-1}5d$ transitions of the trivalent lanthanides in halogenides and chalcogenides.* Journal of Luminescence, 2000. **91**(1-2): p. 91-106.
62. Yamaoka, H., et al., *Resonant inelastic X-ray scattering of $EuNi_2(Si_{1-x}Ge_x)_2$ and Eu_2O_3 at Eu L_3 absorption edge.* Journal of the Physical Society of Japan, 2006. **75**(3): p. 034702.
63. Strange, P., et al., *Understanding the valency of rare earths from first-principles theory.* Nature, 1999. **399**(6738): p. 756-758.
64. Brown, S.D., et al., *Dipolar excitations at the L(III) x-ray absorption edges of the heavy rare-earth metals.* Physical Review Letters, 2007. **99**(24): p. 7401.
65. Brown, S.D., et al., *4f/5d hybridization in the heavy rare earth elements Er and Tm.* Physical Review B, 2013. **87**(16): p. 5111.
66. Judd, B.R., *Hypersensitive Transitions in Rare-Earth Ions.* Journal of Chemical Physics, 1966. **44**(2): p. 839.
67. Judd, B.R., *Ionic Transitions Hypersensitive to Environment.* Journal of Chemical Physics, 1979. **70**(11): p. 4830-4833.
68. Ofelt, G.S., *Intensities of Crystal Spectra of Rare-Earth Ions.* Journal of Chemical Physics, 1962. **37**(3): p. 511.
69. Mason, S.F., R.D. Peacock, and B. Stewart, *Ligand-Polarization Contributions to Intensity of Hypersensitive Trivalent Lanthanide Transitions.* Molecular Physics, 1975. **30**(6): p. 1829-1841.
70. Krisch, M.H., et al., *Evidence for a Quadrupolar Excitation Channel at the L_{III} Edge of Gadolinium by Resonant Inelastic X-Ray Scattering.* Physical Review Letters, 1995. **74**(24): p. 4931-4934.
71. Bartolome, F., et al., *Quadrupolar excitation channels at the L_3 edge of rare-earth ions probed by resonant inelastic x-ray scattering.* Physical Review B, 1999. **60**(19): p. 13497-13506.
72. Dallera, C., et al., *Resonant inelastic x-ray scattering at the L_2 and L_3 edge of terbium in $TbCo_2$ and TbF_3.* Physical Review B, 2000. **62**(11): p. 7093-7097.
73. Hamalainen, K., et al., *Elimination of the Inner-Shell Lifetime Broadening in X-Ray-Absorption Spectroscopy.* Physical Review Letters, 1991. **67**(20): p. 2850-2853.

74. Frisch, M.J., *Gaussian 09*, 2009, Gaussian, Inc.: Wallingford, CT.
75. Becke, A.D., *Density-Functional Thermochemistry .3. The Role of Exact Exchange.* Journal of Chemical Physics, 1993. **98**(7): p. 5648-5652.
76. Stephens, P.J., et al., *Ab-Initio Calculation of Vibrational Absorption and Circular-Dichroism Spectra Using Density-Functional Force-Fields.* Journal of Physical Chemistry, 1994. **98**(45): p. 11623-11627.
77. Ditchfield, R., W.J. Hehre, and J.A. Pople, *Self-Consistent Molecular-Orbital Methods .9. Extended Gaussian-Type Basis for Molecular-Orbital Studies of Organic Molecules.* Journal of Chemical Physics, 1971. **54**(2): p. 724.
78. Hehre, W.J., R. Ditchfield, and J.A. Pople, *Self-Consistent Molecular-Orbital Methods .12. Further Extensions of Gaussian-Type Basis Sets for Use in Molecular-Orbital Studies of Organic-Molecules.* Journal of Chemical Physics, 1972. **56**(5): p. 2257.
79. Gordon, M.S., *The Isomers of Silacyclopropane.* Chemical Physics Letters, 1980. **76**(1): p. 163-168.
80. Dolg, M., et al., *Energy-Adjusted Pseudopotentials for the Rare-Earth Elements.* Theoretica Chimica Acta, 1989. **75**(3): p. 173-194.
81. Dolg, M., H. Stoll, and H. Preuss, *A Combination of Quasi-Relativistic Pseudopotential and Ligand-Field Calculations for Lanthanoid Compounds.* Theoretica Chimica Acta, 1993. **85**(6): p. 441-450.
82. *Persistence of Vision Raytracer*, 2004, Persistence of Vision Pty. Ltd.
83. Rehr, J.J., et al., *Ab initio theory and calculations of X-ray spectra.* Comptes Rendus Physique, 2009. **10**(6): p. 548-559.

Chapter 4. Further time-resolved XANES signatures of 4f excited states in luminescent lanthanide materials

This text is derived from two manuscripts that are being prepared for submission: *Energy transfer and heavy-atom effects in Tb-organic complexes*, by Joseph I. Pacold,[†] David S. Tatum,[‡] Xiaoyi Zhang[‖], Gerald T. Seidler,[†] and Kenneth N. Raymond;[‡] and *Transient x-ray signature of a 4f excited state in a nanocrystalline Eu phosphor*, by Joseph I. Pacold,[†] Tetsuhiko Isobe,[§] Xiaoyi Zhang,[‖] and Gerald T. Seidler.[†]

[†]Department of Physics, University of Washington, Seattle, Washington 98195, United States
[‡]Chemical Sciences Division, Lawrence Berkeley National Laboratories, Berkeley, California 94720, United States, and Department of Chemistry, University of California, Berkeley, California 94720, United States
[‖]X-ray Science Division, Argonne National Laboratory, Argonne, Illinois 60439, United States
[§]Department of Applied Chemistry, Keio University, Kanagawa 223-8522, Japan

4.1 Introduction

This chapter summarizes two time-resolved XANES results on luminescent materials closely related to the samples reported on in Chapter 3. First, we studied a set of metallo-organic dyes in which Tb^{III} (instead of Eu^{III}) is the activator ion, and obtained a transient signal whose magnitude again is correlated with the quantum yield of the dye. Second, we studied a colloidal suspension of an inorganic Eu^{III}-activated phosphor, YVO_4:Bi,Eu. In both cases, we found transient XANES signals similar to those observed in the Eu-organic dyes. This validates the general approach of using TR-XANES to study excited state pathways in lanthanide materials. A limitation of these experiments is the lack of an independent measurement of the energy transfer efficiency for quantitative comparison with the TR-XANES signals. However, one can interpret the functional form of the signals as support for the 4f-5d mixing hypothesis proposed in Chapter 3. We discuss these results in light of another physical interpretation not considered in the

previous chapter, namely the possibility that the 4f excited state has ligand-to-metal charge transfer character.

4.2 Tb-organic dyes

Organic and metallo-organic fluorescent dyes are widely used in biomedical imaging and immunoassays [1-3]. We recall from Chapter 1 that lanthanide-organic dyes typically have lower quantum yields than purely organic molecules, but have the advantages of narrow emission lines and long excited state lifetimes. These properties make it possible to strongly suppress backgrounds (e.g. from other fluorescent species in the sample) by spectral filtering and time-gating. In the case of fluoroimmunoassays, which rely on energy transfer between two cooperating dyes, the long lifetimes of the lanthanide 4f states also increase the probability of successful energy transfer to the second dye [4-6]. The most commonly used immunoassay dyes are chelates of Eu^{III} and Tb^{III} [2, 3], which have strong emission lines at 618 nm and 547 nm. Since other visible and near-infrared emission wavelengths are sometimes desirable, dyes activated by other lanthanides have also been developed [1, 4] to take advantage of the range of 4f-4f emission wavelengths found across the lanthanide series.

Here, as an extension of our study of Eu^{III} chelates (Chapter 3) [7], we present results from a study of Tb^{III} chelates. The sample set again consists of three complexes with different quantum yields. However, the physical basis for the quantum yield variation is significantly different here. Rather than varying the bridge unit of the ligand (see Table 3.1), we vary substituent groups attached to the outer carbon atoms. This changes the energies and kinetics of the ligand excited states without significantly affecting coordination and bonding to the Tb^{III} ion. Recall that the emitting level of the lanthanide ion in these complexes is populated by energy transfer from a triplet excited state of the organic ligand (see Fig. 3.1). Consequently, there is a

straightforward resonance condition affecting ligand-to-lanthanide energy transfer (ET): the ET efficiency is higher when the ligand triplet state energy is a close match to the energy of the accepting lanthanide state. (See the discussion of energy transfer mechanisms in Section 1.5.) Two of the dyes studied here have sensitizing ligands with different triplet state energies, and therefore have different quantum yields. The third has an unexpectedly low quantum yield given its triplet state energy, due to a quenching mechanism that is not yet positively identified.

4.2.1 Materials and methods

The structure of the base ligand in all the complexes used in this study is shown in Fig. 4.1. Synthesis and characterization procedures are reported in ref. [8]. In solution, two ligands bind to each Tb^{III}, producing a complex in which eight oxygen atoms are coordinated to the central Tb^{III} ion. External groups on the chelating cage, labeled X in Fig. 4.1, may be substituted to tune the absorption band and excited state energies of the ligand. Absorption and emission spectra typical of this family of complexes are shown in Fig. 4.2.

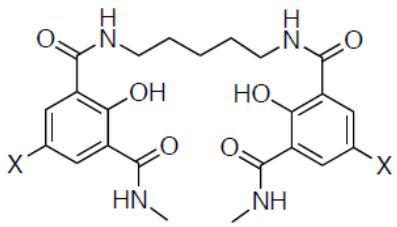

Figure 4.1. From ref. [9], chemical structure of the 5LI-IAM-X ligand (X = PEG, SO_3, Br).

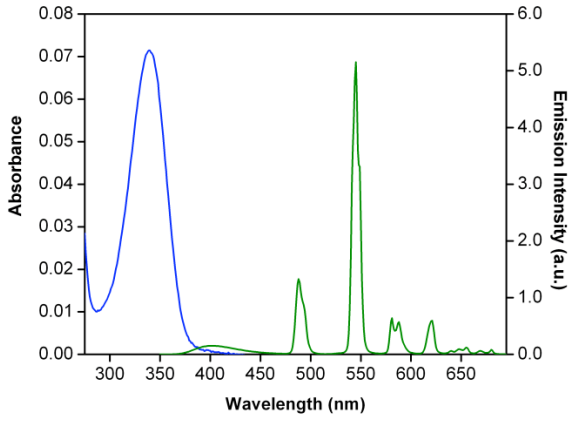

Figure 4.2. From ref. [8], absorbance (blue) and emission (green; λ_{exc} = 240 nm) of the Tb(5LI-IAM-SO_3)$_2$ complex in 0.1 M TRIS buffer, pH = 7.4.

The differences in quantum yield that result from varying the substituent X are summarized in Table 4.1. For this study, complexes of Tb^{III} with ligands with X = PEG, SO_3, and Br substituents were synthesized. Note that, in general, the quantum yield is optimized with the triplet state energy is ~2750 cm^{-1} above the energy of the Tb^{III} emitting state. This energy difference prevents back-transfer of the excitation from the lanthanide to the ligand [10]. Moving off the resonance to either higher or lower energy decreases the quantum yield. A notable exception to the pattern is the Br-substituted ligand, which has much lower quantum yield than the similar Cl-substituted ligand, in spite of their nearly identical triplet state energies. This is hypothesized [9] to be due to heavy-atom quenching by the Br. Quenching effects due to the high spin-orbit coupling constants of heavy atoms have been observed in several organic molecules [11]; the addition or substitution of high-Z atoms tends to increase the rate of nominally spin-forbidden transitions between states of the ligand, thus increasing both the rate of singlet-to-triplet conversion and the rate of energy loss via triplet-to-ground state transitions.

Ligand X =	**$T_{0\text{-}0}$ (cm^{-1})**	**Φ**
Amide	24000	0.40
SO_3	23900	0.38
H	23300	0.36
PEG	23170	0.56
Br	22300	0.06
Cl	22100	0.30
CH_3	22100	0.29
F	21600	0.10
NO_2	21400	0
OCH_3	19900	0

Table 4.1. Energies of the triplet excited state ($T_{0\text{-}0}$) and quantum yields (Φ) obtained from Tb^{III} complexes of ligands with several substituent groups. For comparison with the triplet state energies, the energy of the emitting Tb^{III} $^5D_4$ state is 20400 cm^{-1}. The three ligands used in this study are highlighted.

For the present ligands, measurements of the phosphorescence from the triplet state [9] showed that the triplet state lifetime of the Br-substituted ligand is 1.61 ms, compared to 3.03 ms for the Cl-substituted ligand. This suggests that increased losses from the triplet state lead to the lower quantum yield of the Br ligand. It should be noted, however, that the presence of the heavy atom is also expected to increase the ET rate from the ligand triplet state to the emitting Tb^{III} $^5D_4$ state. In addition, the Tb^{III} luminescence lifetime in the Br-ligand complex is 0.94 ms, compared to 1.98 ms in the Cl-ligand complex, suggesting that another quenching mechanism is involved (most likely back-transfer from the Tb^{III} to the ligand). There is no analog for Tb^{III} of the branching ratio calculation used to deduce the ET efficiency in the Eu^{III} complexes, and it is therefore not possible to distinguish between the possible quenching mechanisms with UV/visible spectroscopy.

We performed a time-resolved XANES study of the complexes with PEG, SO_3, and Br substituents. The samples were prepared as 1 mM (PEG- and SO_3-substituted ligands) and 0.3 mM (Br-substituted ligand) solutions in 0.01 M aqueous TRIS buffer (pH = 7.4) with up to 5% DMSO as a co-solvent. Laser-pump/x-ray probe measurements were performed on a flowing jet of each solution at beamline 11-ID-D of the Advanced Photon Source. The samples were excited with 351 nm pulses produced by a frequency-doubled Nd:YLF regenerative amplified laser. We collected Tb L_3-edge XANES averaged over 180 μs before and 75 μs after each laser pulse.

4.2.2 Results and discussion

Ground state and transient XANES spectra are shown in Fig. 4.3. As with the Eu complexes, the L_3-edge spectrum is dominated by a "white line" peak due to $2p_{3/2} \rightarrow 5d$ transitions. Photoexcitation leads to a transient change in the white line; for the ligands with PEG and SO_3 substituents, the ration between the magnitudes of the transient signals corresponds well

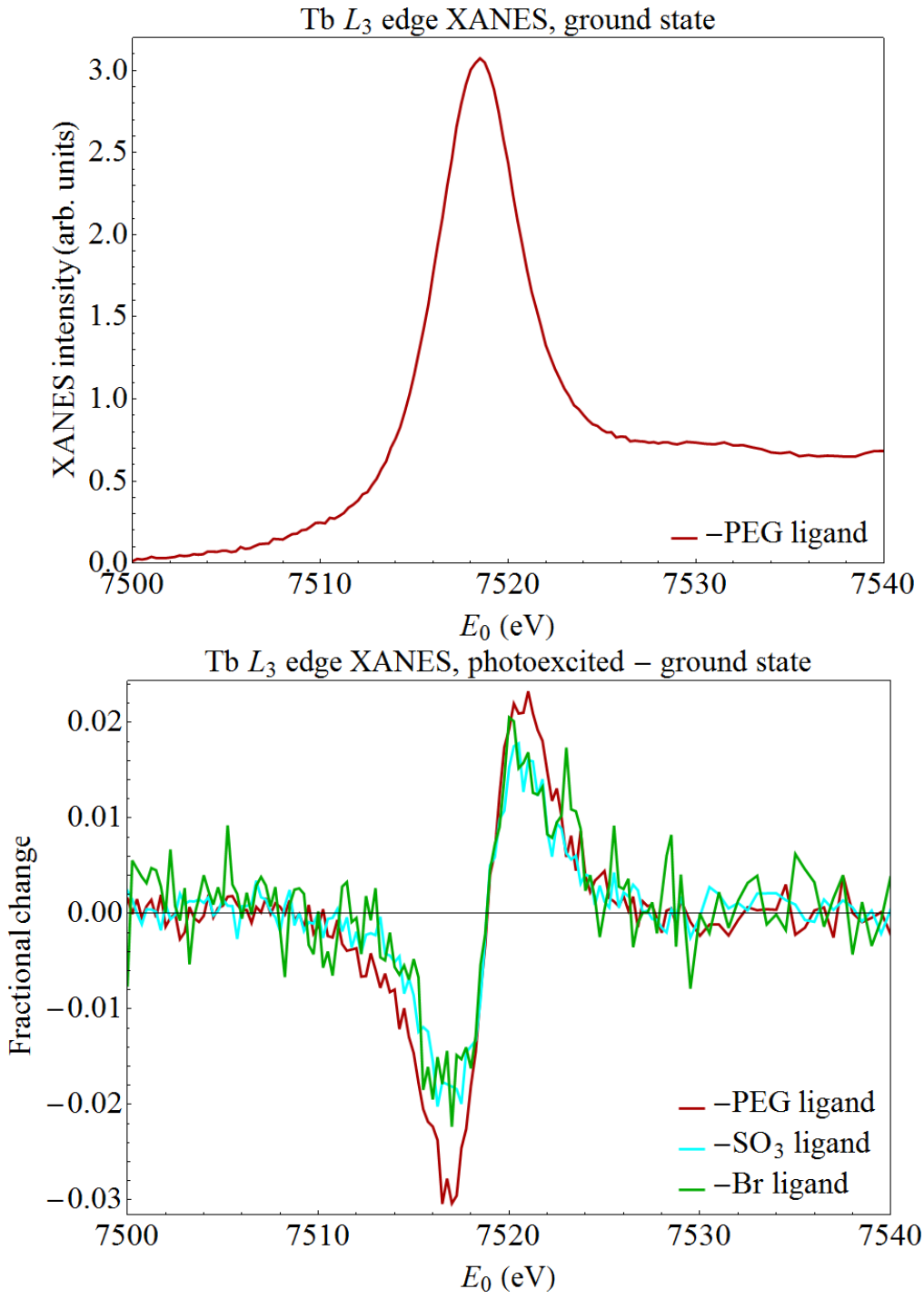

Figure 4.3. Ground state Tb L_3-edge XANES of Tb(5LI-IAM-PEG)$_2$ and transient XANES signals from Tb complexes with three substituent groups.

with the ratio of quantum yields. The low-quantum-yield Br-substituted ligand, on the other hand, produces a transient signal that is statistically indistinguishable from that of the SO_3-substituted ligand. This suggests that population of the Tb^{III} $^5D_4$ state is in fact of roughly equal efficiency in the Br- and SO_3-substituted ligands, and that thermal back-transfer is the primary reason for the lower quantum yield of the Br-ligand complex.

There is no low-energy feature in the transient signal corresponding to the shoulder seen 10 eV below the white line in the Eu data (see Fig. 3.3). One possible explanation for that the $2p_{3/2} \rightarrow 4f$ contribution to the XANES, which is already weak due to its electric dipole-forbidden nature, is further suppressed due to the higher 4f occupancy of Tb^{III} relative to Eu^{III}. The transient signal can be modeled well by a simple shift of the white line to lower energy. Under the hypothesis presented in Chapter 3 that the 4f excited state is accompanied by a transient change in 4f-5d mixing, we can interpret this as a reorganization of the 5d orbitals as they mix with lower-energy 4f states.

4.3 Nanocrystalline YVO_4:Bi,Eu

To investigate whether the TR-XANES approach is applicable to inorganic materials, we performed a study of a colloidal suspension of a nanocrystalline phosphor, YVO_4:Bi,Eu. Thin film coatings of YVO_4:Eu and YVO_4:Bi,Eu are promising candidates for conversion of solar UV radiation into visible, in order to improve the useful lifetime of organic and dye-sensitized solar cells [12, 13]. This application will be discussed in more detail in Section 5.1.

The band structures of YVO_4 and YVO_4:Bi were investigated by Dolgos et al. [14]; as the precise sequence of excited states following photoexcitation is important for interpretation of the TR-XANES results, we briefly summarize the results here. In the isolated VO_4^{3-} ion, there is a 4.5 eV gap between the nonbonding O 2p HOMO and the LUMO, which is a linear combination

of antibonding V 3d and O 2p orbitals. The lowest-energy excitation can therefore be thought of as an O-V charge transfer. Bulk YVO_4 has valence and conduction bands derived from the VO_4^{3-} HOMO and LUMO, respectively, with a 3.8 eV band gap. Upon doping with Bi^{3+} (which substitutes for the Y^{3+} ion) there is a shift of the absorption band to longer wavelengths. This arises from the fact that Y^{3+} has a noble gas electron configuration, while Bi^{3+} has a partially filled 6p shell. In particular, the Bi 6p orbitals hybridize with the VO_4^{3-} antibonding orbitals, reducing the band gap to 2.8 eV.

Therefore, the UV absorption band of YVO_4:Bi can be thought of as an O-V charge transfer excitation with some O-Bi charge transfer character. The key point here is that the excitation is confined to the luminescence sensitizers (i.e., the host lattice and the Bi^{3+} dopant), with no participation of the Eu^{3+} activator if it is present. This is in contrast to phosphors that are excited by charge transfer from the lanthanide activator to the host lattice [15-19]. Choosing this particular sample therefore ensures that the TR-XANES signal will be derived purely from the 4f intrashell excited state of the Eu ion, rather than from the more drastic changes electronic structure that accompany a charge transfer state.

4.3.1 Materials and methods

An aqueous suspension of YVO_4:7%Bi,7%Eu (particle size ~30 nm) was prepared according to a wet chemical synthesis procedure reported in refs. [20, 21]. For transport to the beamline, the suspension was reduced to a paste (~40% water by mass) using a rotary evaporator. The photoluminescence spectrum of the paste is shown in Fig. 4.4. We also collected Eu L_3 edge EXAFS (Fig. 5.5) to verify that the Eu^{3+} ion substitutes for the Y^{3+} site; EXAFS data were collected at beamline 20-ID-B of the Advanced Photon Source.

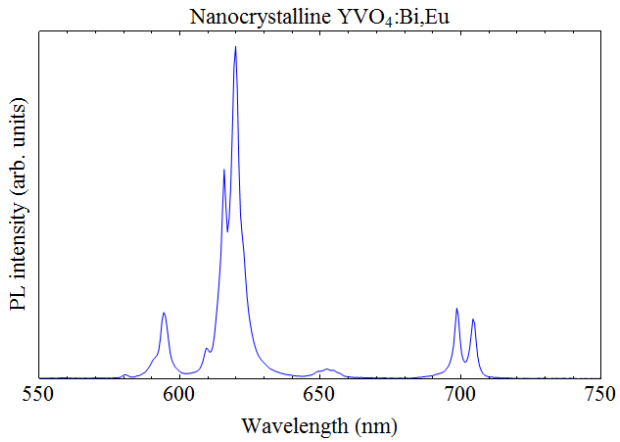

Figure 4.4. Photoluminescence spectrum of a concentrated colloidal paste of nanocrystalline YVO_4:Bi,Eu (λ_{exc} = 350 nm).

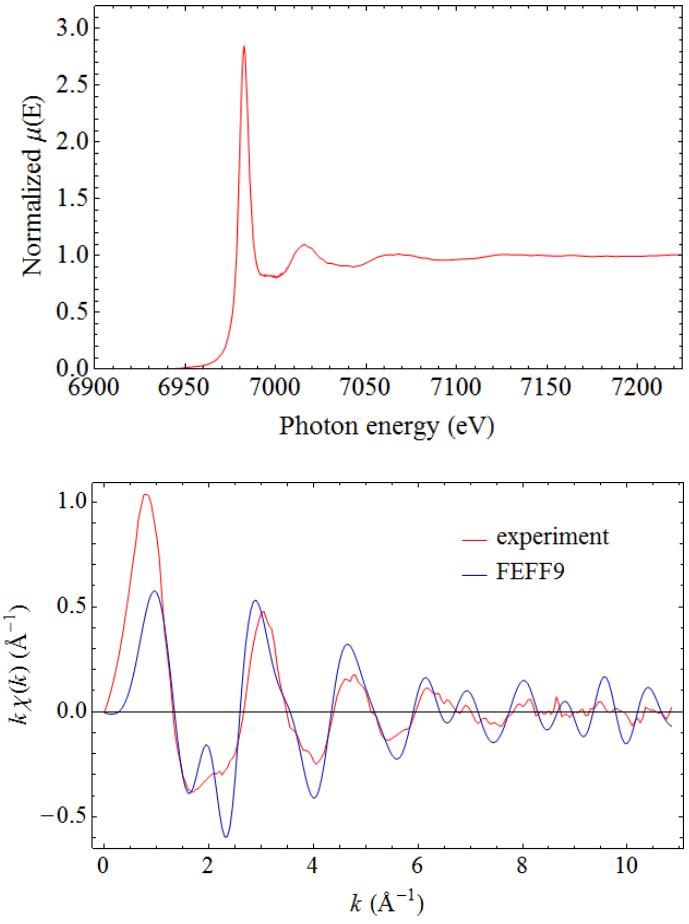

Figure 4.5. Eu L_3-edge EXAFS collected from the nanocrystalline YVO_4:Bi,Eu paste. The *k*-space data are shown with results from FEFF9 [22] for an Eu atom placed at the Y site.

Immediately before TR-XANES data collection, the paste was re-diluted with water to a concentration of approximately 2 mM in the Eu dopant, and sonicated for 30 minutes to produce a colloidal dispersion. Laser-pump/x-ray probe measurements at the Eu L_3 edge were performed on a flowing jet of the suspension at beamline 11-ID-D of the Advanced Photon Source, using 351 nm pump pulses as in the Tb study reported above.

4.3.2 Results and discussion

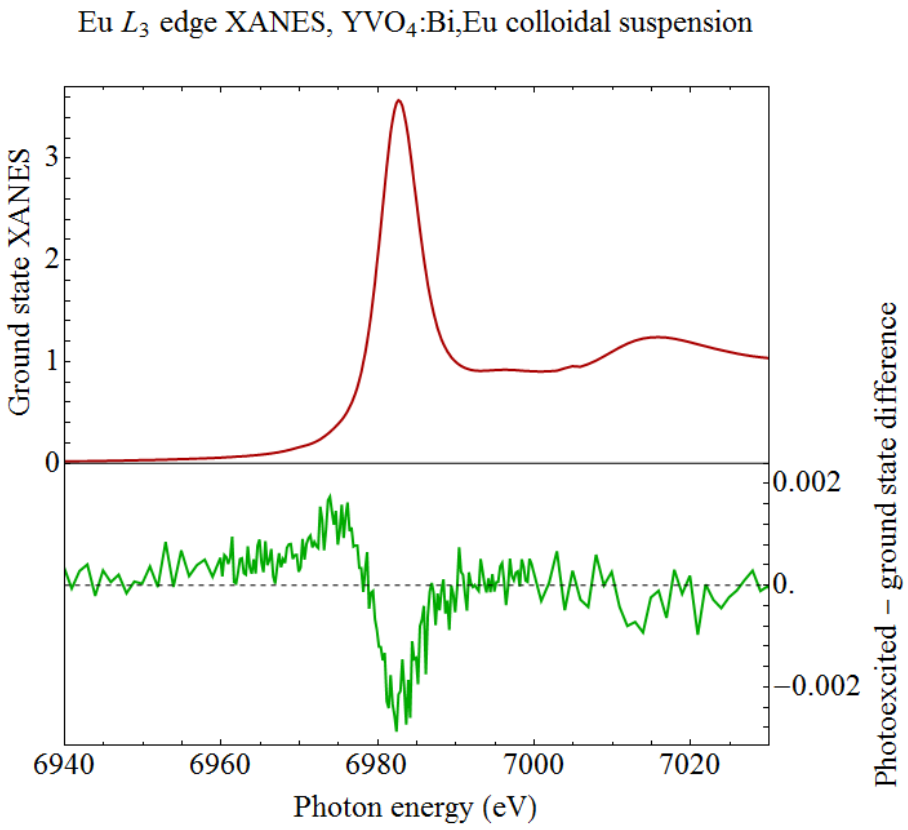

Figure 4.6. Ground-state XANES and difference spectra collected from an aqueous suspension (~ 5 mM Eu) of nanocrystalline YVO_4:Bi,Eu.

TR-XANES results are shown in Fig. 4.6. As in the study of Eu-organic dyes reported in Chapter 3, we observe an excited – ground state difference signal that consists of a suppression of the Eu white line together with an increase in absorption near 6977 eV, i.e., at the expected

energy of 2p → 4f transitions. As discussed in Section 3.3, we hypothesize that this pre-edge feature in particular can be attributed to transient reorganization of the 4f shell. Here, in light of this result, as well as the Tb XANES dataset, we discuss another hypothesis that was not covered in Chapter 3: the possibility that the transient state we are observing has metal-to-ligand charge transfer (MLCT) character. MLCT excitations are part of the excited state cascade in several inorganic Eu-activated phosphors [16, 23] and transition metal-organic complexes [24, 25]. The transfer of a 4f electron to the ligand (or to the host lattice in the case of the YVO_4:Bi,Eu) would cause an increase in absorption due to 2p → 4f transitions,

The divalent lanthanides typically have L edge energies approximately 10 eV below the corresponding edges of the trivalent lanthanides. As an example, Figure 4.7 shows Sm L_3-edge XANES collected from Sm in three compounds with divalent ($SmCl_2$), trivalent (SmF_3), and mixed (Sm_2S_4) Sm valence. This raises the question of whether a feature 10 eV below the edge, as observed in Figs. 3.3 and 4.6, could be a signature of a state with divalent character, i.e. a mixed state with a small contribution from a charge transfer state. As mentioned in Section 4.3.1, intermediate Ln-to-lattice charge transfer states are known to play a role in the sensitization of many inorganic phosphors [15-19]. Metal-to-ligand charge transfer states have also been observed in closely related photoactive transition metal-organic complexes [26-28], where the orbital reorganization that accompanies the charge transfer state leads to changes of typically 0.2 Å in the metal-ligand bond lengths (see Section 2.3.2).

Similar charge transfer excitations and structural distortions have not been reported, however, in either the Ln-organic dyes studied here or in YVO_4:Bi,Eu (which is instead reported to be sensitized via a charge transfer confined to the Bi/vanadate host [29]). This is reflected in the DFT calculations presented in Chapter 3, as well as in the relatively small fractional TR-

XANES signals that we observe; compare the scales in Figs. 4.3 and 4.6 with, for example, the charge transfer-associated TR-XANES signal shown in Fig. 2.7. The lack of a transient feature 10 eV below the edge in the Tb results is also evidence that charge transfer states are not significant in the sequence of excited states in the Tb dyes. In summary, while metal-to-ligand charge transfer is an important possibility to consider in light of existing results on related systems, we conclude that it is unlikely to contribute significantly in the systems studied here.

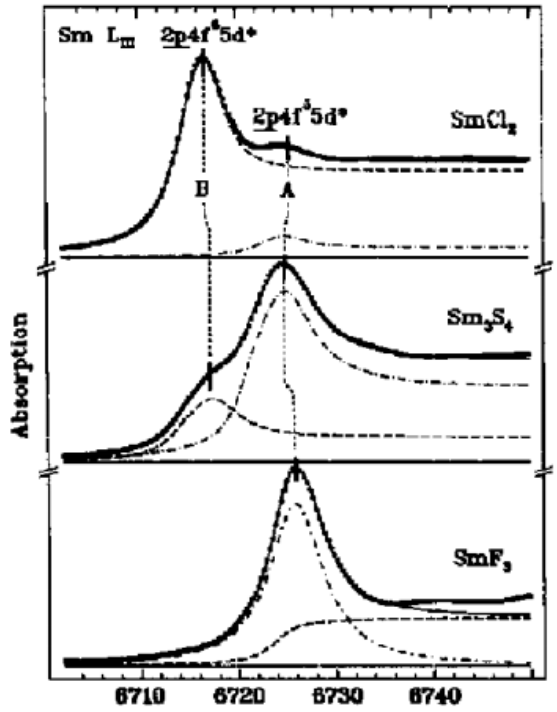

Figure 4.7 Sm L_3-edge XANES of several compounds with different Sm valences [30].

4.4 Conclusion

We applied the methodology of the TR-XANES study reported in Chapter 3 to several other luminescent lanthanide systems, specifically a set of Tb-organic dyes and an inorganic Eu-activated phosphor. In the case of the Tb-organic dyes, we found an interesting discrepancy between the overall quantum yield and our TR-XANES-derived measurement of the efficiency

with which a heavy atom-containing ligand sensitizes the Tb activator. This suggests that thermal back-transfer, rather than inefficient energy transfer from the ligand to the Tb ion, is the primary reason for the unexpectedly low quantum yield of this complex. For the inorganic phosphor, we obtain a TR-XANES result similar to our results on Eu-organic dyes; in particular, we observe a similar feature at the energy associated with 2p → 4f transitions. These results provide additional validation of our general approach to studying 4f intrashell excitations by x-ray spectroscopy.

4.5 References

1. Moore, E.G., A.P.S. Samuel, and K.N. Raymond, *From Antenna to Assay: Lessons Learned in Lanthanide Luminescence.* Accounts of Chemical Research, 2009. **42**(4): p. 542-552.
2. Alpha, B., J.M. Lehn, and G. Mathis, *Energy-Transfer Luminescence of Europium(Iii) and Terbium(Iii) Cryptates of Macrobicyclic Polypyridine Ligands.* Angewandte Chemie-International Edition in English, 1987. **26**(3): p. 266-267.
3. Cross, J.P., A. Dadabhoy, and P.G. Sammes, *The sensitivity of the lehn cryptand-europium and terbium (III) complexes to anions compared to a coordinatively saturated systems.* Journal of Luminescence, 2004. **110**(3): p. 113-124.
4. Werts, M.H.V., et al., *A near-infrared luminescent label based on Yb-III ions and its application in a fluoroimmunoassay.* Angewandte Chemie-International Edition, 2000. **39**(24): p. 4542.
5. Soini, E. and I. Hemmila, *Fluoroimmunoassay - Present Status and Key Problems.* Clinical Chemistry, 1979. **25**(3): p. 353-361.
6. Soini, E. and T. Lovgren, *Time-Resolved Fluorescence of Lanthanide Probes and Applications in Biotechnology.* Crc Critical Reviews in Analytical Chemistry, 1987. **18**(2): p. 105-154.
7. Pacold, J.I., et al., *Direct Observation of 4f Intrashell Excitation in Luminescent Eu Complexes by Time-Resolved X-ray Absorption Near Edge Spectroscopy.* Journal of the American Chemical Society, 2014. **136**(11): p. 4186-4191.
8. Samuel, A.P.S., et al., *Water-soluble 2-hydroxyisophthalamides for sensitization of lanthanide luminescence.* Inorganic Chemistry, 2008. **47**(17): p. 7535-7544.
9. Samuel, A.P.S., *Optimizing New Classes of Luminescent Lanthanide Complexes*, in *Chemistry*2003, University of California, Berkeley: Berkeley, CA.
10. Latva, M., et al., *Correlation between the lowest triplet state energy level of the ligand and lanthanide(III) luminescence quantum yield.* Journal of Luminescence, 1997. **75**(2): p. 149-169.
11. Martinho, J.M.G., *Heavy-Atom Quenching of Monomer and Excimer Pyrene Fluorescence.* Journal of Physical Chemistry, 1989. **93**(18): p. 6687-6692.
12. Riwotzki, K. and M. Haase, *Colloidal YVO_4:Eu and $YP_{0.95}V_{0.05}O_4$:Eu nanoparticles: Luminescence and energy transfer processes.* Journal of Physical Chemistry B, 2001. **105**(51): p. 12709-12713.

13. Riwotzki, K., et al., *Liquid-phase synthesis of colloids and redispersible powders of strongly luminescing $LaPO_4$:Ce,Tb nanocrystals.* Angewandte Chemie-International Edition, 2001. **40**(3): p. 573-576.
14. Dolgos, M.R., et al., *The electronic structures of vanadate salts: Cation substitution as a tool for band gap manipulation.* Journal of Solid State Chemistry, 2009. **182**(7): p. 1964-1971.
15. Fonger, W.H. and C.W. Struck, *Eu^{3+} ^5D Resonance Quenching to Charge-Transfer States in Y_2O_2S, La_2O_2S, and LaOCl.* Journal of Chemical Physics, 1970. **52**(12): p. 6364.
16. Struck, C.W. and W.H. Fonger, *Dissociation of $Eu3^+$ Charge-Transfer State in Y_2O_2S and La_2O_2S into Eu^{2+} and a Free Hole.* Physical Review B, 1971. **4**(1): p. 22-&.
17. Struck, C.W. and W.H. Fonger, *Quantum-mechanical Treatment of Eu^{3+} 4f-4f and 4f-Reversible Charge-transfer- state Transitions in Y_2O_2S and La_2O_2S.* Journal of Chemical Physics, 1976. **64**(4): p. 1784-1790.
18. Blasse, G., *The influence of charge-transfer and rydberg states on the luminescence properties of lanthanides and actinides.* Structure and Bonding, 1976. **26**: p. 43-79.
19. Peacock, R.D., *Charge-Transfer Contribution to Intensity of Hypersensitive Trivalent Lanthanide Transitions.* Molecular Physics, 1977. **33**(5): p. 1239-1246.
20. Takeshita, S., T. Isobe, and S. Niikura, *Low-temperature wet chemical synthesis and photoluminescence properties of YVO_4:Bi^{3+},Eu^{3+} nanophosphors.* Journal of Luminescence, 2008. **128**(9): p. 1515-1522.
21. Takeshita, S., et al., *Effects of the homogeneous Bi^{3+} doping process on photoluminescence properties of YVO_4:Bi^{3+},Eu^{3+} nanophosphor.* Journal of Luminescence, 2009. **129**(9): p. 1067-1072.
22. Rehr, J.J., et al., *Parameter-free calculations of X-ray spectra with FEFF9.* Physical Chemistry Chemical Physics, 2010. **12**(21): p. 5503-5513.
23. Hunt, R.B. and R.G. Pappalardo, *Fast Excited-State Relaxation of Eu-Eu Pairs in Commercial Y_2O_3-Eu^{3+} Phosphors.* Journal of Luminescence, 1985. **34**(3): p. 133-146.
24. Huse, N., et al., *Photo-Induced Spin-State Conversion in Solvated Transition Metal Complexes Probed via Time-Resolved Soft X-ray Spectroscopy.* Journal of the American Chemical Society, 2010. **132**(19): p. 6809-6816.
25. Van Kuiken, B.E., et al., *Probing the Electronic Structure of a Photoexcited Solar Cell Dye with Transient X-ray Absorption Spectroscopy.* Journal of Physical Chemistry Letters, 2012. **3**(12): p. 1695-1700.
26. Khalil, M., et al., *Picosecond X-ray absorption spectroscopy of a photoinduced iron(II) spin crossover reaction in solution.* Journal of Physical Chemistry A, 2006. **110**(1): p. 38-44.
27. Bressler, C. and M. Chergui, *Ultrafast X-ray absorption spectroscopy.* Chemical Reviews, 2004. **104**(4): p. 1781-1812.
28. Gawelda, W., et al., *Structural determination of a short-lived excited iron(II) complex by picosecond x-ray absorption spectroscopy.* Physical Review Letters, 2007. **98**(5): p. 057401.
29. Huang, X.Y., et al., *Spectral conversion for solar cell efficiency enhancement using YVO_4:Bi^{3+},Ln^{3+} (Ln = Dy, Er, Ho, Eu, Sm, and Yb) phosphors.* Journal of Applied Physics, 2011. **109**(11).

30. Hu, Z.W., G. Kaindl, and G. Meyer, *X-ray absorption near-edge structure at the L(I-III) thresholds of Pr, Nd, Sm, and Dy compounds with unusual valences.* Journal of Alloys and Compounds, 1997. **246**(1-2): p. 186-192.

Chapter 5. Saturation of x-ray excited luminescence in Eu-activated phosphors by cross-relaxation

This chapter is a manuscript in preparation by Joseph I. Pacold[1], Devon R. Mortensen[1], William Reichlin[2], Y. Zou Finfrock[3], Anthony Diaz[2], and Gerald T. Seidler.[1]
[1]Department of Physics, University of Washington, Seattle, Washington 98195, United States
[2]Chemistry Department, Central Washington University, Ellensburg, WA 98926, United States
[3]Advanced Photon Source, Argonne National Laboratory, Argonne, IL 60439, United States

Abstract

This chapter reports the first study of saturation effects in the x-ray excited optical luminescence (XEOL) of doped and co-doped YVO_4:Eu and YVO_4:Bi,Eu phosphors. We observe a decrease in the Eu XEOL yield at high x-ray flux density that we analyze in a kinetic model in which pairs of excited Eu ions undergo an Auger-like cross-relaxation. This effect is well documented in the literature on cathode-ray phosphors, and is a function of the fraction of Eu ions that reach the excited state necessary for emission. Furthermore, we observe that introduction of the Bi co-dopant has a statistically negligible influence on the quenching effect. We estimate that 4% of the Eu ions in each sample are excited at the highest flux density reached in this study (10^{12} photons/second in a 5 μm-wide spot). We consider a possible extension of this work to higher x-ray densities, and discuss its relevance for future x-ray spectroscopy studies that require high flux, e.g. time-resolved x-ray emission spectroscopy.

5.1 Introduction: vanadate- and Bi-activated phosphors

Compounds, molecules, and nanoparticles containing lanthanides as primary constituents or as dopants are seeing a dramatic growth in scientific and technical importance. In the field of optical materials, and especially luminescent or fluorescent materials in the near-infrared and optical, this includes continued improvements in classic fields such as luminescent time-resolved immuno-assays [1-3], phosphors for lighting [4, 5], telecommunications [6-8], and laser materials [6, 9, 10].

An interesting emerging application is solar spectrum conversion for the enhancement of photovoltaic cell performance. [11-15] For reference, we have reproduced the solar spectrum in Fig. 5.1. In the context of Si-based photovoltaics, there are two approaches to enhancing photovoltaic efficiency subject to the realities of the solar spectrum. First, partial utilization of

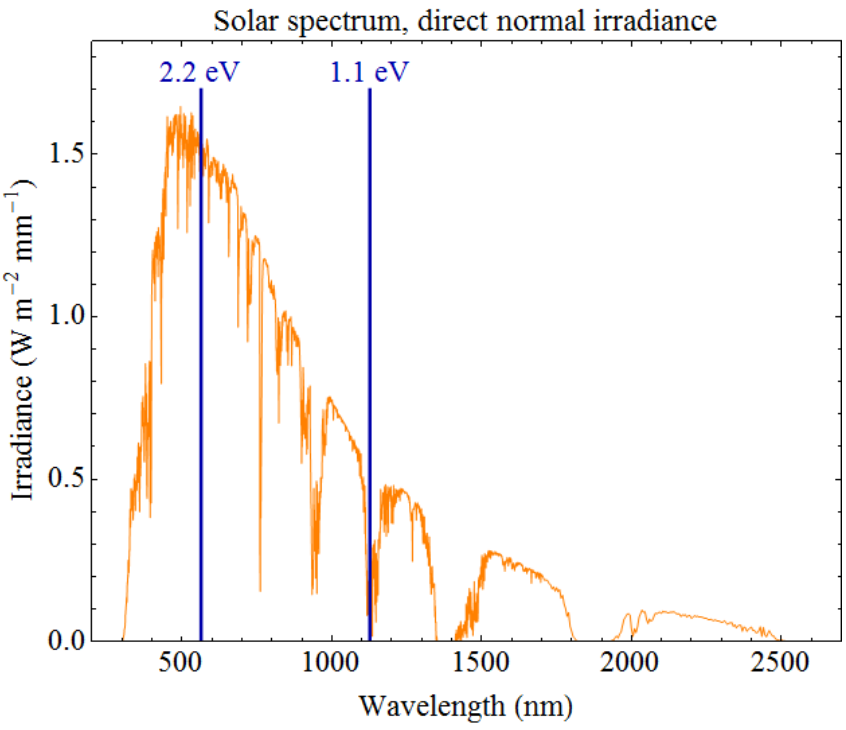

Figure 5.1. Solar spectrum at the surface of the Earth under standardized atmospheric conditions [16]. The band gap of Si (1.1 eV) and twice the band gap are indicated to highlight the long- and short-wavelength portions of the spectrum, which can be up-converted and down-converted respectively to improve the performance of an Si PV cell.

the long-wavelength, below band gap portion of the solar spectrum can come from "up-converting" multiple IR photons to single photons above the 1.1 eV bandgap. This increases the quantum efficiency of the cell by creating electron-hole pairs with photons that would otherwise not occur at all. Second, improved power output from the short-wavelength tail of solar spectrum can occur upon by "down-converting" (or "quantum cutting") single UV photons having energies above 2.2 eV into multiple photons with energies just above 1.1 eV. Down-conversion mitigates wasting of the excess energy of UV photons compared to the Si bandgap by creating more than one electron-hole pair per photon [13, 14].

On the other hand, in the context of organic and dye-sensitized solar cells, the more limited goal is to develop a coating that is transparent to visible light but that strongly absorbs UV photons and converts them to visible or near-IR with high efficiency. Such a coating would drastically reduce UV degradation of the organic and organometallic components of the cell, improving its useful lifetime without sacrificing performance [12].

Hence, for both "quantum cutting" and UV-to-visible converting phosphors, it is important to be able to engineer the absorption band to cover the UV portion of the solar spectrum, i.e., wavelengths between approximately 300 nm and 400 nm. The commercially available phosphors developed for fluorescent lighting do not satisfy this criterion, as they were designed for use with the 254 nm emission of Hg [17]. To overcome this limitation, it is possible to manipulate the near-UV absorption by adding a dopant. In particular, doping of several commonly used lighting phosphors with Bi has been shown to insert localized levels into the band gap due to Bi-lattice charge transfer excitations [18, 19], thus yielding an interesting strategy for improving phosphor performance for possible enhancement of photovoltaic harvesting of the solar spectrum.

Here, we report a study of x-ray excited optical luminescence (XEOL) in YVO_4:10%Eu, YVO_4:10%Bi, and YVO_4:10%Bi,10%Eu using a synchrotron x-ray microprobe endstation capable of achieving sufficiently high flux densities that nonlinear XEOL effects due to saturation of steps in the energy relaxation cascade can be observed. To our knowledge this is the first such study using x-rays (rather than cathode rays) to excite the samples. YVO_4:Eu was initially investigated as a red phosphor for cathode-ray tubes [20]; more recently, YVO_4:Eu and YVO_4:Bi,Eu have been proposed as wavelength-converting coatings for dye-sensitized solar cells [12, 21-24]. Schematics of the excited state cascades are shown in Fig. 5.2a. In both materials, we observe saturation of specific Eu emission lines at high excitation density. The saturation behavior is described well by a model based on cross-relaxation, i.e., an Auger-like process involving two interacting Eu ions (Fig. 5.2b). Identical saturation behavior is observed in Eu-doped samples with and without the Bi codopant.

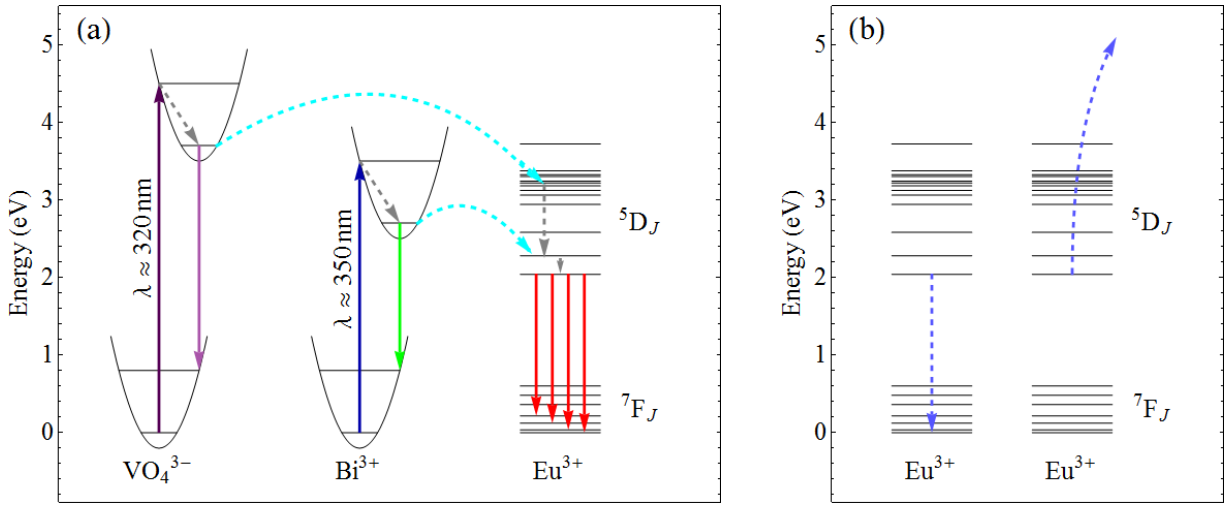

Figure 5.2. (a) Schematic of the excited states involved in luminescence in YVO_4:Bi,Eu, adapted from ref. [22]. Solid arrows represent radiative transitions and dashed arrows represent nonradiative transitions. **(b)** Two nearby Eu^{3+} ions that are both in the long-lived $^5D_0$ state may decay by cross-relaxation instead of emitting photons. In this process, one of the two ions returns to a lower-energy state while the second is excited to a higher-energy state.

We continue as follows. In Section 5.2, we briefly review existing applications of XEOL. Section 5.3 describes the synthesis of the phosphor samples, their characterization by optical and x-ray methods, and the procedure for the XEOL saturation measurement. In Section 5.4, we present the results for YVO_4:10%Eu, YVO_4:10%Bi, and YVO_4:10%Bi,10%Eu; consider possible saturation mechanisms; and demonstrate that the data are consistent with cross-relaxation being the dominant quenching effect. In Section 5.5, we summarize and conclude, discuss the limitations of the XEOL approach, and outline the necessary additional steps needed to obtain detailed information on the energy transfer cascade.

5.2 Applications of XEOL

An X ray absorbed by a solid can produce a high-energy photoelectron, which in turn will produce an avalanche of secondary electron-hole pairs by scattering from other electrons. In luminescent materials, the secondary excited electrons may transfer energy to activator sites, leading to emission of visible light. This effect is clearly useful for x-ray detection and imaging [25-27]. XEOL has also bee used extensively for detection of lanthanides and actinides at the part-per-billion level [28-31]; this application takes advantage of the non-specificity of the technique. By "non-specificity" we mean that (1) the secondary electrons have a broad distribution of energies and (2) in principle, they can deposit the energy that they carry on any site in the sample, without restrictions due to the selection rules for radiative transitions. This constitutes a limitation of XEOL, in the sense that methods such as photoluminescence can distinguish between different excitation channels, and therefore provide more detailed information on the process of luminescence.

XEOL has been used as a detection mode in x-ray absorption fine structure (XAFS) studies of luminescent materials [32-34]. Here, again, the nonspecific nature of the excitation is

often an obstacle: the edge step in XEOL-mode XAFS is often weak or undetectable, as crossing an absorption edge of the targeted element does not necessarily lead to a measureable increase in the intensity of the emission lines [35]. However, collecting the optical emission from the sample (rather than the x-ray emission) can make it possible to collect XAFS datasets that distinguish between sites with different luminescence properties. For example, XEOL-mode XAFS was used to determine the local structure of luminescent centers in porous Si [36].

Here, we examine a saturation effect in the XEOL yield that occurs when luminescent materials are placed in a microfocused hard x-ray beam with a flux of over 10^{12} photons/second. From an experimental point of view, this is valuable information for laser pump/x-ray probe studies of energy transfer processes in lanthanide phosphors. Such measurements will require high x-ray flux densities to achieve practical count rates, and the nonspecific excitations induced by the probe pulse must therefore be evaluated.

5.3 Materials and Methods

Powders of YVO_4:x%Bi,y%Eu (x, y = 0, 3, 10) were synthesized by solid-state reactions. To prepare each sample, stoichiometric amounts of Y_2O_3, Bi_2O_3, Eu_2O_3, and NH_4VO_3 were combined in an agate mortar with a small amount of hexane and ground for 20 minutes. Once dried, the resulting powder was transferred to an alumina crucible and fired at 1100 °C for 6 hours. The material was removed from the furnace, allowed to cool and ground into powder. The powder was then re-fired at 1100 °C for an additional 3 hours, allowed to cool, and re-ground. X-ray powder diffraction patterns were collected from each sample with a diffractometer (Philips XPert MPD, Cu Kα radiation) and were found to be consistent with the tetragonal YVO_4 structure (Fig. 5.3).

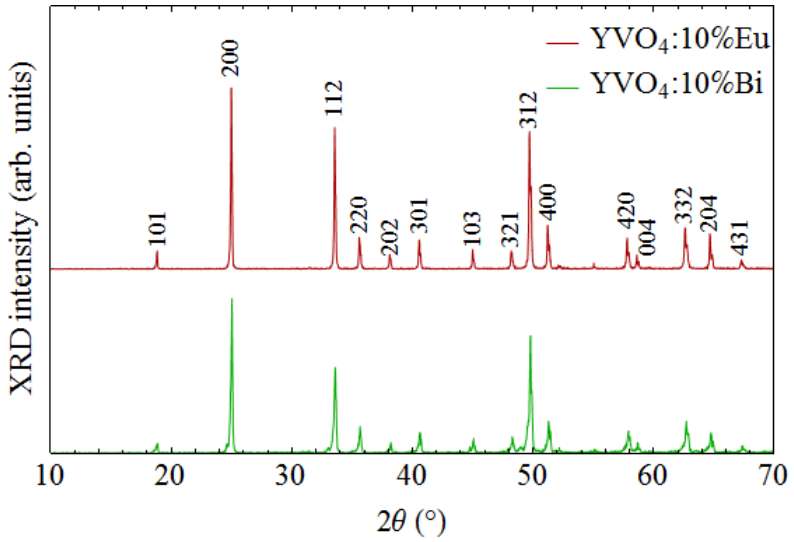

Figure 5.3. Powder diffraction of YVO_4:10%Eu and YVO_4:10%Bi. YVO_4 Bragg peaks are indicated following refs. [12, 37, 38].

A ~3 μm-thick layer of each powder was spread on polyimide tape and covered with 3.6 μm BoPET film. In all measurements (i.e. under UV excitation as well as x-ray excitation), both the incident light and the luminescence were transmitted through the BoPET. Photoluminescence and photoluminescence excitation spectra (Fig. 5.2) were collected using a spectrofluorometer equipped with a CW xenon lamp as the light source (Horiba Fluorolog FL-3). Note the broadening and shift to longer wavelength of the PLE band that occurs upon co-doping with Bi; this is attributed to the introduction of Bi-V charge transfer excitations (Fig. 5.2a) [12, 39]. Our XRD and photoluminescence results are consistent with the results of the similar solid-state reaction used by Huang et al. [12].

Given that our goal is to understand the energy relaxation pathways in these materials, we performed measurements of the photoluminescence lifetimes for the different emission channels (Fig. 5.5). Luminescence decay curves were collected by two methods. The μs-scale decay of the Bi CT emission was measured with a time-correlated single photon counting spectrometer (FluoTime 100/PicoHarp 300); the samples were excited with a 375 nm laser diode (pulse

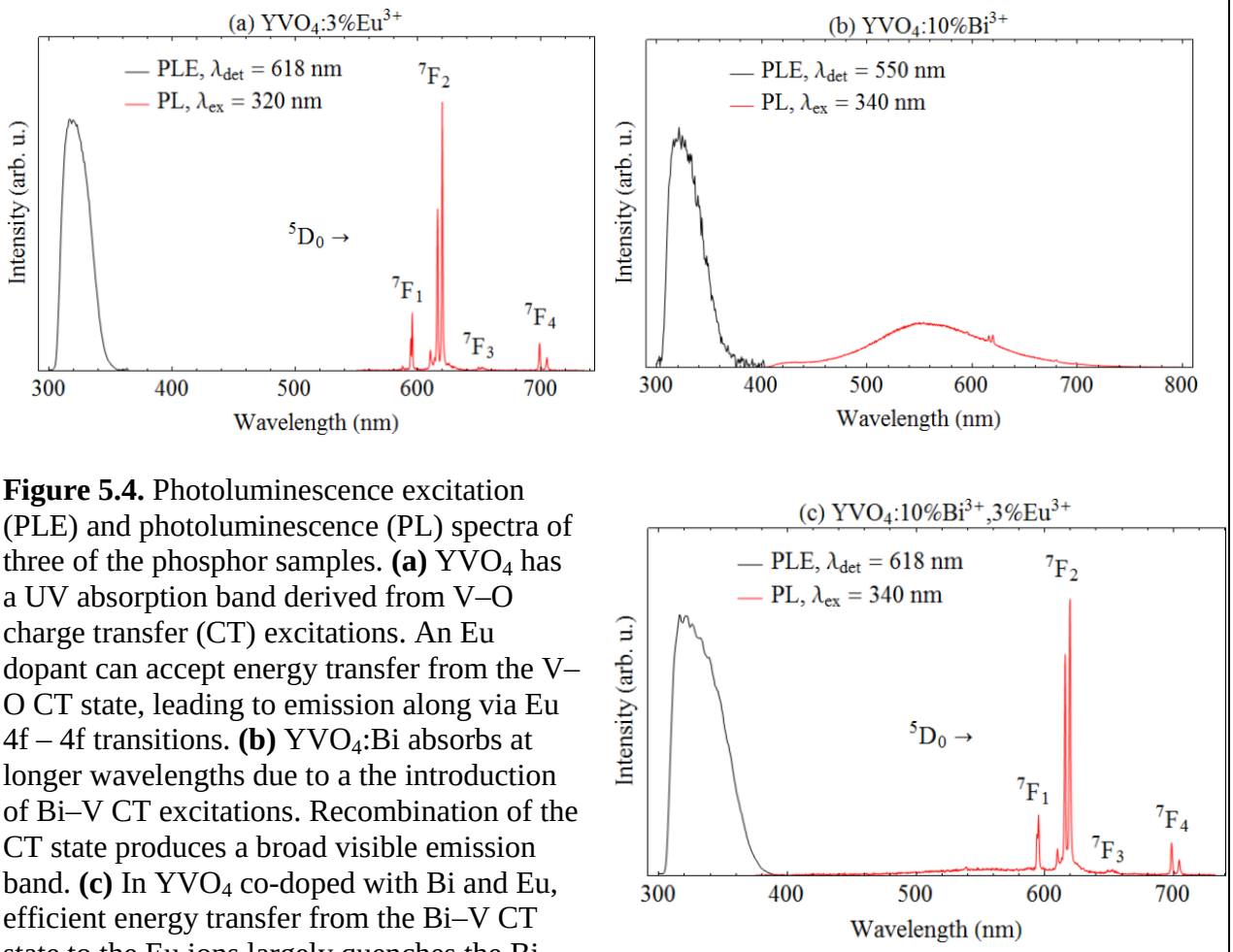

Figure 5.4. Photoluminescence excitation (PLE) and photoluminescence (PL) spectra of three of the phosphor samples. **(a)** YVO_4 has a UV absorption band derived from V–O charge transfer (CT) excitations. An Eu dopant can accept energy transfer from the V–O CT state, leading to emission along via Eu 4f – 4f transitions. **(b)** YVO_4:Bi absorbs at longer wavelengths due to a the introduction of Bi–V CT excitations. Recombination of the CT state produces a broad visible emission band. **(c)** In YVO_4 co-doped with Bi and Eu, efficient energy transfer from the Bi–V CT state to the Eu ions largely quenches the Bi-derived emission.

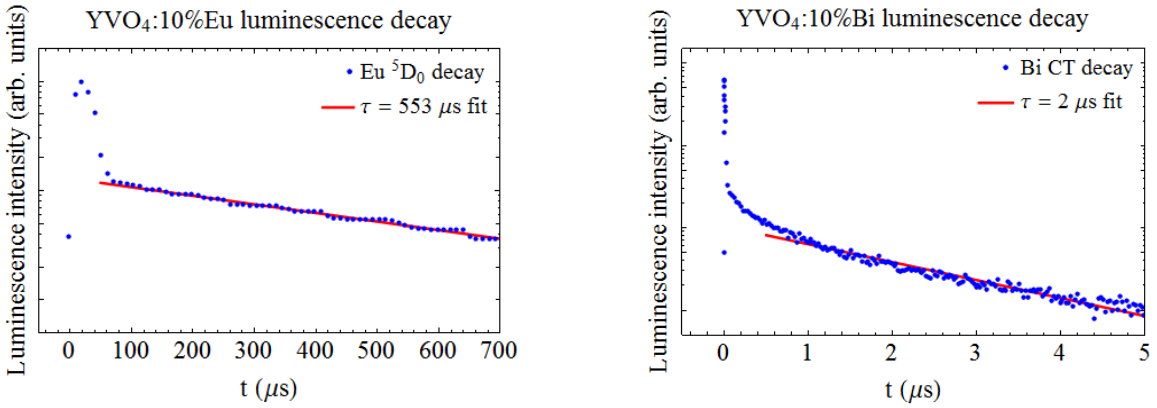

Figure 5.5. Luminescence decays of YVO_4:10%Eu and YVO_4:10%Bi (logarithmic vertical scales). Data were collected with different excitation light sources and detectors; methods are described in the text. 95% confidence intervals for the fits are 546 μs < τ < 559 μs for the Eu luminescence and 1.94 μs < τ < 2.07 μs for the Bi luminescence.

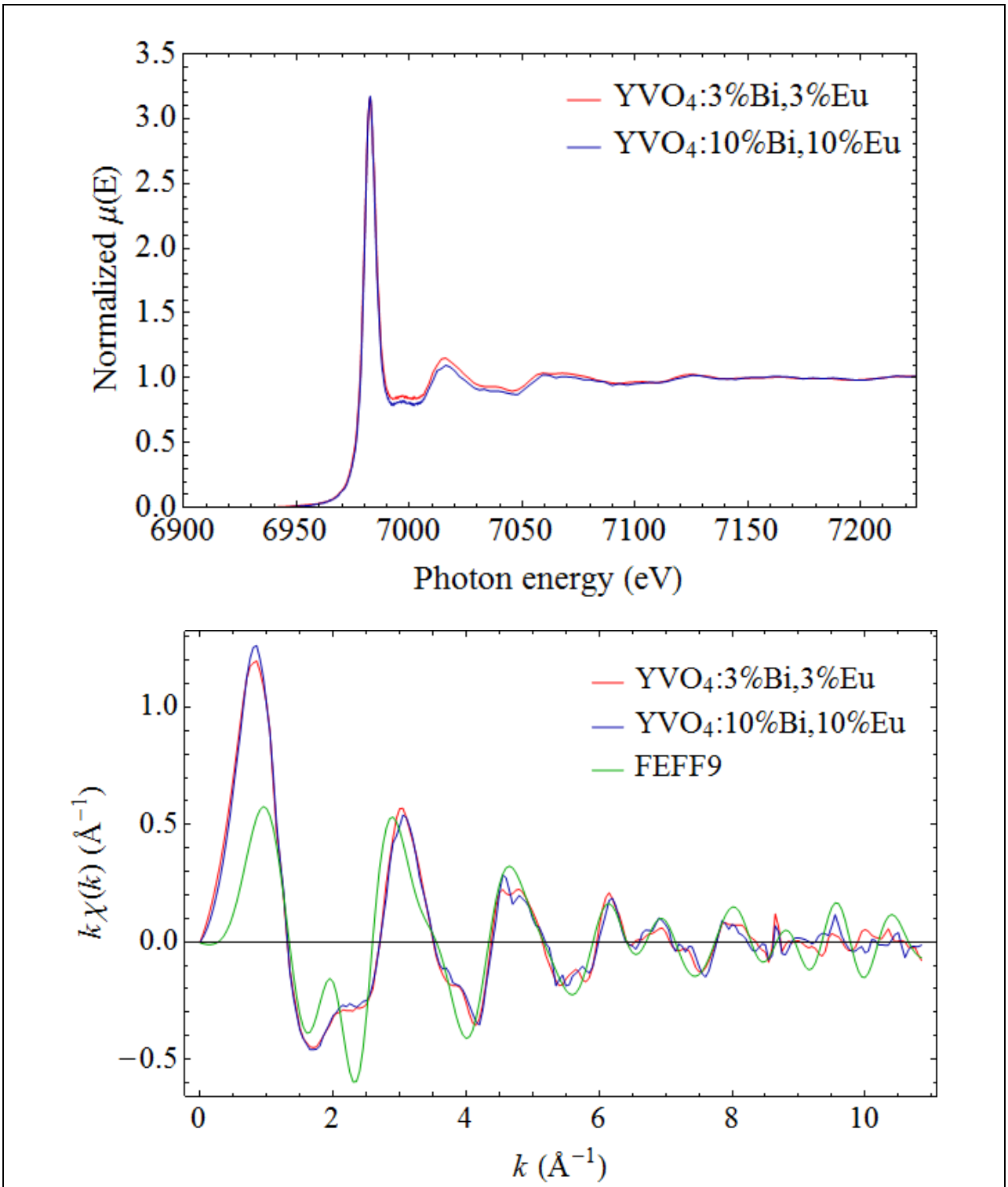

Figure. 5.6. Eu L_3-edge EXAFS of YVO_4:3%Bi,3%Eu and YVO_4:10%Bi,10%Eu in *E* and *k*. We observe no significant change in local coordination on increasing the dopant concentrations. Calculated EXAFS from FEFF9 [40] for an Eu atom substituted at the Y site of YVO_4 [41] is shown with the *k*-space data.

FWHM 80 ps). The ms-scale decay of the Eu $^5D_0$ emission was measured by exciting the sample with a xenon flash lamp (Ocean Optics PX-2, pulse FWHM 4 μs) and monitoring the luminescence with a silicon photodiode (Thorlabs DET36A). A dielectric filter (620 nm center wavelgenth, 10 nm FWHM bandpass) was used to select the $^5D_0 \rightarrow {}^7F_2$ emission for detection by the photodiode. We find lifetimes of 2.00 ± 0.03 μs for the Bi CT emission and 553 ± 3 μs for the Eu $^5D_1 \rightarrow {}^7F_2$ transition. These are consistent with previous studies of YVO_4 doped with varying levels of Bi and Eu [21, 22, 42], which consistently report Eu $^5D_0$ luminescence lifetimes on the order of 500 μs and lifetimes of less than 10 μs for the Eu $^5D_1$, Bi CT, and V-O CT emission at 300 K (with variations caused by dopant levels, temperature, and particle size).

The samples were further characterized by x-ray fluorescence (XRF) and extended x-ray absorption fine structure (EXAFS). Spectra were collected at beamline 20-ID-B of the Advanced Photon Source. XRF data were collected with a Si drift detector and used to verify the dopant concentrations. Lanthanide dopants are reported to substitute for the Y^{3+} ion in doped YVO_4 synthesized by both solid-state and sol-gel methods [12, 37, 38]. To verify this for the Eu present in our samples, we collected EXAFS at the Eu L_3 edge (Fig. 5.6). An Si (111) double crystal monochromator was used to scan the x-ray energy. An ion chamber was used to measure the flux incident on the sample and a Si drift detector was used to monitor the intensity of the Eu Lα radiation. The results are consistent with Eu^{3+} substitution for Y^{3+}, and we observe no significant change in local structure at the Eu sites as the dopant concentrations increase.

5.4 Results and discussion

XEOL measurements were performed at APS beamline 20-ID-B. The monochromator was used to fix the x-ray photon energy at 6982 eV (the peak of the Eu "white line" in Fig. 5.6). The beam was focused to a 5 μm-FWHM spot with Kirpatrick-Baez mirrors, yielding a flux of as

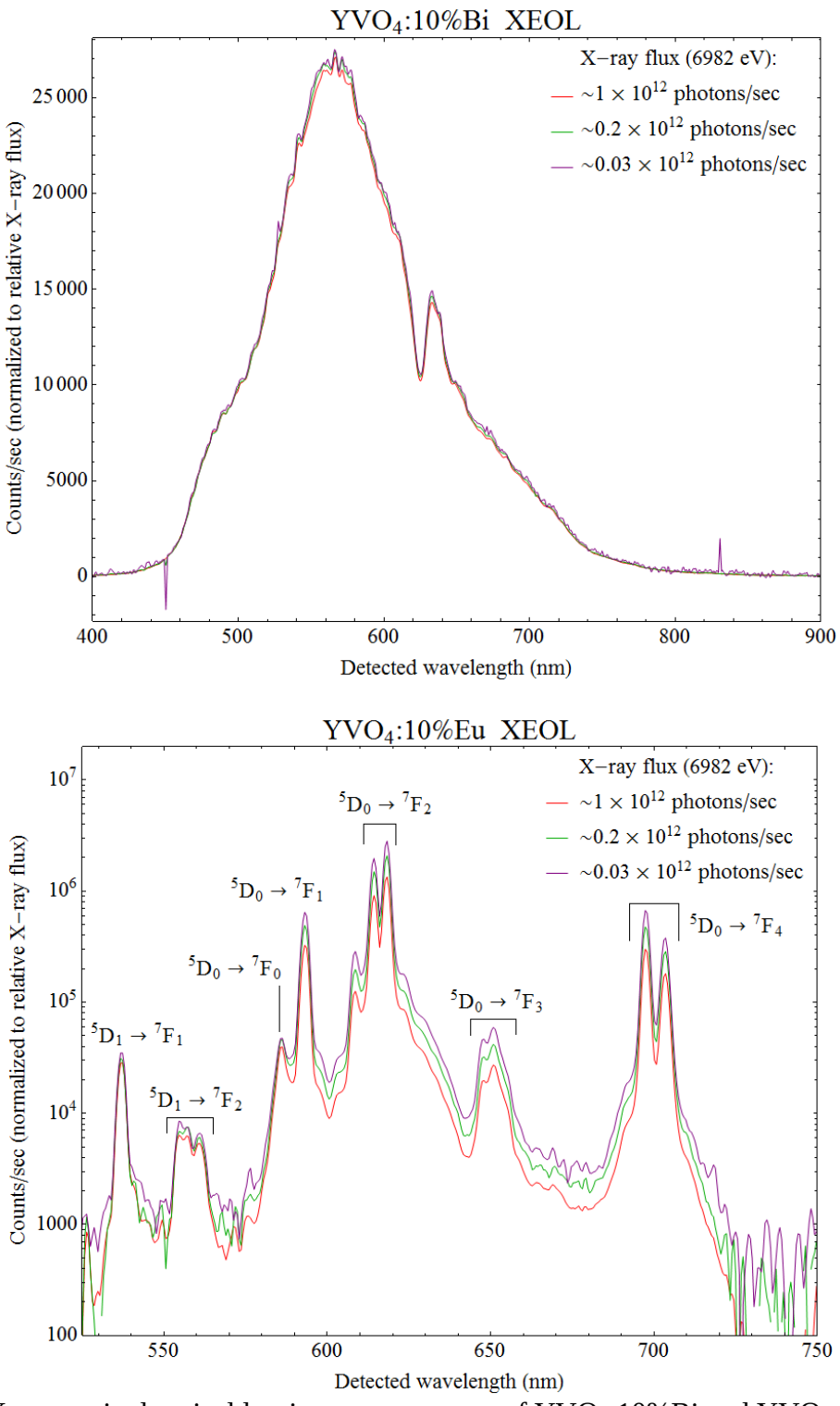

Figure 5.7. X-ray excited optical luminescence spectra of YVO_4:10%Bi and YVO_4:10%Eu under x-ray excitation at several different photon densities. Spectra have been scaled by the x-ray flux; note the logarithmic vertical scale used for the Eu XEOL. The Eu emission lines are identified following ref. [21].

much as ~2 × 10^{12} /s at the sample position. Combinations of Al and Mo foils were used to attenuate the beam to lower intensities by up to three orders of magnitude. Luminescence spectra were collected with a fiber-coupled optical spectrometer (AvaSpec-UL). Data were collected at ambient temperature and at 80 K; low temperatures were maintained with a compact Joule-Thomson refrigerator (MMR Technologies).

Ambient-temperature XEOL spectra collected from YVO_4:10%Bi and YVO_4:10%Eu at several different x-ray fluxes are shown in Fig. 5.7. We immediately observe that the CT-derived Bi emission scales linearly with the x-ray intensity, while several of the Eu emission lines saturate at high incident flux. In particular, emission lines derived from the Eu $^5D_0$ 4f-intrashell excitted state saturate, while the weaker emission lines derived from the $^5D_1$ state do not. In the low-temperature XEOL spectra from YVO_4:10%Eu, band emission from the YVO_4 host lattice is also observed (Fig. 5.8), and scales linearly with the x-ray flux. We conclude that the observed nonlinear response of the XEOL is specifically due to nonradiative quenching of the $^5D_0$ state.

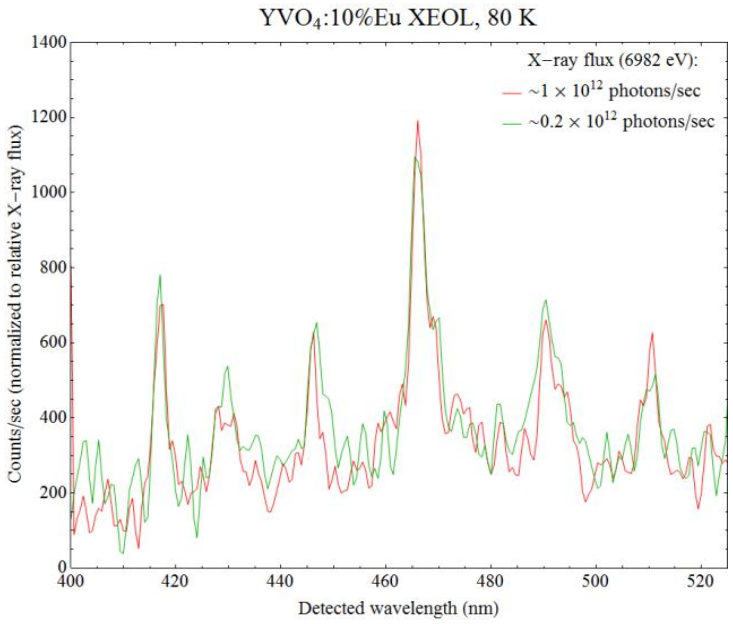

Figure 5.8. Low-temperature XEOL of YVO_4:10%Eu. Note that both vertical and horizontal scales differ from those in Figure 5.6; this range of wavelengths includes a broad background due to VO_4^{3-} band emission and several weak lines due to Eu $^5D_2 \rightarrow {}^7F_J$ transitions.

We also note that note that the interval between the x-ray pulses produced by the APS (153 ns) is an order of magnitude shorter than the lifetimes of all the excited states involved in the luminescence of the samples. The XEOL measurements can therefore be treated as data taken under continuous rather than pulsed illumination. With this context established, we next discuss the applicability of several saturation mechanisms that have been described in the literature.

5.4.1 Possible saturation mechanisms

The application of phosphors to cathode-ray tube displays has led to extensive studies of saturation behavior under various operating conditions [43-46]. Consequently, we can draw on well-established modeling strategies for cathode-ray excitation and straightforwardly extend them to x-ray excitation.

One possibility is that a significant fraction of the Eu ions in the sample may be driven into the $^5D_0$ excited states at high x-ray flux, leading to a saturation bottleneck in the excitation of the Eu ions by the cascade of secondary fast electrons that result from the high incident x-ray flux. This effect is referred to as ground-state depletion, and is commonly observed in luminescent systems with long excited state lifetimes [47, 48]. To determine whether this effect is significant, we estimate the rates of energy absorption and dissipation by the sample. The 3 μm-thick sample absorbs approximately 20% of the x-ray beam, so (with the maximum x-ray flux used in this experiment) the rate of energy deposition is 3×10^{15}eV/s. This rate is largely independent of the dopant concentrations, as the photoelectric cross section at the photon energy used here is dominated by the YVO_4 host lattice (Table 5.1). For the specific case of YVO_4:10%Eu, the x-ray-illuminated volume of sample contains approximately 10^{11}Eu atoms, giving 3×10^4eV/s per Eu ion deposited in the material.

For an estimate of the fraction of this energy that is actually converted into electron-hole pairs, we can again draw on the cathode-ray phosphor literature. Statistical models show that for YVO_4 in particular, the efficiency of this process is approximately 8%, with most of the loss due to creation of high-frequency phonons [49, 50]. The deposition rate for energy capable of producing luminescence is therefore less than 3×10^3eV/s per Eu ion. Note that this is still an overestimate of the energy that can be transported to a typical Eu site, since energy is deposited near-uniformly through the material and the dopants are relatively dilute.

YVO_4	**0% Bi**	**3% Bi**	**10% Bi**
0% Eu	230 kb	240 kb	260 kb
3% Eu	240 kb	250 kb	270 kb
10% Eu	260 kb	270 kb	290 kb

Table 5.1. Estimates of the photoelectric absorption cross sections at 7 keV for YVO_4 doped with varying levels of Bi and Eu. Data are derived from ref. [51], and are given as cross sections for an average unit cell (four formula units).

Next, to calculate a lower bound for the power that each Eu atom can dissipate, we can assume that one photon is emitted via the hypersensitive $^5D_0 \rightarrow {}^7F_2$ transition every ~500 μs (Fig. 5.5), giving 4×10^3eV/s emitted. Comparing this with the rate of energy deposition, we conclude that most of the x-ray flux densities used in this study are well below the regime needed for ground state depletion to become significant.

Two other considerations add to the rationale for ruling out ground state depletion. First, the power per unit area absorbed by the sample (approximately 10^5 W/cm^2) is an order of magnitude lower than typically necessary to reach the ground-state depletion with cathode-ray excitation [52]. Second, the fact that we observe no saturation of the $^5D_1$ emission lines implies

that the initial Eu excitation is still a linear process in this regime, i.e., we have not driven a significant fraction of the Eu ions out of the ground state.

Second, we consider temperature quenching, as a possible consequence of x-ray heating of the thin sample. Struck and Fonger [53, 54] reported thermally assisted quenching of the Eu emission in several phosphors. At high temperatures, the probability of back-transfer from the Eu ion to the host lattice becomes significant. This quenches the Eu emission lines sequentially, beginning with the lines derived from higher-energy ^5D_J states. The $^5D_1 \rightarrow {}^7F_J$ lines therefore quench before the $^5D_0 \rightarrow {}^7F_J$ lines; this does not correspond with the behavior seen in Fig. 5.3, ruling out this mechanism. In addition, the heat capacity of YVO_4 at 300 K is approximately 100 J/(K mol) [55], and as a result the energy deposited by each x-ray pulse (as calculated above) raises the sample temperature by less than 0.1 K.

5.4.2 Analysis in terms of energy loss via cross-relaxation

Finally, we consider cross-relaxation quenching. In this process, pairs of excited Eu ions may simultaneously undergo nonradiative transitions in which one ion returns to the ground state while the second is excited to a higher-energy state (Fig. 5.1b). Since this is a two-atom process, the rate at which it occurs is quadratic in the density of excited Eu ions. When the magnitudes of the relevant cross-sections and rate constants are considered, it is known that cross-relaxation can contribute significantly even when ground-state depletion is relatively insignificant [56]. In particular, we find that a kinetic model developed by de Leeuw and ’t Hooft [52] gives an excellent fit to the observed behavior.

First, we summarize their calculation for the case of an activator with a single sensitizer; in the present study, this applies to YVO_4:Eu. A schematic of the energy flow is shown in Fig. 5.9. In a simplification from the full map of excited states shown in Fig. 5.2, both the sensitizer

(VO_4^{3-}) and the activator (Eu^{3+}) are treated as two-level systems. In particular, all of the intermediate steps between the V-O charge transfer excitation and the emitting Eu^{3+} $^5D_0$ state are modeled as a single transfer of energy. In Table 5.2, notation is defined for the populations of each state and the rate constants for transitions between them.

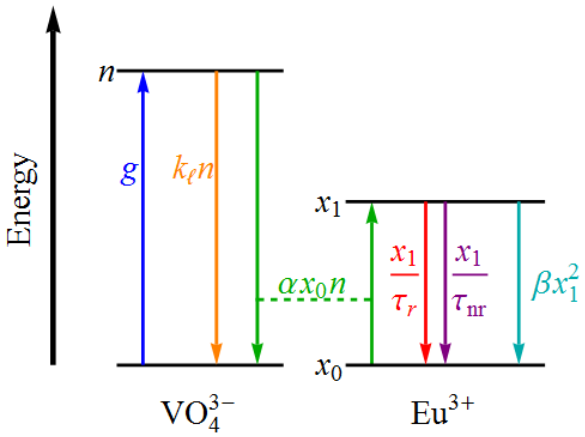

Figure 5.9. Simplified schematic of energy flow in YVO_4:Eu, adapted from ref. [52]. Notation is defined in Table 5.1.

ϕ_{in}	Incident x-ray flux
ϕ_{det}	Detected luminescence count rate
n	Density of V-O charge transfer (CT) excitations
g	Rate of creation (per unit volume) of V-O CT states by x-ray beam
k_ℓ	Overall rate constant for decay of the V-O CT state (via any process)
α	Rate constant for nonradiative ET from the V-O CT state to the Eu^{3+} $^5D_0$ state
N	Density of Eu^{3+} dopant in the phosphor
x_0	Density of Eu^{3+} ions in the ground state
x_1	Density of Eu^{3+} ions in the $^5D_0$ state
τ_r	Radiative decay lifetime of the $^5D_0$ state of Eu^{3+}
τ_{nr}	Nonradiative decay lifetime of the $^5D_0$ state of Eu^{3+}
τ	Observed luminescence decay lifetime
β	Rate constant for cross-relaxation losses from the $^5D_0$ state of Eu^{3+}

Table 5.2. Notation for kinetic modeling of the energy flow in YVO_4:Eu under x-ray excitation.

Electron-hole pairs are created in the YVO_4 host at a rate proportional to the x-ray flux ϕ_{in}. These are in turn converted into V-O charge transfer (CT) excitations at a rate $g \propto \phi_{in}$, producing a density n of excited vanadate groups. The CT state may return to the ground state through radiative or nonradiative processes, with a rate constant k_ℓ for the decay of lattice excitations. Transfer of energy from the V-O CT state to the Eu $^5D_1$ state proceeds at a rate proportional to both n and the density of Eu^{3+} ions in the ground state, x_0. The continuity equation for the sensitizer is therefore

$$\frac{dn}{dt} = g - k_\ell n - \alpha x_0 n. \tag{5.1}$$

The Eu^{3+} state may decay by emitting a photon, by a nonradiative transition involving a single Eu^{3+} ion, or by cross-relaxation of a pair of Eu^{3+} ions. The first two processes are linear in the density of excited Eu^{3+} ions (x_1), while the cross-relaxation rate depends on x_1 quadratically. The continuity equation for the Eu ions is

$$\frac{dx_1}{dt} = \alpha x_0 n - \frac{x_1}{\tau_r} - \frac{x_1}{\tau_{nr}} - \beta x_1^2. \tag{5.2}$$

Since we are in a regime where ground state depletion can be neglected, i.e. $x_1 \ll x_0$, we can take x_0 to be simply the overall density of Eu^{3+} ions in the phosphor. In the steady state, $\frac{dn}{dt} = \frac{dx_1}{dt} = 0$ and we can eliminate n to obtain

$$\beta x_1^2 + \frac{1}{\tau} x_1 - \frac{\alpha x_0}{k_\ell + \alpha x_0} g = 0, \tag{5.3}$$

where, to simplify the notation, we have written

$$\frac{1}{\tau_r} + \frac{1}{\tau_{nr}} = \frac{1}{\tau}. \tag{5.4}$$

Experimentally, τ is the measured lifetime of the $^5D_1$-derived luminescence. Eq. (5.3) gives

$$x_1 = \frac{1}{2\beta\tau}\left[\sqrt{1 + \frac{\alpha x_0}{k_\ell + \alpha x_0}(4\beta\tau^2 g)} - 1\right]. \tag{5.5}$$

It is instructive to compare Eqn. (5.5) with the result in the linear regime, which can be derived by either (1) considering the limit of low excitation density ($g \to 0$), or (2) simply neglecting the quadratic term in Eq. (5.3):

$$\frac{x_1}{\tau} = \frac{\alpha x_0}{k_\ell + \alpha x_0} g. \tag{5.6}$$

Here, x_1/τ is the rate at which the excited Eu ions return to the ground state. In the steady state, this must equal the rate at which the excited state is repopulated. The right-hand side represents the rate at which lattice excitations are converted into Eu excited states, with an efficiency $\alpha x_0/(k_\ell + \alpha x_0)$ determined by two competing rate constants. A lower bound for this quantity is the overall quantum efficiency of YVO_4:Eu under UV illumination, approximately 70% [57]. For the purposes of our calculation we will take $\alpha x_0/(k_\ell + \alpha x_0) = 0.7$ with a systematic uncertainty of 0.1. (Systematic uncertainties are further discussed below.)

The rate constant for cross-relaxation, β, can be estimated from a two-parameter fit to the data as follows. We absorb the proportionality constant ϕ_{det}/x_1, as well as the factor $1/2\beta\tau$, into a dimensionless constant K, so that Eq. (5.5) becomes

$$\phi_{det} = K\left[\sqrt{1 + \frac{\alpha x_0}{k_\ell + \alpha x_0}(4\beta\tau^2 g)} - 1\right]. \tag{5.7}$$

Next, we estimate the proportionality constant between g and ϕ_{in}. If we assume that the X ray-derived photoelectrons deposit energy in the same way as cathode-ray electrons of the same energy, we can again use existing results [49, 50] to deduce that each absorbed X ray produces ~125 V-O excitations. This gives

$$g \approx 1.6 \times 10^{12}\text{cm}^{-3}\text{s}^{-1} \times \phi_{in}. \tag{5.8}$$

Finally, using the estimate for $\alpha x_0/(k_\ell + \alpha x_0)$ derived from the overall quantum efficiency of the phosphor, we have

$$\phi_{det} \approx K\left[\sqrt{1 + 4\beta\tau^2(1.1 \times 10^{12}\text{cm}^{-3}\text{s}^{-1})\phi_{in}} - 1\right]. \tag{5.9}$$

Eq. (5.12) can be fitted to the data using K and $\beta\tau^2$ as the parameters. The constant K scales out variations in, e.g., differences in sample thickness and detector geometry between measurements. Finally, by measuring the luminescence lifetime τ, we can calculate the rate constant β. It should be noted that there is a large systematic error (~20%) in the conversion between g and ϕ_{in}, due to (1) the estimate for $\alpha x_0/(k_\ell + \alpha x_0)$ and (2) uncertainties in the measurement of absolute photon fluxes with the ion chamber, e.g., due to uncertainty in the mixture of gases present.

The experimental measurement of the XEOL yield from YVO4:10%Eu is shown in Fig. 5.10, together with the results of this fitting procedure. The fluorescence yield was calculated by integrating the count rate across the $^5D_0 \rightarrow {}^7F_2$ emission lines, i.e. the wavelengths between 610 and 620 nm (see Figs. 5.4 and 5.7). We find that $K = (1.89 \pm 0.01) \times 10^6$ and $\beta\tau^2 = (1.13 \pm 0.04) \times 10^{-23}$ cm^{3}s. Errors reported here are 95% confidence level intervals from the fit; again, we emphasize that there is a systematic uncertainty of ~20% in both parameters. The linear behavior at low ϕ_{in} strongly constrains K, while $\beta\tau^2$ has a relatively larger uncertainty due to statistical errors in the XEOL intensity measurements. We measured τ to be 553 ± 3 μs (Section 5.3), and hence $\beta = (3.70 \pm 0.13) \times 10^{-17}\text{cm}^3\text{s}^{-1}$.

To validate this result, we can obtain an order-of-magnitude estimate of x_1, the time-averaged density of Eu ions in the $^5D_0$ state, as follows. The luminescence yield deviates from linear dependence on ϕ_{in} when the cross-relaxation rate βx_1^2 is comparable to the single-atom decay rate x_1/τ. That is, cross-relaxation becomes significant when

$$x_1 \approx \frac{1}{\beta\tau} = (4.89 \pm 0.17) \times 10^{19}/\text{cm}^3. \tag{5.10}$$

This is approximately 4% of the total density of Eu^{3+} in YVO_4:10%Eu. We conclude that we are well below the regime of ground state depletion, and that cross-relaxation is in fact the dominant luminescence saturation mechanism at the x-ray fluxes used in this experiment.

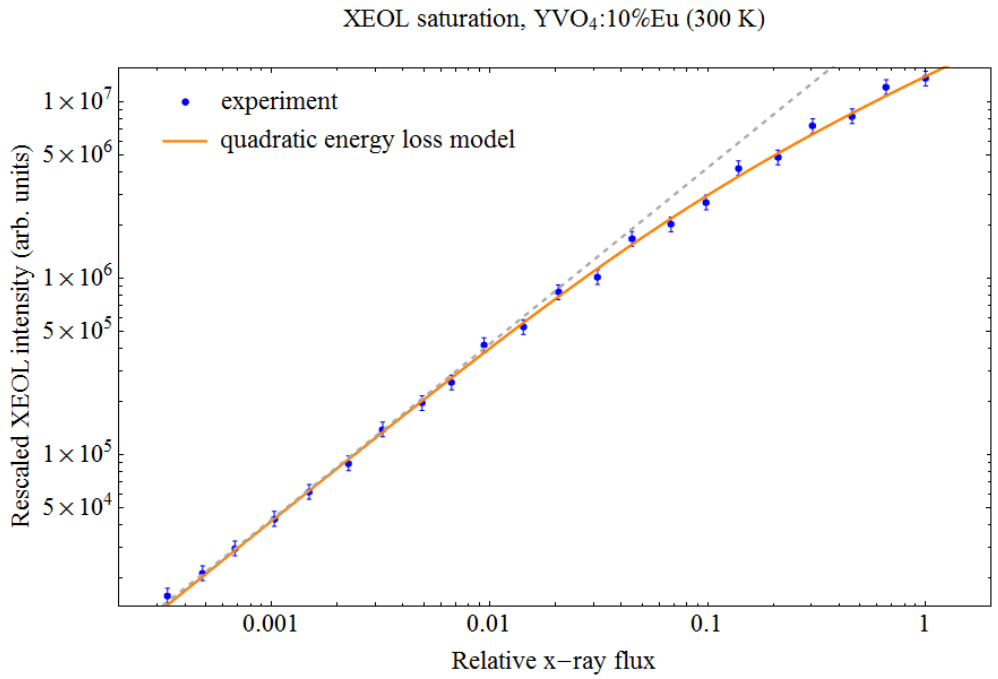

Figure 5.10. X-ray flux dependence of the luminescence yield of YVO_4:10%Eu at room temperature. The solid curve is a fit to the cross-relaxation model in Eq. (5.7). The dashed line is a linear extrapolation of the low-flux data, using the fit parameter K in Eq. (5.8). Values of the incident x-ray flux have been rescaled by the maximum flux used, approximately $8 \times 10^{10}/\mu m^2$; the ion chamber used to monitor the x-ray flux responds linearly over the range used, but there is a ~20% systematic uncertainty in the absolute photon count due to uncertainty in the relative He/N_2 content of the chamber. Error bars are derived from measured fluctuations in the x-ray flux and XEOL yield (see Section 5.6); the horizontal error bars are not visible at this scale.

Before concluding, it is interesting to compare the XEOL yields from several samples. In Fig. 5.11, the relative luminescence yields of YVO_4:10%Bi and YVO_4:10%Eu are plotted together with the Eu- and Bi-derived XEOL yields of YVO_4:10%Bi,10%Eu. The vertical axes have been rescaled by fitting each dataset as described above and dividing out the parameter K,

enabling a quantitative comparison across samples. We again observe linear scaling of the Bi luminescence and identical saturation behavior in the Eu luminescence, regardless of which dopant species are present. This implies that the Bi co-dopant has a negligible effect on the cross-relaxation process. Additional studies (e.g., time-resolved measurements of the rise and decay times of the Bi and Eu XEOL) are needed to more precisely determine the role of the Bi ion in the excited state cascade that follows x-ray excitation.

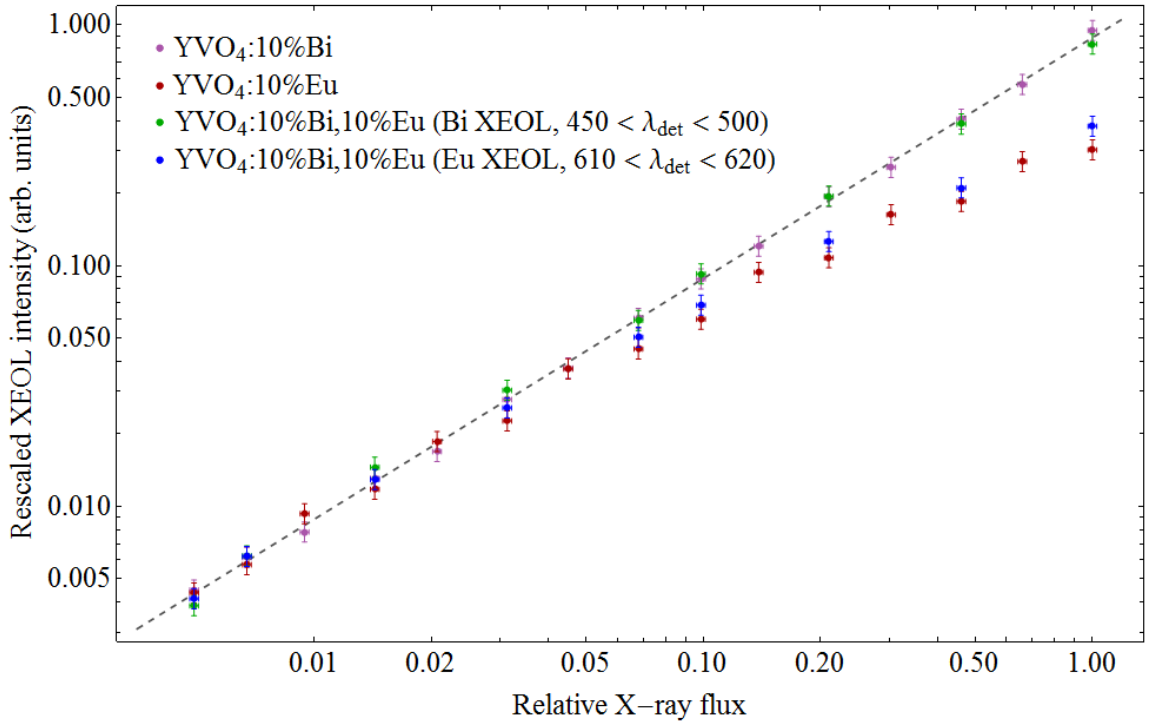

Figure 5.11. Saturation behavior of singly-doped and co-doped samples at room temperature. The dashed line is a fit to the luminescence yield of YVO4:10%Bi. In both YVO_4:Bi and YVO_4:Bi,Eu, the Bi luminescence yield scales linearly with x-ray flux, while the Eu-derived luminescence yield of YVO_4:Bi,Eu shows saturation behavior identical to that in YVO_4:Eu.

5.5 Conclusion

We have positively identified cross-relaxation as the dominant saturation mechanism in the x-ray excited optical luminescence of several Eu-doped phosphors. This conclusion is supported by estimates of the energy deposition rate and by kinetic modeling based on the

literature on saturation effects in cathode ray-excited phosphors. We used a microfocused beam of X rays produced by an insertion device beamline at a third-generation synchrotron light source to reach high flux densities. To our knowledge, this is the first study of XEOL saturation effects in this regime. Two categories of further studies are potentially of interest. First, time-resolved XEOL measurements would clarify the kinetics of the sequence of excited states induced by the bath of photoelectrons; this would be particularly useful for disentangling the roles of the VO_4^{3-} and Bi^{3+} sensitizers in co-doped phosphors. Second, studies at higher flux, e.g. with a non-monochromatic synchrotron beam, are needed to identify the flux density at which ground-state depletion becomes important. This is important technical background for future studies of solid-state luminescent materials, which will require short, high-intensity pulses of X rays (as produced, for example, at x-ray free electron laser facilities).

5.6 References

1. Moore, E.G., A.P.S. Samuel, and K.N. Raymond, *From Antenna to Assay: Lessons Learned in Lanthanide Luminescence.* Accounts of Chemical Research, 2009. **42**(4): p. 542-552.
2. Soini, E. and I. Hemmila, *Fluoroimmunoassay - Present Status and Key Problems.* Clinical Chemistry, 1979. **25**(3): p. 353-361.
3. Soini, E. and T. Lovgren, *Time-Resolved Fluorescence of Lanthanide Probes and Applications in Biotechnology.* Crc Critical Reviews in Analytical Chemistry, 1987. **18**(2): p. 105-154.
4. Eliseeva, S.V. and J.C.G. Bunzli, *Rare earths: jewels for functional materials of the future.* New Journal of Chemistry, 2011. **35**(6): p. 1165-1176.
5. Bunzli, J.C.G.E., S. V., *Basics of Lanthanide Photophysics,* in *Lanthanide Luminescence*, H.P.H. H., Editor 2011, Springer Berlin Heidelberg. p. 1-45.
6. Miniscalco, W.J., *Erbium-Doped Glasses for Fiber Amplifiers at 1500-Nm.* Journal of Lightwave Technology, 1991. **9**(2): p. 234-250.
7. Slooff, L.H., et al., *Rare-earth doped polymers for planar optical amplifiers.* Journal of Applied Physics, 2002. **91**(7): p. 3955-3980.
8. Bunzli, J.C.G. and S.V. Eliseeva, *Lanthanide NIR luminescence for telecommunications, bioanalyses and solar energy conversion.* Journal of Rare Earths, 2010. **28**(6): p. 824-842.
9. Reisfeld, R. and C.K.l. Jørgensen, *Lasers and excited states of rare earths.* 1977, Berlin; New York: Springer-Verlag.

10. Kuriki, K., Y. Koike, and Y. Okamoto, *Plastic optical fiber lasers and amplifiers containing lanthanide complexes.* Chemical Reviews, 2002. **102**(6): p. 2347-2356.
11. Wegh, R.T., et al., *Visible quantum cutting in $LiGdF_4:Eu^{3+}$ through downconversion.* Science, 1999. **283**(5402): p. 663-666.
12. Huang, X.Y., et al., *Spectral conversion for solar cell efficiency enhancement using YVO4:Bi3+,Ln(3+) (Ln = Dy, Er, Ho, Eu, Sm, and Yb) phosphors.* Journal of Applied Physics, 2011. **109**(11).
13. Trupke, T., et al., *Efficiency enhancement of solar cells by luminescent up-conversion of sunlight.* Solar Energy Materials and Solar Cells, 2006. **90**(18-19): p. 3327-3338.
14. Richards, B.S., *Enhancing the performance of silicon solar cells via the application of passive luminescence conversion layers.* Solar Energy Materials and Solar Cells, 2006. **90**(15): p. 2329-2337.
15. Richards, B.S., *Luminescent layers for enhanced silicon solar cell performance: Down-conversion.* Solar Energy Materials and Solar Cells, 2006. **90**(9): p. 1189-1207.
16. ASTM, *Standard Tables for Reference Solar Spectral Irradiances: Direct Normal and Hemispherical on 37° Tilted Surface*, 2012.
17. Smets, B.M.J., *Phosphors Based on Rare-Earths, a New Era in Fluorescent Lighting.* Materials Chemistry and Physics, 1987. **16**(3-4): p. 283-299.
18. Dolgos, M.R., et al., *The electronic structures of vanadate salts: Cation substitution as a tool for band gap manipulation.* Journal of Solid State Chemistry, 2009. **182**(7): p. 1964-1971.
19. Zhang, Q.Y. and X.Y. Huang, *Recent progress in quantum cutting phosphors.* Progress in Materials Science, 2010. **55**(5): p. 353-427.
20. Levine, A.K. and F.C. Palilla, *A New, Highly Efficient Red-Emitting Cathodoluminescent Phosphor ($YVO_4:Eu$) for Color Television.* Applied Physics Letters, 1964. **5**(6): p. 118.
21. Riwotzki, K. and M. Haase, *Wet-chemical synthesis of doped colloidal nanoparticles: YVO_4:Ln (Ln = Eu, Sm, Dy).* Journal of Physical Chemistry B, 1998. **102**(50): p. 10129-10135.
22. Riwotzki, K. and M. Haase, *Colloidal $YVO_4:Eu$ and $YP_{0.95}V_{0.05}O_4:Eu$ nanoparticles: Luminescence and energy transfer processes.* Journal of Physical Chemistry B, 2001. **105**(51): p. 12709-12713.
23. Takeshita, S., T. Isobe, and S. Niikura, *Low-temperature wet chemical synthesis and photoluminescence properties of YVO(4): Bi(3+), Eu(3+) nanophosphors.* Journal of Luminescence, 2008. **128**(9): p. 1515-1522.
24. Takeshita, S., et al., *Effects of the homogeneous Bi^{3+} doping process on photoluminescence properties of $YVO_4:Bi^{3+},Eu^{3+}$ nanophosphor.* Journal of Luminescence, 2009. **129**(9): p. 1067-1072.
25. Buchanan, R.A., Wickersh.Ka, and Finkelst.Si, *X-Ray Exposure Reduction Using Rare-Earth Oxysulfide Intensifying Screens.* Radiology, 1972. **105**(1): p. 185-&.
26. Cavouras, D., et al., *An evaluation of the Y2O3:Eu3+ scintillator for application in medical x-ray detectors and image receptors.* Medical Physics, 1996. **23**(12): p. 1965-1975.
27. Brixner, L.H., *New X-Ray Phosphors.* Materials Chemistry and Physics, 1987. **16**(3-4): p. 253-281.
28. Makovsky, J., W. Low, and S. Yatsiv, *Excitation of Optical Fluorescence Spectra of Transition Elements by Means of X-Rays.* Physics Letters, 1962. **2**(4): p. 186-187.

29. Linares, R.C., Schroede.Jb, and L.A. Hurlbut, *Applications of X-Ray Excited Optical Fluorescence to Analytical Chemistry.* Spectrochimica Acta, 1965. **21**(11): p. 1915-&.
30. Jaworows.Rj, et al., *Determination of Trace Rare Earths by X-Ray Excited Optical Fluorescence.* Spectrochimica Acta Part B-Atomic Spectroscopy, 1968. **B 23**(11): p. 751-&.
31. Ozawa, L. and T. Toryu, *Quantitative Determination of Rare Earths in Yttrium Oxide by Spectrophotoluminescence.* Analytical Chemistry, 1968. **40**(1): p. 187-&.
32. Armelao, L., et al., *X-ray excited optical luminescence studies of ZnO and Eu-doped ZnO nanostructures (vol 111, pg 10199, 2007).* Journal of Physical Chemistry C, 2007. **111**(49): p. 18444-18444.
33. Rosenberg, R.A., et al., *Determination of the local structure of luminescent sites in ZnS nanowires using x-ray excited optical luminescence.* Applied Physics Letters, 2005. **87**(25).
34. Heigl, F., et al., *Time-resolved X-ray excited optical luminescence from tris(2-phenyl bipyridine) iridium (vol 128, pg 3906, 2006).* Journal of the American Chemical Society, 2006. **128**(28): p. 9257-9257.
35. Soo, Y.L., et al., *X-ray excited luminescence and local structures in Tb-doped Y2O3 nanocrystals.* Journal of Applied Physics, 1998. **83**(10): p. 5404-5409.
36. Sham, T.K., et al., *Origin of Luminescence from Porous Silicon Deduced by Synchrotron-Light-Induced Optical Luminescence.* Nature, 1993. **363**(6427): p. 331-334.
37. Huignard, A., T. Gacoin, and J.P. Boilot, *Synthesis and luminescence properties of colloidal YVO4 : Eu phosphors.* Chemistry of Materials, 2000. **12**(4): p. 1090-1094.
38. Cho, Y.S. and Y.D. Huh, *Preparation of Transparent Red-Emitting YVO4:Eu Nanophosphor Suspensions.* Bulletin of the Korean Chemical Society, 2011. **32**(1): p. 335-337.
39. Blasse, G., *The influence of charge-transfer and rydberg states on the luminescence properties of lanthanides and actinides.* Structure and Bonding, 1976. **26**: p. 43-79.
40. Rehr, J.J., et al., *Parameter-free calculations of X-ray spectra with FEFF9.* Physical Chemistry Chemical Physics, 2010. **12**(21): p. 5503-5513.
41. Baglio, J.A. and G. Gashurov, *A Refinement of Crystal Structure of Yttrium Vanadate.* Acta Crystallographica Section B-Structural Crystallography and Crystal Chemistry, 1968. **B 24**: p. 292-&.
42. Stickrath, A.B., et al., *Detailed Transient Heme Structures of Mb-CO in Solution after CO Dissociation: An X-ray Transient Absorption Spectroscopic Study.* Journal of Physical Chemistry B, 2013. **117**(16): p. 4705-4712.
43. Bril, A., *On the Saturation of Fluorescence with Cathode-Ray Excitation.* Physica, 1949. **15**(3-4): p. 361-379.
44. Meyer, V.D. and F.C. Palilla, *Phosphor Screens for High-Current-Density Cathode-Ray Tubes.* Journal of the Electrochemical Society, 1969. **116**(4): p. 535-&.
45. Gibbons, E.F., et al., *Technique for Measuring Saturation of Phosphors at High-Current Densities.* Journal of the Electrochemical Society, 1973. **120**(12): p. 1730-1734.
46. Vanderweg, W.F. and M.W. Vantol, *Saturation Effects of Cathodoluminescence in Rare-Earth Activated Epitaxial Y3al5o12 Layers.* Applied Physics Letters, 1981. **38**(9): p. 705-707.

47. Tobita, S., M. Arakawa, and I. Tanaka, *Electronic Relaxation Processes of Rare-Earth Chelates of Benzoyltrifluoroacetone.* Journal of Physical Chemistry, 1984. **88**(13): p. 2697-2702.
48. Hao, J.H., J. Gao, and M. Cocivera, *Green, blue, and yellow cathodoluminescence of Ba2B5O9Cl thin-films doped with Tb3+, Tm3+, and Mn2+.* Applied Physics Letters, 2003. **82**(14): p. 2224-2226.
49. Robbins, D.J., *On Predicting the Maximum Efficiency of Phosphor Systems Excited by Ionizing-Radiation.* Journal of the Electrochemical Society, 1980. **127**(12): p. 2694-2702.
50. Vanroosb.W, *Theory of Yield and Fano Factor of Electron-Hole Pairs Generated in Semiconductors by High-Energy Particles.* Physical Review, 1965. **139**(5A): p. 1702-&.
51. McMaster, W.H., et al., *Compilation of X-ray Cross Sections*, 1969, Lawrence Livermore National Laboratory.
52. Deleeuw, D.M. and G.W. Thooft, *Method for the Analysis of Saturation Effects of Cathodoluminescence in Phosphors - Applied to Zn_2SiO_4-Mn and $Y_3Al_5O_{12}$-Tb.* Journal of Luminescence, 1983. **28**(3): p. 275-300.
53. Struck, C.W. and W.H. Fonger, *Thermal Quenching of Tb+3, Tm+3, Pr+3, and Dy+3 4fn Emitting States in La2o2s.* Journal of Applied Physics, 1971. **42**(11): p. 4515-&.
54. Fonger, W.H. and C.W. Struck, *Eu^{3+} ^5D Resonance Quenching to Charge-Transfer States in Y_2O_2S, La_2O_2S, and LaOCl.* Journal of Chemical Physics, 1970. **52**(12): p. 6364.
55. Gavrichev, K.S., et al., *Heat capacity and thermodynamic functions of YVO4 in the 13-347 K region.* Russian Journal of Inorganic Chemistry, 2010. **55**(12): p. 1935-1939.
56. Tolstoi, N.A. and A.P. Abramov, *On a Possible Theoretical Interpretation of Nonlinear Quenching.* Optics and Spectroscopy-Ussr, 1966. **20**(3): p. 273-&.
57. Ropp, R.C., *Spectra of Some Rare Earth Vanadates.* Journal of the Electrochemical Society, 1968. **115**(9): p. 940.

Chapter 6. Conclusion

6.1 Summary

This dissertation presented several studies of the excited state cascade in luminescent lanthanide materials. The overall goal of this research program is to investigate unresolved questions about the process of luminescence, focusing in particular on nonradiative transitions and the transfer of energy between different components of a luminescent system. We have shown that time-resolved x-ray absorption spectroscopy is sensitive to excitations of the 4f shell in disparate lanthanide-activated molecules and materials. From the perspective of applied physics and materials science, this enables activator-targeted measurements of the energy transfer rate and efficiency, and therefore is a novel method for evaluating a key figure of merit for lanthanide phosphors. This approach is particularly useful in cases where the emissive excited state of the activator can be strongly quenched by nonradiative processes, i.e., in cases where the optical emission does not directly reflect the excited state occupation.

From a fundamental physics perspective, the absorption spectroscopy results raise interesting questions about the character of the 4f intrashell excited states. In particular, we find that 4f excited states of Eu^{3+} are associated with a transient increase in spectral weight at energies corresponding to the 4f manifold. This implies either a change in the degree of 4f-5d mixing upon excitation, or a metal-to-ligand charge transfer contribution to the 4f excited state. Current theoretical models of the energy transfer process and subsequent $4f \rightarrow 4f$ emission assume that the 4f electronic structure is frozen. While this is a reasonable approximation to make, given the screened nature of the 4f orbitals, the results presented here imply that transient changes in 4f electronic structure are significant. This results in a strong involvement of the 4f electrons in the excited state character itself. While such effects are a topic of continuing interest

in solid-state physics of correlated electron systems, they are not commonly considered in molecular systems and certainly have not been anticipated in luminescent lanthanides. Proposed work, described below, would help resolve these questions while also addressing the nature of the interactions associated with the ligand-to-lanthanide energy transfer step.

In a second applied physics study, we have demonstrated the utility of x-ray excited optical luminescence for the identification of luminescence quenching mechanisms, and approximately quantified the effects of high-intensity x-ray probe pulses on lanthanide-doped samples. This lays the technical foundation for a portion of the additional studies outlined in the next section, which will require the high-intensity pulses available at third-generation synchrotron light sources and x-ray free electron laser (XFEL) facilities. Specifically, we have found that in laser-pump/x-ray probe studies, the x-ray probe itself can induce a significant 4f excited state population. This effect must be monitored during each future experiment to ensure that transient signals caused by the pump and the probe can be separated.

6.2 Future directions

As a next step, we have proposed a time-resolved x-ray emission spectroscopy (XES) study of luminescent materials using the subpicosecond time resolution and high flux available at the Linac Coherent Light Source (LCLS) to observe the onset of the energy transfer step. Here, the goal is to unambiguously distinguish between Förster and Dexter energy transfer from the sensitizer to the activator (Section 1.6). XES is highly sensitive to spin state, and will therefore allow us to monitor the change in total activator spin associated with Dexter transfer. Currently, the energy transfer mechanism can be identified in specific cases by using selection rules to eliminated one mechanism, or, more rarely, manipulating the sensitizer-activator distance and measure the resulting effects on the transfer rate. In general, however, one is limited to

calculating the transfer rates associated with each mechanism and comparing the results with experiment. We expect TR-XES to provide the first direct experimental signature of the energy transfer mechanism. In preparation for this experiment, we have commissioned high-efficiency portable instruments capable of collecting lanthanide *L*-shell XES (see the Appendix).

Another intriguing possibility raised by the XEOL result of Chapter 5 is to conduct x-ray pump/laser probe experiments. Here, the goal would be to investigate excited state cascades arising from radiatively forbidden transitions. That is, we would take advantage of the non-specific nature of x-ray excitation to study energy transfer pathways that are not practically accessible by laser excitation, thus giving a more detailed inquiry into, for example, nonradiative quenching mechanisms that are largely hidden from optical spectroscopies.

In summary, we have discovered an experimental signature for a crucial step in luminescence, with implications for the current theoretical understanding of lanthanide 4f photoactivation. We have also characterized the effects of a microfocused synchrotron x-ray beam on a luminescent sample and identified the associated luminescence saturation mechanism. Taken together, these results lay the groundwork for further studies with the goal of unambiguously identifying the sensitizer-to-lanthanide energy transfer mechanism. A recurring theme in this work is the use of the particular excitation channels accessible by X rays. This enables measurements that either complement UV/visible spectroscopy results or that provide uniquely specific information on the 4f electronic structure of the luminescent center.

Appendix A. A miniature X-ray emission spectrometer (miniXES) for high-pressure studies in a diamond anvil cell

Text of this appendix is from ref. [1], by J. I. Pacold[a], J. A. Bradley[b], B. A. Mattern[a], M. J. Lipp[b], G. T. Seidler[a], P. Chow[c], Y. Xiao[c], Eric Rod[c], B. Rusthoven[d] and J. Quintana[d].

[a]Physics Department, University of Washington, Seattle, Washington, 98195, United States
[b]Condensed Matter and Materials Division, Lawrence Livermore National Laboratory, Livermore, California, 94550, United States
[c]HPCAT, Carnegie Institution of Washington, Argonne, Illinois, 60439, United States
[d]APS Engineering Support Division, Argonne National Laboratory, Argonne, Illinois, 60439, United States

Abstract

Core-shell x-ray emission spectroscopy (XES) is a valuable complement to x-ray absorption spectroscopy (XAS) techniques. However, XES in the hard x-ray regime is much less frequently employed than XAS, often as a consequence of the relative scarcity of XES instrumentation having energy resolutions comparable to the relevant core-hole lifetimes. To address this, our research group has developed a family of inexpensive and easily-operated short working distance x-ray emission spectrometers. The use of computer-aided design and rapid prototype machining of plastics allows customization for various emission lines having energies from ~ 3keV to ~10 keV. The specific instrument described here, based on a coarsely-diced approximant of the Johansson optic, is intended to study volume collapse in Pr metal and compounds by observing the pressure dependence of the Pr Lα emission spectrum. The collection solid angle is ~50 msr, roughly equivalent to that of six traditional spherically-bent crystal analyzers. The miniature x-ray emission spectrometer (miniXES) methodology will help encourage the adoption and broad application of high-resolution XES capabilities at hard x-ray synchrotron facilities.

A.1 Introduction

Core-shell hard x-ray emission spectroscopy (XES) at 1-eV energy resolution is an important technique in condensed matter physics, coordination chemistry, earth sciences, and related fields. At such energy resolutions, one obtains very local assessments of the atomic oxidation and spin states and coordination geometry [2, 3]. Historically, however, a practical limitation has constrained the actual range of applications: few hard x-ray beamlines are equipped to perform high-resolution XES, while many are equipped to perform x-ray absorption spectroscopies. Appreciation for the value of resonant and nonresonant XES and high-energy resolution fluorescence detection (HERFD) has expanded in recent years, with applications in areas including catalysis science [4, 5], biology [6], earth sciences [7, 8], and more generally, identification of ligands [9, 10], time-resolved studies [11], and determination of metal oxidation states [12]. This growing understanding of the value of XES is driving upgrades of some hard x-ray XAS beamlines to also accommodate regular general access to XES and HERFD, in addition to having such methods included in the conceptual designs for beamlines under construction, such as the Inner Shell Spectroscopy (ISS) and submicron resolution x-ray spectroscopy (SRX) beamlines at NSLS-II.

With some notable exceptions [13-16], hard x-ray XES studies at 1-eV energy resolution have used spherically-bent crystal analysers (SBCA). These optics are placed ~1 m from the sample, and consequently subtend 8 msr, or about 1/1600 of 4π sr. This relatively small collection solid angle has led to the on-going development of dedicated multi-SBCA spectrometers for resonant and non-resonant XES [17-19] and for non-resonant inelastic x-ray scattering at similar energy resolutions [20, 21]. The existence of such instruments, however, is only a partial step toward resolving the shortage of XES and HERFD capability, since each one

is usually dedicated to a single beamline due to their construction cost, structural and operational complexity, and overall physical scale.

For the last few years we have been developing a family of portable, inexpensive, and easily-operated high-resolution hard x-ray spectrometers for use at synchrotron x-ray sources. These short working distance (SWD) dispersive spectrometers [22] make use of arrays of small, flat Bragg analysers placed near the sample. The SWD spectrometers, independent of the optical design, have become known as miniXES ("miniature x-ray emission spectrometers") in the synchrotron community, and we shall use that term in this paper. Our subsequent work on miniXES spectrometers based on the cylindrical von Hámos configuration [23] has recently been reported [24]. Here, we present and discuss design considerations for instruments based on the Johansson, i.e., perfect Rowland circle, geometry. We again use 3-D rapid prototype machining and in-context computer aided design. However, here we use a different, somewhat more flexible optical configuration and also tailor the design of a particular spectrometer for compatibility with a ubiquitous extreme sample environment: a diamond anvil cell (DAC).

In section A.2, we summarize the design considerations for Johannson-style miniXES instruments. The general framework for the optimal design of miniXES based on a Rowland circle construction is presented. Such an x-ray optic may be thought of as a coarsely-diced approximant to a Johannson bent crystal analyser [25]. In section A.3, we present design and fabrication details for the Pr $L\alpha$ spectrometer. This instrument is being used in high-pressure DAC studies of Pr metal and compounds where volume collapse is observed, in order to measure concomitant delocalization of the $4f$ electrons. In section A.4, we present results for the performance of this instrument, and discuss the generalization of this approach to other energy

ranges, systems, and sample environments. Finally, in section A.5, we briefly summarize and conclude.

A.2 The design of miniXES based on a Johansson configuration

As recently demonstrated [22], a hard x-ray dispersive spectrometer with 1-eV resolution can be based on a micro-focused beam, a modern 2-D position-sensitive detector (2D-PSD), and an array of small, flat Bragg analysers placed a few cm from the sample. This approach gives large collection solid angles; for example, a 1-cm^2 flat analyser at 10-cm working distance subtends a somewhat larger collection solid angle as a traditional 10-cm diameter, circular SBCA at 1-m working distance. Here we formalize the design, construction, and operation of an important class of such instruments, all with a view toward production of large numbers of miniXES spectrometers of various designs for wide distribution and application in the synchrotron radiation community.

In this section, we outline an optimal Rowland circle construction for miniXES-type instruments. By "optimal," we mean that the dispersed reflections efficiently fill the 2D-PSD surface while retaining unique illumination of each pixel (i.e., the dispersed reflections from distinct analyser crystals do not overlap). The design algorithm is described in purely geometric terms, and can therefore be easily implemented in any computer-assisted design (CAD) software that allows geometric constraints. First, in Fig. A.1a, we define the correct placement of flat crystals for Bragg angle θ on a Rowland circle of radius R. Note that scattering from the intersection A.point of any crystal with the Rowland circle comes to a common exit point on the circle. Second, in Fig. A.1b, we observe that all virtual sources for flat analysers properly oriented on the Rowland circle must rest on another circle, this one having radius $2R \sin \theta$ and centred about the point P as constructed in Fig. A.1a. Third, one may then show a novel result

that is closely related to the occurrence of 'dispersion compensation' in SBCA [26], namely that there is a spectral focusing effect along an arc of the circle for virtual sources. As shown in Fig. A.1b, independent of where any two Rowland-circle oriented crystals are placed, the scattering from common Bragg angles on their surfaces will necessarily intersect on the circle of virtual sources. This observation leads to the two key results: there is a unique location for an exit aperture that will select the same reflected energy range from each crystal, and Rowland circles for arbitrarily perturbed Bragg angles can be constructed in addition to the original (Bragg angle θ) Rowland circle. In Fig. A.1b, these new Rowland circles are defined by the points *S*, *P*, and $E(\theta\text{-}\Omega)$ for the Bragg angle $\theta\text{-}\Omega$ on any crystal, and similarly for Bragg angle $\theta\text{+}\Omega$.

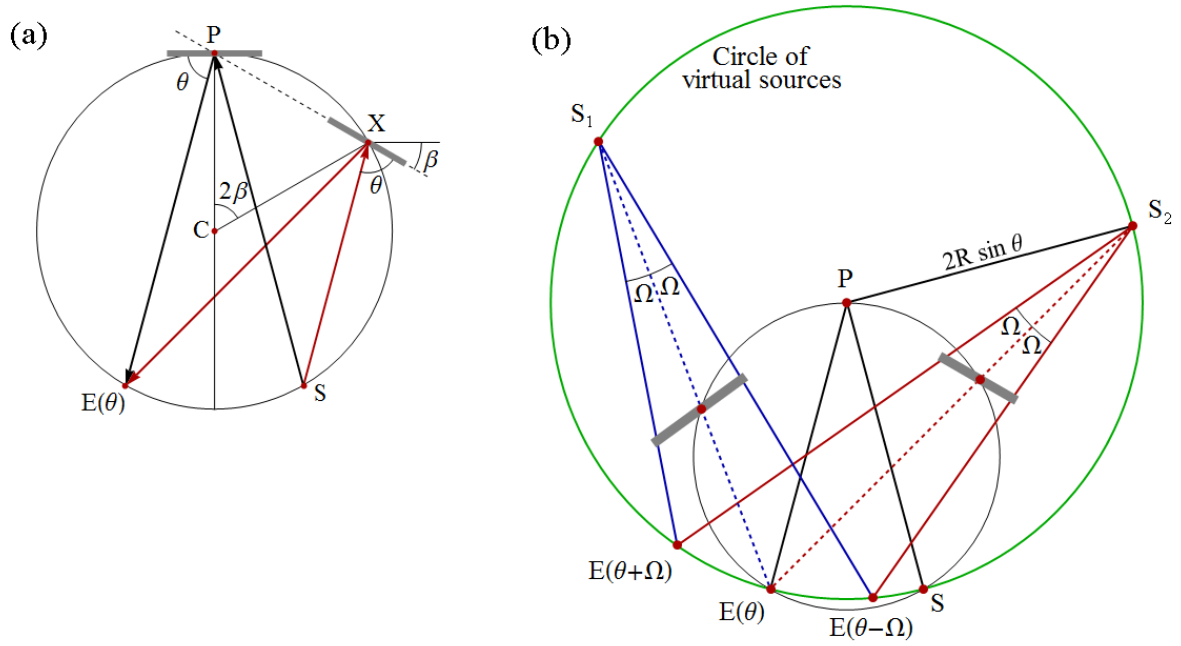

Figure A.1. (a) The Rowland circle geometry for flat analyser crystals. A crystal placed horizontally through the point P, at the top of the Rowland circle, reflects rays from the source S at Bragg angle θ to the point E(θ). A flat crystal passing through point X, where the radius CX is at an angle 2β from the vertical, must be tilted by β to reflect at the same Bragg angle. It follows that the crystal lies along the line PX. (b) From the observation that appropriately tilted crystals lie on lines passing through P, it is possible to show that the virtual source for reflection from any such crystal lies on a circle of radius 2 R sin θ centred at P. Given a range of Bragg angles, there is an arc on this circle that spatially selects rays reflected in this range from any crystal placed on the Rowland circle.

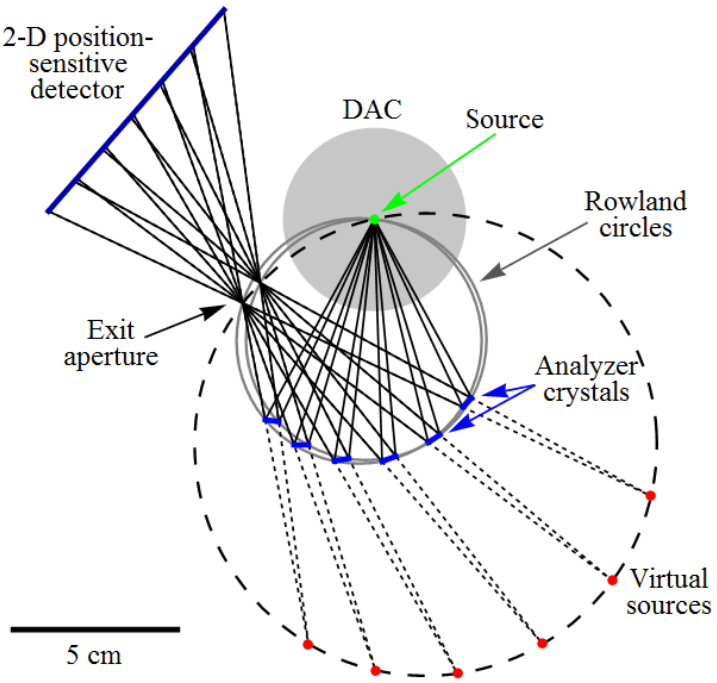

Figure A.2. Ray tracing diagram for a short working distance dispersive x-ray spectrometer. Two Rowland circles are constructed through the source point; flat analyser crystals with their endpoints on these circles can be tilted so that they all select the same range of Bragg angles. It then follows (see Fig. A.1) that the virtual sources for reflection from the crystals all lie on a third, larger circle (dashed), and that an aperture placed on this circle will select photons in the desired energy range. In this case, the position-sensitive detector was located to allow clearance for a 5.6 cm-diameter diamond anvil cell (DAC), and the average diameter of the Roland circles was approximately 7.4 cm, leaving clearance for a mounting bracket and translation stages (not shown) underneath the crystals.

With these tools in hand, it is now straightforward to design an optimal Johannson-style miniXES spectrometer for any selected energy range where the detector functions well. We first calculate the required range of Bragg angles, determined by the emission line(s) to be studied and the specific crystal reflection chosen. We then construct the necessary Rowland circles and the circle of virtual sources, and choose a tentative distance and orientation for the detector such that its spatial resolution will yield the desired energy resolution. Iterative ray-tracing between the detector face and the circle of virtual sources (Fig. A.2) then provides optimal locations for flat Bragg analysers. We may then gradually modify the Rowland circle radius, and detector location and orientation to satisfy other design constraints (e.g., to allow clearance for a DAC as

in the present instrument) while also maintaining the desired energy resolution and a substantial collection solid angle. We note that the underlying design can be easily customized for various emission lines, as discussed in section A.4.

A.3 Customization for high-pressure studies of Pr $L\alpha$ emission

Several of the elemental lanthanide metals, including Ce, Pr, and Gd, but interestingly not Nd, undergo first-order phase transitions at room temperature and high pressure, accompanied by a volume collapse of 5 – 15% [27-30]. With the exception of Ce there is an associated change in crystal structure, from high-symmetry transition-metal-like structures at low pressure (i.e., structures associated with elements without *f* electrons) to lower-symmetry actinide-like structures at high pressure. This suggests that in the low-pressure phase, bonding is dominated by the 5*d* electrons and the 4*f* electrons are localized, while in the high-pressure phase, the 4*f* electrons become delocalized [31, 32]. Because of its sensitivity to (1) 4*f* occupation number and (2) quantum mechanical mixing between the *f* and *d* states, *L*-shell emission spectroscopy is well-suited to studying the volume collapse of 4*f*-elements. Previous experiments have observed the pressure dependence of the Gd $L\gamma_1$ and $L\alpha$ lines, along with the Ce $L\alpha$ [33-35].

The present instrument is designed to observe the $L\alpha$ emission spectrum from Pr under high pressure. Consequently, the main design constraint is the clearance required for a diamond anvil cell. The samples in this device are kept between two diamonds to generate GPa-scale pressure and surrounded by a metal gasket (here, Be) for confinement. Depending on the target pressure range, typical gaskets are 5 - 50 μm thick and have a central hole 20 - 200 μm in diameter. Given these size constraints and the attenuation by the encapsulating material, x-ray emission experiments using SBCA can take hours of exposure to obtain a spectrum at a single pressure point, even at high flux beamlines [33].

The design methodology of section A.2 is implemented in the SolidWorks CAD environment. The fixed input parameters are the dimensions of the available 2D-PSD (Dectris Pilatus 100K) and the range of Bragg angles to be collected. The desired energy range (4989 – 5065 eV) and the crystal reflection Ge (331) give Bragg angles 70.6 – 73.2°, which is extended to 70.35 – 73.45° to provide angular tolerance for the final assembly. Experimentation with the radii of the Rowland circles and the detector distance and orientation resulted in the exact ray-tracing shown in Fig. A.2; in the final configuration, the collection solid angle is ~50 msr, roughly equivalent to 6 SBCA. This sketch is used as the basis for an in-context design of an instrument consisting of a combined spectrometer body and optic, together with an access door. Fig. A.3 shows CAD renderings of the spectrometer body constructed to hold the analyser crystals and the entrance and exit apertures, with the ray tracing of Fig. A.2 superimposed.

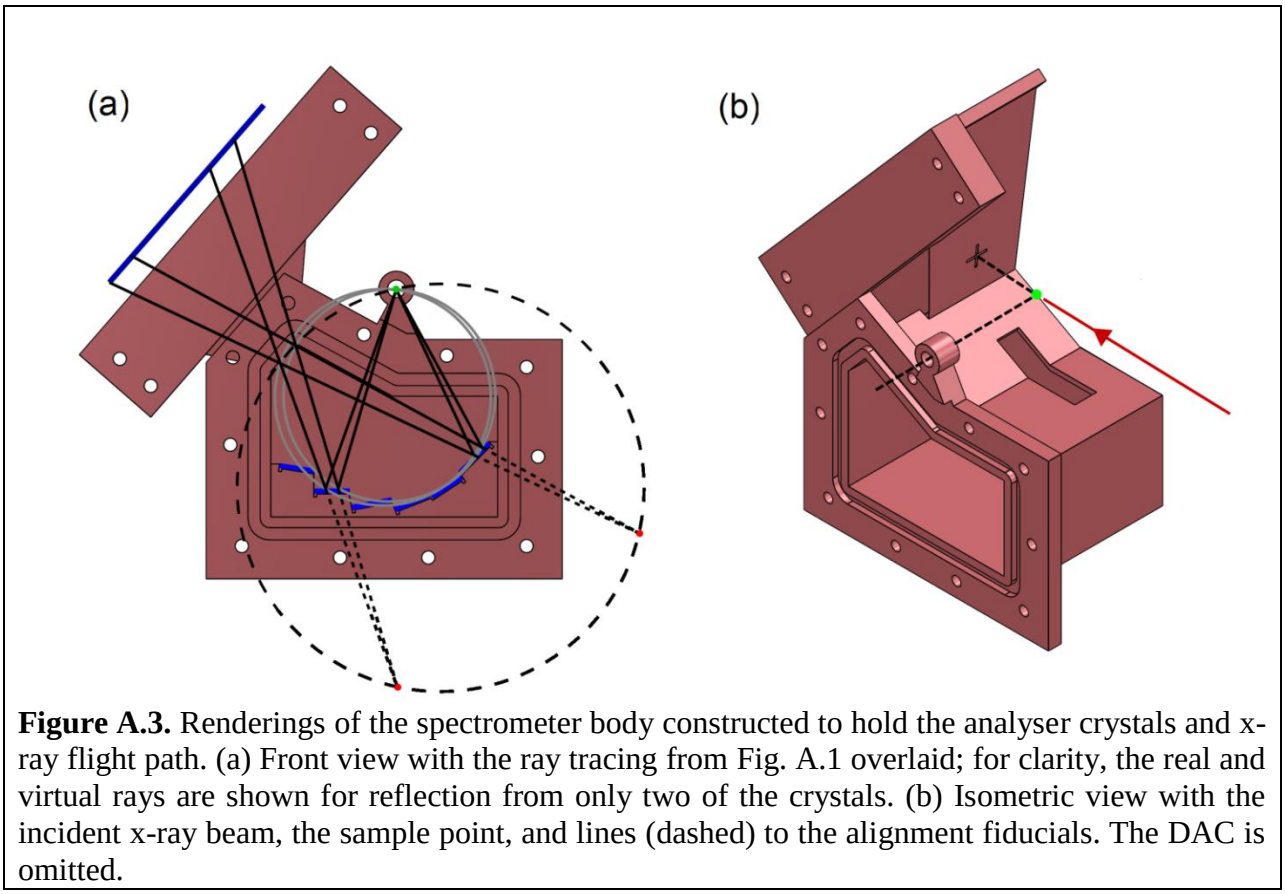

Figure A.3. Renderings of the spectrometer body constructed to hold the analyser crystals and x-ray flight path. (a) Front view with the ray tracing from Fig. A.1 overlaid; for clarity, the real and virtual rays are shown for reflection from only two of the crystals. (b) Isometric view with the incident x-ray beam, the sample point, and lines (dashed) to the alignment fiducials. The DAC is omitted.

The plastic spectrometer body was constructed from a thermosetting polymer by an Alaris 30 rapid-prototyping machine (colloquially, a "3-D printer"). This has proven to be an efficient and cost-effective way of manufacturing miniXES instruments; we have previously used it to produce Johansson-type spectrometers for the Co Kβ [36], Mn Kβ [37], and Ce Lα lines [38] in addition to von Hamos-style instruments for Fe Kβ [39] and Mn Kβ [37]. Profiling measurements have shown that the process holds angular tolerances to within 0.1°. Six Ge (331) crystals are placed on the plastic flats, and the rest of the inner surface is lined with 1-mm thick Pb tape. Visible in Fig. A.3 is a circular hole for rough alignment with the DAC axis, and a crosshair which is covered with a thin x-ray phosphor film and acts as a rough alignment target for the beam (the incident beam is normal to that face). A window cut in a 0.25 mm-thick Mo plate defines the exit aperture. Work with similar spectrometers has shown that the primary source of background is diffuse scattering of strong sample fluorescence from the analyser crystals and the internal surface of the spectrometer body; to reduce this, two additional 0.25 mm-thick Mo plates are used to define entrance apertures. Each of these plates contains three windows, with each window paired with one of the crystals. This constrains rays entering the spectrometer to illuminate the active region of each crystal (the apertures are oversized by ~20% in each dimension to allow for assembly tolerances). An O-ring sealed access-door, machined from 9.5 mm-thick poly(methyl methacrylate), contains entrance and exit fittings for He flow, installed by standard pipe tap threads. A 9.5 mm machined Al mounting plate fixes the relative positions of the spectrometer body and the 2D-PSD.

Fig. A.4 shows the spectrometer installed at Sector 16 of the Advanced Photon Source at Argonne National Laboratory. The spectrometer, 2D-PSD, and DAC are mounted on motorized

stages to allow reproducible removal and repositioning of each component. This allows the spectrometer and PSD to be translated downstream during adjustments of the DAC pressure.

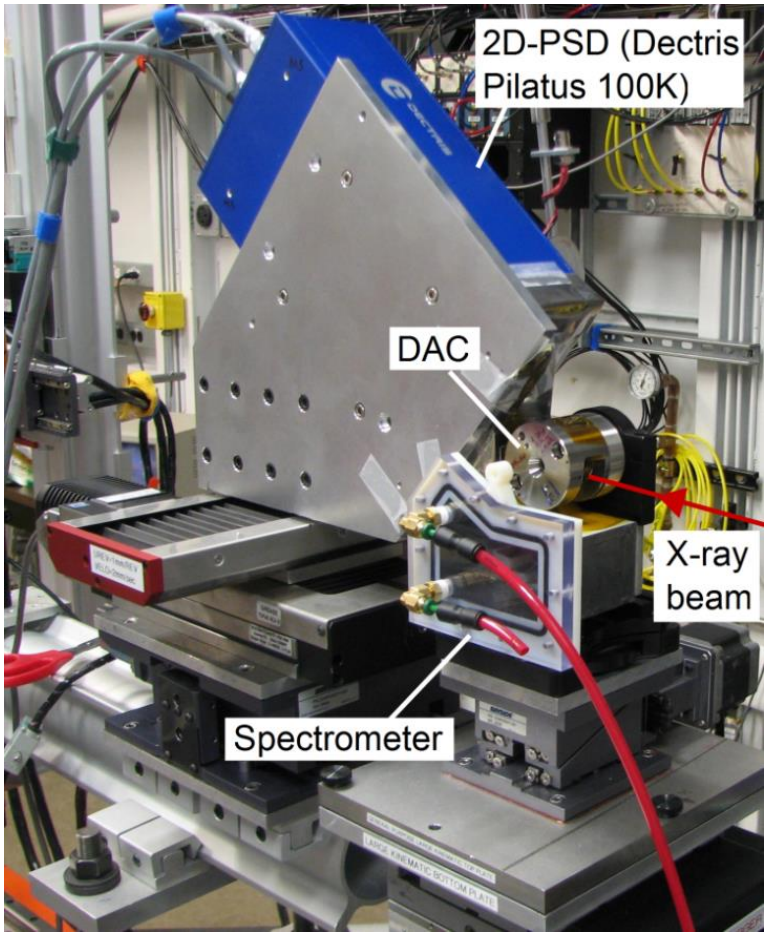

Figure A.4. A photograph of the instrument, with the diamond anvil cell and position-sensitive detector in place. For a sense of scale, note that the DAC has a diameter of 5 cm.

A.4 Spectrometer calibration, results, and discussion

Calibration of miniXES instruments for ambient-condition samples makes use of the elastic scattering from the sample itself [22, 39]. For DAC-based studies, the situation is complicated by the strong elastic scattering from either the diamond or the gasket, depending on the entrance and exit paths for the incident beam. Instead of using the elastic scattering from the target sample itself, the scattering from an ambient reference material (here, a 100-micron diameter borosilicate glass bead) is used to calibrate the spectrometer. The sample inside the

DAC is then placed at the same spatial location to within ~20 microns, ensuring that errors in energy calibration are less than ~0.15 eV. Spatial coincidence of the reference bead and DAC sample is established by standard means based on positioning each on the vertical axis of a rotation stage intersecting the incident beam's focal spot. With the reference bead in place, the incident photon energy is scanned in 7.5-eV steps through the designed energy range for detection of x-ray emission (4989 – 5064 eV). The monochromator, based on two diamond 111 reflections, has ~ 1-eV energy resolution in the relevant energy range, and the incident beam profile measures ~30 μm (V) by ~50 μm (H). A 2D-PSD exposure is taken at each step; interpolation between the pixels illuminated at each incident energy [39] produces a map of the photon energy detected by each pixel (Fig. A.5).

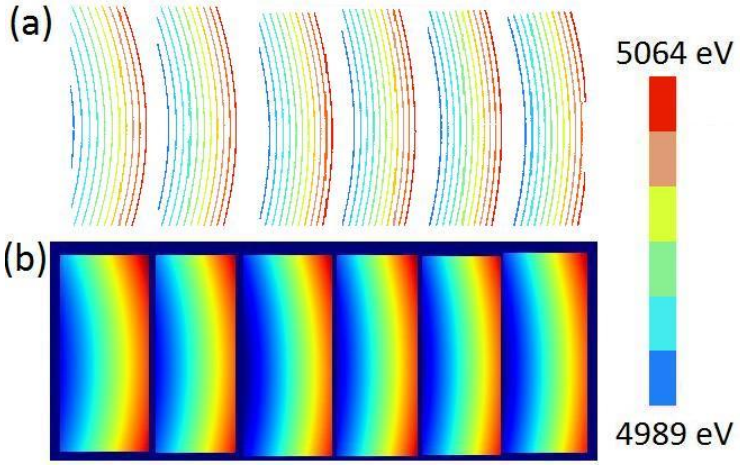

Figure A.5. (a) A composite image illustrating the calibration procedure. The incident energy was scanned through the detected energy band, and the pixels illuminated on the 2D PSD were recorded at each incident energy. Note that each crystal illuminates a separate region of the detector. (b) Interpolation between these points yields a map of the energy detected at each pixel on the PSD.

In the volume collapse study, a sample of pure Pr metal, approximately 150 microns in diameter and 50 microns thick at zero pressure, was sealed into a high-purity Be gasket inside the DAC. No pressure medium was used for the data set reported here, as the metal was soft enough to be deformed to fill the hole in the gasket. In addition, this avoided the possibility of chemical reactions at the Pr surface with a pressure-transmitting medium. Spectra were taken at

pressures ranging from ambient to 35 GPa and at multiple incident energies near the Pr L_3 edge. Illustrative results are shown in Fig. A.6 for P = 16 ± 2.5 GPa, in the general regime required for the transition.

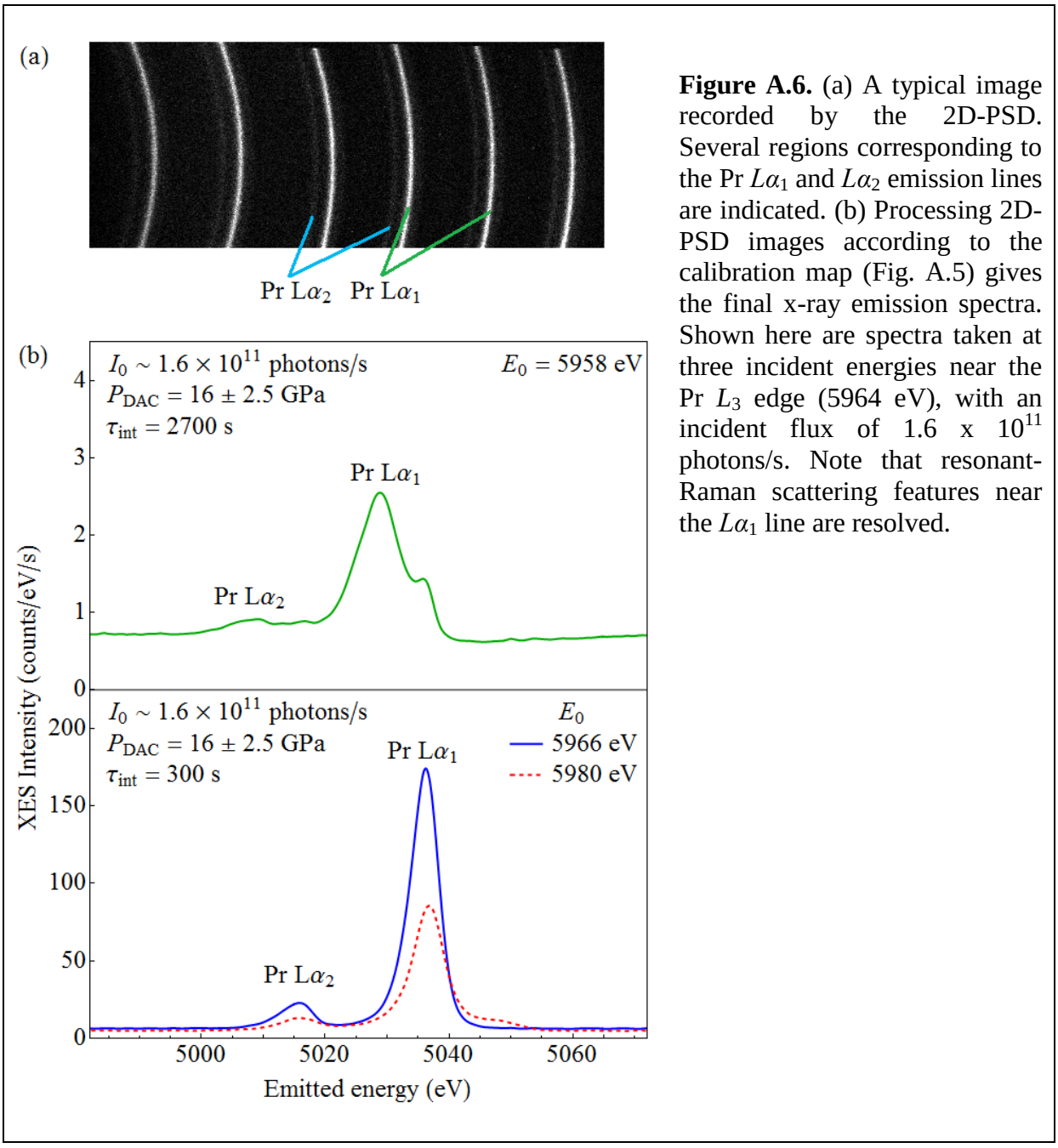

Figure A.6. (a) A typical image recorded by the 2D-PSD. Several regions corresponding to the Pr $L\alpha_1$ and $L\alpha_2$ emission lines are indicated. (b) Processing 2D-PSD images according to the calibration map (Fig. A.5) gives the final x-ray emission spectra. Shown here are spectra taken at three incident energies near the Pr L_3 edge (5964 eV), with an incident flux of 1.6 x 10^{11} photons/s. Note that resonant-Raman scattering features near the $L\alpha_1$ line are resolved.

The purely geometric resolution of the instrument is ~1.3 eV. The actual energy resolution, as determined by the width of the lines in the elastic exposures used to build the

calibration matrix, is ~2 eV (including convolution with the resolution of the monochromator). While the instrument has a collection solid angle roughly equivalent to 6 SBCA, overall count rates are low due to strong absorption of both the incident beam and the fluorescence by the DAC gasket (~1.5 mm thickness of Be). However, with the incident energy above the Pr L_3 edge (Fig. A.6b), an integration time of 300 s is sufficient to collect a very low-noise $L\alpha$ emission spectrum with an incident flux of 1.6 x 10^{11} photons/s. As mentioned above, inelastic scattering of sample fluorescence from the analyser crystals is believed to be the main source of background in miniXES instruments. The problem may be exacerbated in this case by the strong stray scatter of both the incident beam and fluorescence from the Be gasket. Even so, the background is constant to within 3 counts/eV/s, and is well below the intensity of the resonant $L\alpha_1$ emission (~100 counts/eV/s). At times, a vanadium chemical filter was used at the entrance aperture to maximize $L\alpha_1$ signal to (stray scattered) background. Further results on the pressure dependence of the resonant XES from Pr and the issue of volume collapse are presented elsewhere [40]. We note that a separate study used a similar miniXES optical configuration to collect $L\alpha$ emission spectra from Ce compounds [38]. The resolution, count rates, and low noise levels obtained during these studies show that the miniXES approach is a convenient and effective tool for investigating the physics of *f*-electron materials.

With the use of CAD software, it is straightforward to modify the underlying design for observation of a wide range of emission lines, subject to the following limitations. First, the 2D-PSD must have sensitivity in the desired energy range and also must have nearly zero dark- and readout-noise; exposures at the level of an average of one count of true signal per pixel generate extremely quiet analysed spectra. Second, there must be an appropriate crystal reflection for the desired energy band. By “appropriate,” we mean that the Bragg angles should be close enough to

backscatter to allow the desired energy resolution per pixel with a relatively short total distance from sample to the 2D-PSD. For the Pilatus 100k at ~10 keV, this means that the Bragg angle should be less than ~20° from backscatter. In addition, given the range of required incident energies, it is necessary to compile a list of other crystal planes that can reflect elastic scattering, Compton scattering, or fluorescence from other species onto the 2D-PSD, producing spurious secondary counts. Such interfering planes generally do not exist for high-symmetry analyser crystals (e.g., Si, Ge, and GaP) and photon energies below 6.5 keV, but at higher energies they may rule out some crystal reflections.

As examples, some viable crystal reflections for the $L\alpha$ emission from each of the lanthanides are listed in Table 1. For specific instruments, additional considerations may apply, e.g., the amount of clearance required around the sample and the reflectivity of the possible crystals. Finally, it is crucial to recall that the incident beam must be focused to dimensions somewhat smaller than the pixel size of the 2D-PSD, so that the pixel size is the limiting contributor to the spectrometer's energy resolution. Once the design is finalized, construction and commissioning is conveniently brief. Typically two days of machining time are required for the mechanical support components and Mo shielding, and the rapid prototyping process for the spectrometer body takes roughly a day. After assembly and commissioning, the instrument can be removed and re-installed at the beamline in a few hours, as was the case here.

A.5 Conclusion

We present a complete design algorithm and methodology for the fabrication of miniXES spectrometers based on the Rowland circle construction. These portable instruments can be quickly installed at any at least modestly focused hard x-ray spectroscopy endstation. To illustrate, we have designed, constructed, and commissioned such a short working distance

spectrometer for resonant XES studies of Pr at high pressures in a standard diamond anvil cell. CAD software was used to preserve the necessary geometry for the analyser crystals while ensuring compatibility with the sample environment. The resulting instrument has low cost, but high collection efficiency and ease of use. The design can be easily modified for studies of other elements. This approach will help spread the adoption of 1-eV resolution XES as a complementary technique to x-ray absorption spectroscopies at hard x-ray beamlines.

A.6 Acknowledgments

GTS acknowledges support of this research program by the U.S. Department of Energy, Basic Energy Sciences, under award DE-SC0002194. This work was performed at HPCAT (Sector 16), Advanced Photon Source (APS), Argonne National Laboratory. HPCAT is supported by CIW, CDAC, UNLV and LLNL through funding from DO E-NNSA, DOE-BES and NSF. APS is supported by DOE-BES, under Contract No. DE-AC02-06CH11357. Part of this work was performed under the auspices of the U.S. Department of Energy by Lawrence Livermore National Laboratory under contract DEAC52-07NA27344.

Table A.1. Energies of the Lα emission lines of the lanthanides, with corresponding crystal reflections from silicon, germanium, and gallium phosphide. The Bragg angles listed correspond to 20 eV below the Lα2 energy and 20 eV above the Lα1 energy. Reflections were omitted if both of these angles were less than 70° (i.e., if the entire range of Bragg angles selected by the resulting spectrometer would be more than 20° away from backscatter).

Z	Element	$L\alpha_1$ (eV)	$L\alpha_2$ (eV)	Crystal reflection	Bragg angles (°)	
57	La	4651	4634	Ge 400	69.78	71.80
				Si 400	77.82	81.72
				GaP 400	76.87	80.36
58	Ce	4840	4823	Ge 331	79.36	83.97
				Si 400	69.96	71.92
				GaP 400	69.39	71.28
59	Pr	5034	5013	Ge 331	70.92	73.06
				Si 331	79.89	85.21
60	Nd	5230	5208	Si 331	71.39	73.55
61	Pm	5432	5408	Ge 422	79.94	85.09
62	Sm	5636	5609	Ge 422	71.64	73.84
63	Eu	5846	5816	Ge 511/333	76.08	79.23
				Si 422	72.42	74.75
64	Gd	6057	6025	Ge 511/333	69.55	71.47
				Si 511/333	77.43	81.01
				GaP 333	76.50	79.75
65	Tb	6273	6238	Ge 440	80.07	85.48
				Si 511/333	70.48	72.53
				GaP 333	69.89	71.87
66	Dy	6495	6458	Ge 440	72.07	74.33
				GaP 440	80.90	87.76
67	Ho	6720	6679	Si 440	73.34	75.86
				GaP 440	72.64	75.03
68	Er	6949	6905	Si 531	75.70	78.76
69	Tm	7181	7133	Ge 620	74.24	76.99
				Si 531	69.68	71.69
70	Yb	7414	7367	Si 620	76.20	79.30
				Ge 533	75.14	77.96
				Ge 620	68.79	70.61

A.7 References

1. Pacold, J.I., et al., *A miniature X-ray emission spectrometer (miniXES) for high-pressure studies in a diamond anvil cell.* Journal of Synchrotron Radiation, 2012. **19**: p. 245-251.
2. de Groot, F., *Multiplet effects in X-ray spectroscopy.* Coordination Chemistry Reviews, 2005. **249**(1-2): p. 31-63.
3. Glatzel, P. and U. Bergmann, *High resolution 1s core hole X-ray spectroscopy in 3d transition metal complexes - electronic and structural information.* Coordination Chemistry Reviews, 2005. **249**(1-2): p. 65-95.
4. van Bokhoven, J.A., J. Singh, and C. Lamberti, *Advanced X-ray absorption and emission spectroscopy: in situ catalytic studies.* Chemical Society Reviews, 2010. **39**(12): p. 4754-4766.
5. Yamamoto, T., et al., *Quantitative Chemical State Analysis of Supported Vanadium Oxide Catalysts by High Resolution Vanadium K alpha Spectroscopy.* Analytical Chemistry, 2011. **83**(5): p. 1681-1687.
6. Bergmann, U. and P. Glatzel, *X-ray emission spectroscopy.* Photosynthesis Research, 2009. **102**(2-3): p. 255-266.
7. Badro, J., et al., *Electronic transitions in perovskite: Possible nonconvecting layers in the lower mantle.* Science, 2004. **305**(5682): p. 383-386.
8. Lin, J.F., et al., *Spin transition of iron in magnesiowustite in the Earth's lower mantle.* Nature, 2005. **436**(7049): p. 377-380.
9. Swarbrick, J.C., et al., *Ligand Identification in Titanium Complexes Using X-ray Valence-to-Core Emission Spectroscopy.* Inorganic Chemistry, 2010. **49**(18): p. 8323-8332.
10. DeBeer, S. and C.J. Pollock, *Valence-to-Core X-ray Emission Spectroscopy: A Sensitive Probe of the Nature of a Bound Ligand.* Journal of the American Chemical Society, 2011. **133**(14): p. 5594-5601.
11. Vanko, G., et al., *Picosecond Time-Resolved X-Ray Emission Spectroscopy: Ultrafast Spin-State Determination in an Iron Complex.* Angewandte Chemie-International Edition, 2010. **49**(34): p. 5910-5912.
12. Bordage, A., et al., *V oxidation state in Fe-Ti oxides by high-energy resolution fluorescence-detected X-ray absorption spectroscopy.* Physics and Chemistry of Minerals, 2011. **38**(6): p. 449-458.
13. Hayashi, K., et al., *Wave-dispersive x-ray spectrometer for simultaneous acquisition of several characteristic lines based on strongly and accurately shaped Ge crystal.* Review of Scientific Instruments, 2008. **79**(03): p. 3110.
14. Hoszowska, J., et al., *High-resolution von Hamos crystal X-ray spectrometer.* Nuclear Instruments & Methods in Physics Research Section A, 1996. **376**(1): p. 129-138.
15. Hoszowska, J., et al., *First Observation of Two-Electron One-Photon Transitions in Single-Photon K-Shell Double Ionization.* Physical Review Letters, 2011. **107**(05): p. 3001.
16. Hayashi, H., et al., *A multi-crystal spectrometer with a two-dimensional position-sensitive detector and contour maps of resonant K beta emission in Mn compounds.* Journal of Electron Spectroscopy and Related Phenomena, 2004. **136**(1-2): p. 191-197.
17. Qian, Q., et al., *High-efficiency high-energy-resolution spectrometer for inelastic X-ray scattering.* Journal of Physics and Chemistry of Solids, 2005. **66**(12): p. 2295-2298.

18. Kleymenov, E., et al., *Five-element Johann-type x-ray emission spectrometer with a single-photon-counting pixel detector.* Review of Scientific Instruments, 2011. **82**(06): p. 5107.
19. Bergmann, U. and S.P. Cramer, *A High-Resolution Large-Acceptance Analyzer for X-ray Fluorescence and Raman Spectroscopy.* Proc. SPIE, 1998. **3448**: p. 198.
20. Fister, T.T., et al., *Multielement spectrometer for efficient measurement of the momentum transfer dependence of inelastic x-ray scattering.* Review of Scientific Instruments, 2006. **77**(6): p. 3901.
21. Verbeni, R., et al., *Multiple-element spectrometer for non-resonant inelastic X-ray spectroscopy of electronic excitations.* Journal of Synchrotron Radiation, 2009. **16**: p. 469-476.
22. Dickinson, B., et al., *A short working distance multiple crystal x-ray spectrometer.* Review of Scientific Instruments, 2008. **79**(12): p. 3112.
23. von Hámos, L., Annalen der Physik, 1933. **409**(6): p. 716-724.
24. Mattern, B.A., et al., *A plastic miniature x-ray emission spectrometer based on the cylindrical von Hamos geometry.* Review of Scientific Instruments, 2012. **83**(2): p. 3901.
25. Johansson, T., *Über ein neuartiges, genau fokussierendes Röntgenspektrometer Erste Mitteilung.* Zeitschrift Für Physik A, 1933. **82**(7-8): p. 507-528.
26. Huotari, S., et al., *Improving the performance of high-resolution X-ray spectrometers with position-sensitive pixel detectors.* Journal of Synchrotron Radiation, 2005. **12**: p. 467-472.
27. McMahan, A.K., *Combined local-density and dynamical mean field theory calculations for the compressed lanthanides Ce, Pr, and Nd.* Physical Review B, 2005. **72**(11): p. 5125.
28. McMahan, A.K., R.T. Scalettar, and M. Jarrell, *Screening of 4f moments and delocalization in the compressed light rare earths.* Physical Review B, 2009. **80**(23): p. 5105.
29. Lipp, M.J., et al., *Thermal Signatures of the Kondo Volume Collapse in Cerium.* Physical Review Letters, 2008. **101**(16): p. 5703.
30. Zhao, Y.C., F. Porsch, and W.B. Holzapfel, *Determination of Triple Points in the Phase-Diagram of Praseodymium.* Physical Review B, 1995. **52**(1): p. 134-137.
31. Allen, J.W. and R.M. Martin, *Kondo Volume Collapse and the Gamma-Alpha Transition in Cerium.* Physical Review Letters, 1982. **49**: p. 151106.
32. Soderlind, P., *Delocalization and phase transitions in Pr: Theory.* Physical Review B, 2002. **65**(11): p. 5105.
33. Maddox, B.R., et al., *4f delocalization in Gd: Inelastic x-ray scattering at ultrahigh pressure.* Physical Review Letters, 2006. **96**(21): p. 5701.
34. Rueff, J.P., et al., *Probing the gamma-alpha transition in bulk Ce under pressure: A direct investigation by resonant inelastic x-ray scattering.* Physical Review Letters, 2006. **96**(23): p. 7403.
35. Rueff, J.P. and A. Shukla, *Inelastic x-ray scattering by electronic excitations under high pressure.* Reviews of Modern Physics, 2010. **82**(1): p. 847-896.
36. Kelly, S., et al., 2011(in preparation).
37. Davis, K.M., et al., *Fast Detection Allowing Analysis of Metalloprotein Electronic Structure by X-ray Emission Spectroscopy at Room Temperature.* Journal of Physical Chemistry Letters, 2012. **3**(14): p. 1858-1864.

38. Gordon, R.A., et al., *Hard X-ray RIXS and NIXS of ionic cerium compounds.* Physical Review B, 2011(submitted).
39. Mattern, B.A., et al., *A Short Working Distance von Hamos X-ray Spectrometer.* Review of Scientific Instruments, 2011(revised manuscript submitted).
40. Bradley, J.A., et al., *4f electron delocalization and volume collapse in praseodymium metal.* Physical Review B, 2012. **85**(10).